

FIBER-OPTIC SILICON FABRY-PEROT INTERFEROMETERS FOR HIGH-SPEED  
ANEMOMETER AND HIGH-SENSITIVITY BOLOMETER APPLICATIONS

By

Nezam Uddin

A DISSERTATION

Submitted to  
Michigan State University  
in partial fulfillment of the requirements  
for the degree of

Electrical Engineering – Doctor of Philosophy

2022

## **ABSTRACT**

### **FIBER-OPTIC SILICON FABRY-PEROT INTERFEROMETERS FOR HIGH-SPEED ANEMOMETER AND HIGH-SENSITIVITY BOLOMETER APPLICATIONS**

By

Nezam Uddin

Fiber-optic silicon Fabry-Perot interferometric temperature sensor offers the advantage of high-speed and high-resolution to characterize the ocean turbulence in oceanographic research. Compared to silica, the material that makes the optical fiber, silicon has a thermo-optic coefficient ten times higher and a thermal conductivity sixty time higher. Silicon is highly transparent in the infrared wavelength range and can be easily processed with the mature microfabrication technology. All of these make silicon a very attractive material for high-speed and high-resolution turbulence measurement. We attached a small silicon pillar to the end of an optical fiber to make fiber-optic Fabry-Perot interferometric sensor demodulated by a white light system for fast turbulence measurement. We studied the two modes of fiber-optic hot wire anemometer operation for turbulence measurement theoretically and experimentally. The constant temperature operation of the fiber-optic hot wire anemometer was introduced for the first time to reduce the time constant significantly. The anemometer used for demonstration is based on a silicon low-finesse Fabry-Perot interferometer (FPI) attached to the tip of a single mode fiber. Turbulent flow measurement method based on constant temperature operation offers high measuring speed, because the wire temperature is kept constant, the effect of thermal inertia of the wire is suppressed. We also investigated a new sensor structure experimentally and theoretically for the measurement of water flow with reduced directivity. This sensor consists of a laser heated silicon FPI embedded in a metal microsphere. Herein, the spherical shape of the outside metal shell gives a symmetric response to water flow direction; thus, the directivity is reduced greatly. Moreover, the water flow

measurement by the hot wire fiber-optic water flow sensor based on laser heated silicon FPI need to compensate the effect of water temperature variation. We reported a technique to compensate the effect of water temperature change in the flow measurement by using another sensor which will track the temperature of the water. By using the information of the water temperature change, baseline can be defined which will provide unique wavelength change for the flow. Finally, the wavelength change corresponding to the flow speed were calibrated using the sensor pair after compensating the effect of water temperature variation.

We expanded the use of silicon Fabry-Perot interferometric sensor in the measurement of plasma radiation by modifying the structure with gold coated silicon and multimode graded index fiber between the single mode fiber (SMF) and silicon. We reported the design, fabrication, and characterization of a fiber-optic bolometer (FOB) with improved noise equivalent power density (NEPD) performance and increased absorption to high energy photons by engineering the absorber of the FOB. We also have developed a multichannel fiberoptic bolometry system with five bolometers connected to each channel of the coarse wavelength division multiplexer (CWDM), a single light source of super luminescent LED (SLED) and a single I-MON 512 OEM spectrometer. Easy sensor fabrication, significantly enhanced measurement range compared to the previous high-finesse FPI bolometer system for measuring radiation are some of the advantages. Moreover, utilization of the FOB in the vacuum for radiation measurement with reduced time constant was also studied which is practically required in the fusion devices. This was done by adding a heat sink with the current FOB structure and using the deconvolution method to get better temporal resolution. Finally, the FOB with the heat sink was tested in the vacuum condition to measure the radiation using the deconvolution method. Experimental results are presented to support the idea of heat sink and deconvolution method for plasma radiation measurement.

## ACKNOWLEDGEMENTS

Thank you will not be enough to express my gratitude to Professor Ming Han. I am very lucky to have a professor like Dr. Ming Han in my PhD. Whatever I did in my PhD, it came into reality only because of his continuous guidance, support, and encouragement. I appreciate his all kinds of help in academic activities and personal life.

I would like to offer my gratitude to my committee members: Professor Tim Hogan, Professor Wen Li, Professor Zhen Qiu for their suggestions and guidance in my comprehensive exam and dissertation defense. I would like to thank our collaborator Dr. W. Hou (NRL), Dr. Matthew Reinke (ORNL), Dr. Morgan Shafer (ORNL), and Dr. David Donovan (UTK). I learnt a lot from their comments on my experimental results. It helped me to get fruitful outcome easily due to their valuable suggestions. I am also grateful to the funding sources as this work was partially supported by National Science Foundation (Award No.: 1918074), Oak Ridge National Laboratory Subcontract No.: 4000178111 (under Department of Energy (DoE) Contract No. DE-AC05-00OR22725), Department of Energy (DoE) (Award No.: DE-SC0019058).

My lab members always helped me in my research. I would like to thank Dr. Guigen Liu and Dr. Qiwen Sheng for their tremendous help in conducting the experiment. A big thank you goes to Brian Wright, Karl Dersch, Roxanne Peacock, Jordan Bird, Meagan Kroll and other staff members at ECE who made our works easy by their dedication and hard work.

My PhD journey became smoother because of many good friends. They always helped my in my academic matters as well as in my personal life. Dr. Asif Iqbal Arnob, Dr. Wasif Afsari, Dr. Jubaid Abdul Qayyum, Dr. Md Afibuzzaman, Dr. Shams Reaz, Dr. Shafaat Shishir, Dr. Tamanna Tabassum Munia, Al-Ahsan Talukder, Abu Farzan just to name a few.

My wife made my PhD journey very simple. She always encouraged, supported, motivated me to dream for big. Kudos to her hard work and dedication towards my success. Because of her effort, I was able to complete my PhD this early. Thanks to my son Zayan Aabid for being the best son in the world. I am grateful to my brother Nazim Uddin for his contribution in my life. He always guided me in the right direction. Finally, and most importantly I would like to express my gratitude to my parents for their belief and encouragement to go for bigger dreams.

# TABLE OF CONTENTS

LIST OF FIGURES.....	viii
Chapter 1: Introduction.....	1
1.1. Background and Motivation of the work.....	1
1.2. Organization of this report.....	6
Chapter 2: Turbulence measurement by Anemometer.....	8
2.1. Constant temperature operation of the fiber-optic hot wire anemometer.....	8
2.1.1. Introduction.....	8
2.1.2. Experimental set up and principle of operation.....	10
2.1.3. Theoretical analysis.....	13
2.1.4. Experimental Results.....	18
2.1.5. Summary.....	23
2.2. Reduction of directivity of the fiber-optic water flow sensor.....	24
2.2.1. Introduction.....	24
2.2.2. Principle of operation.....	25
2.2.3. Sensor fabrication and experimental procedure.....	27
2.2.4. Experimental Results.....	28
2.2.5. Summary.....	30
2.3. Temperature compensation of fiber-optic water flow sensor.....	30
2.3.1. Introduction.....	31
2.3.2. Principle of operation.....	33
2.3.3. Experimental set up.....	34
2.3.4. Experimental results.....	35
2.3.5. Conclusion.....	37
Chapter 3: Fiber-optic silicon Fabry-Perot interferometric Bolometer.....	38
3.1. Fiber-optic silicon Fabry-Perot interferometric bolometer.....	38
3.1.1. Introduction.....	38
3.1.2. Principle of operation.....	40
3.1.3. Design and fabrication of the FOB.....	44
3.1.3.1. Gold disk preparation.....	44
3.1.3.2. FOB fabrication.....	46
3.1.4. FOB characterization.....	48
3.1.5. Results.....	50
3.1.6. Summary.....	54
3.2. Multichannel fiber-optic silicon Fabry-Perot interferometric bolometer.....	55
3.2.1. Introduction.....	55
3.2.2. Bolometer fabrication and experimental procedure.....	59
3.2.3. Results.....	61
3.2.3.1. Optical power management.....	62
3.2.3.2. Difference in Tracking of Fringes Valleys and Fringe Peaks.....	67

3.2.3.3. Effect of Mechanical Vibration .....	68
3.2.3.4. NEPDs and Time Constants.....	70
3.2.4. Summary .....	72
3.3. FOB with heat sink for plasma radiation measurement in vacuum.....	74
3.3.1. Deconvolution method.....	75
3.3.1.1. Background.....	76
3.3.1.2. Signal processing .....	78
3.3.2. FOB with heat sink .....	81
3.3.2.1. Fabrication of the FOB .....	81
3.3.2.2. Experimental results in air .....	82
3.3.3. FOB with heat sink in vacuum.....	84
Chapter 4: Conclusion and Future work .....	87
4.1. Summary .....	87
4.2. Future work.....	88
<b>BIBLIOGRAPHY.....</b>	<b>90</b>

## LIST OF FIGURES

Figure 1.1 Schematic diagram of the silicon Fabry-Perot interferometric sensor. ....	1
Figure 1.2 Schematic diagram of the thermometer operation without (a) and with (c) active laser heating, spectral notch shift from the temperature change (d). Inset shows the fiber-optic silicon Fabry-Perot interferometric sensor. ....	3
Figure 1.3 (a) Schematic diagram of the constant power operation and (b) constant temperature operation. ....	4
Figure 1.4 (a) Schematic diagram of the basic bolometer design and (b) extension of the fiber-optic silicon Fabry-Perot temperature sensor as bolometer. ....	5
Figure 2.1 (a) Schematics of the experimental setup to study the CT operation of a fiber-optic anemometer (the inset shows the structure and a microscope image of the anemometer consisting of a silicon FPI at the tip of an optical fiber; Att., attenuator). (b) Spectrum measured by the optical spectrum analyzer (OSA) with blue and red curves plotted in different scales. (c) Spectral response of the silicon FPI to the test laser when the system was under locked and unlocked conditions (for clarity, an offset is added to the solid black and dashed black curves). ....	10
Figure 2.2 Transfer function of the constant temperature (a) and constant power operation (b) of fiber-optic hot wire anemometer. ....	14
Figure 2.3 Step response of the fiber-optic anemometer operated in constant temperature operation (a) and constant power operation (c) respectively. Amplitude (b) and phase response (d) of the transfer function for CT and CP operation. ....	18
Figure 2.4 Control and monitor signals of the feedback control system when the anemometer is operated in CT mode. ....	18
Figure 2.5 Step response of the fiber-optic anemometer when operated in CT mode (a) and CP mode (b). ....	20
Figure 2.6 Step response of the fiber-optic anemometer when operated in CT mode (a) and CP mode (b). ....	22
Figure 2.7 Output signal versus radiation power from the test laser. ....	23
Figure 2.8 Schematic diagram of the sensor with (a) only silicon pillar and (b) silicon pillar embedded in a metal sphere. ....	25
Figure 2.9 Measurement of the sensor directivity, (a) Definition of incident angle of the flow. and (b), (c) images of the sensor taken from two different angles. ....	27

Figure 2.10 A typical reflection spectrum obtained from the fabricated sensor (a), and directional response for the sensor having silicon pillar only (b) and metal spherical layer (c), respectively, which is summarized and compared in (d). ..... 29

Figure 2.11 (a) Schematic diagram of the sensor and (b) typical sensor spectrum from the two silicon FPIs..... 34

Figure 2.12 Experimental setup for measuring the flow (a), sensor spectrum from in air (b) and microscopic image of the sensor head (c) and (d). ..... 34

Figure 2.13 Wavelength position of the heated and cold sensor at no flow (a), 70 mm/s (b) and (c) calibration of the flow sensor..... 37

Figure 3.1 Schematic of the (a) FOB head with a gold disk flush with the silicon pillar (old design), (b) resonant wavelength shift in response to radiation absorption, (c) FOB head with a large gold disk (new design), (d) responsivity, defined as the temperature change to an incident power flux of  $1 \text{ W/m}^2$  (assuming 100% absorption) as a function of the Au disk diameter for the FOB of new design with a 100- $\mu\text{m}$ -thick, 125- $\mu\text{m}$ -diameter silicon pillar and a 4- $\mu\text{m}$ -thick gold disk (for comparison, responsibility for the FOB without the gold disk is also shown), and (e) responsivity as a function of photon energy considering the attenuation length of the materials for the two FOBs. .... 41

Figure 3.2 Schematic diagram of the fabrication process of the gold disk: (a) silicon wafer deposited with Ti and Cu; (b) silicon wafer deposited with Ti, Cu, and Au; (c) spin-coated photoresist layer on the top of Au layer; (d) the photoresist patterned layer by lithography; (e) Au etching; (f) deposited photoresist removed; (g) Cu etching; and (h) gold disk. .... 45

Figure 3.3 (a) Image of the gold disk on silicon wafer. (b) SEM image of the gold disk separated from the wafer (top view), (c) side view, and (d) EDS spectrum of the gold disk. .... 46

Figure 3.4 (a)–(f) Schematics of the fabrication steps for the FOB without and with a large gold disk; microscope images of the FOBs of the previous design (g) and the new design (i); reflection spectra of the FOBs of the previous design (h) and the new design (j). .... 48

Figure 3.5 Experimental setup to characterize the noise and responsivity of the FOB. .... 49

Figure 3.6 (a) Original data captured using DAQ for the two bolometers without any radiation; relative temperature variation of the (b) FOB without a large gold disk, and (c) FOB with a large gold disk in the absence of radiation laser. .... 51

Figure 3.7 Time history of the temperature change in the FOB without a large gold disk [(a) and (c)] and the FOB with a large gold disk [(b) and (d)], exposed to a 0.1 Hz square wave power flux at  $\sim 37 \text{ W/m}^2$  and  $\sim 57 \text{ W/m}^2$ , respectively. Close-up view of a response circle of the FOB without a large gold disk (e) and the new FOB with a large gold disk (f). .... 52

Figure 3.8 Measured SNR vs power density for the bolometer without and with a large gold disk. .....	54
Figure 3.9 (a) System configuration of a previously reported bolometer system (inset shows the bolometer structure based on a high-finesse FPI); PD: photodetector; HR: high reflection. (b) System configuration of the multichannel bolometer system reported here (inset shows the bolometer structure based on a low-finesse FPI used in this work). .....	57
Figure 3.10 (a) Fabrication steps of the fiber-optic bolometers; (b) microscopic image of one of the fabricated bolometers; (c) scanning electron microscope image of the gold disk used to fabricate the bolometer shown in (b); (d) reflection spectrum of the bolometer measured by a fiber-optic sensor interrogator; (e) experimental setup for demonstrating and testing the multichannel bolometer system; (f) bolometers in a sealed glass tube for noise test, and (g) bolometers sealed in an aluminum cube for radiation response measurement. ....	59
Figure 3.11 (a, d) Reflection spectrum from the fiber-optic bolometers measured by the spectrometer at different exposure times and peak intensities, respectively; (b, e) relative temperature variation measured by the bolometers connected to Ch. 4 at different exposure time values and peak intensities, respectively; and (c, f) variation in the measurement resolution with exposure time values of the high-speed spectrometer and peak intensities, respectively. ....	64
Figure 3.12 (a, c) Reflection spectrum from the fiber-optic bolometers captured by the spectrometer without the attenuator and with the power balanced by the attenuators, respectively; (b, d) relative temperature variation for channels 2–5 without the attenuator and with the power balanced by the attenuators, respectively.....	66
Figure 3.13 (a) Reflection spectrum from the fiber-optic bolometers captured by the spectrometer with the power balanced by the attenuators for peak tracking; (b) relative temperature variation for channels 2–5 found from peak tracking.....	68
Figure 3.14 (a, c, e) System noise under 5, 10, and 100 Hz vibration, respectively, without a polarization scrambler; (b, d, f) system noise 5, 10, and 100 Hz vibration, respectively, when the polarization scrambler was on. ....	69
Figure 3.15 The response of the bolometers connected to channels 2 (a), 3 (b), 4 (c), and 5 (d) when each of them was exposed to a 0.1 Hz square wave power flux at $\sim 74$ W/m <sup>2</sup> . Insets are the close-up view of the falling transients of the responses. ....	71
Figure 3.16 (a–d) Measured SNR vs. power density for the bolometers connected to channels 2–5, respectively. ....	72
Figure 3.17 (a) Experimental set up for FOB radiation response in vacuum, (b) Time history change of temperature for square wave modulated radiation, (c) zoom in view of the falling temperature change. ....	75
Figure 3.18 Convolution theorem in time and frequency domain. ....	76

Figure 3.19 (a) Experimental set up for radiation test and to measure the incident radiation using photodetector (b)..... 77

Figure 3.20 (a) impulse response, (b) FOB output and (c) deconvoluted and photodetector signal. .... 78

Figure 3.21 Deconvolution algorithm (a) noise subtracted impulse response, (b) zoom in view which shows the temperature drift, (c) linear temperature drift removed, (d) overlapping six pulses with each other, (e) average of six impulse responses, (f) impulse response in frequency domain with actual amplitude using the power density of dc response, (g) FOB response with radiation of four pulses with different amplitude, (h) noise subtracted FOB response in time domain and drift compensated, (i) FOB response for four pulses in frequency domain, (j) input which can be found by dividing the output by the transfer function from (f), (j) converting the signal into double side with complex conjugate, and (l) input radiation with actual amplitude. .... 80

Figure 3.22 (a) FOB response for square modulated radiation, (b) Deconvoluted input and radiation measured by the photodetector. .... 81

Figure 3.23 (a) Schematic diagram of FOB with silicon pillar and gold disk, (b) Schematic diagram of the FOBs with Silicon heat sink, (c) microscopic image of the fabricated FOB with Silicon heat sink..... 81

Figure 3.24 (a) FOB response for the radiation modulated by square wave, (b) zoom in view of the falling edge. SB: sensing bolometer, RB: reference bolometer..... 83

Figure 3.25 (a) microscopic image of the FOB on silicon heat sink, (b) relative temperature variation for the FOB with silicon heat sink for square modulated radiation, (c) slowly rising/falling temperature compensation, and (d) zoom in view of the falling temperature..... 85

Figure 3.26 Experimental set up for testing the FOB in vacuum. .... 85

Figure 3.27 Deconvolution algorithm (a) overlapping of two impulse responses, (b) average of two impulse responses, (c) impulse response in frequency domain, (d) FOB response with the square modulated radiation, (e) chosen window of the noise subtracted FOB response in time domain, (f) FOB response in frequency domain, (g) input which can be found by dividing the output by the transfer function, (h) converting the signal into double side with complex conjugate with filter cut off 60Hz, and (i) reconstructed input radiation..... 86

## Chapter 1: Introduction

### 1.1. Background and Motivation of the work

Fiber-optic sensing platform gained popularity due to light weight, small size, immunity to electromagnetic interference, high temperature performance, electrical and optical multiplexing capabilities, large bandwidth, remote operation capability, resistance to harsh environment [1, 2]. Fiber-optic silicon Fabry-Perot interferometric sensor fabricated by attaching silicon pillar at the tip of the single mode fiber [3] is a good competitor as anemometer/bolometer with other existing electrical, mechanical and optical sensing technologies. The large thermo-optic coefficient and thermal expansion coefficient of the silicon compared to silica [4, 5] helps to get higher sensitivity compared to the sensors fabricated by mechanical deformation [6, 7] or the fiber Bragg grating sensor [8, 9]. Silicon Fabry-Perot interferometer (FPI) creates multiple peaks, in contrast to one from Fiber Bragg grating (FBG), where the central wavelength shifts as the optical path length is varied, primarily due to the temperature sensitivity of the index of refraction of Si, but also the thermal expansion of the pillar itself. Simultaneously measuring multiple peaks from the Fabry-Perot cavity spectrometer allows a reduction of the uncertainty in the change in temperature.

Utilization of this silicon tipped fiber-optic sensor in hot wire anemometry, flow or radiation measurement has many promising aspects compared to other available sensors.

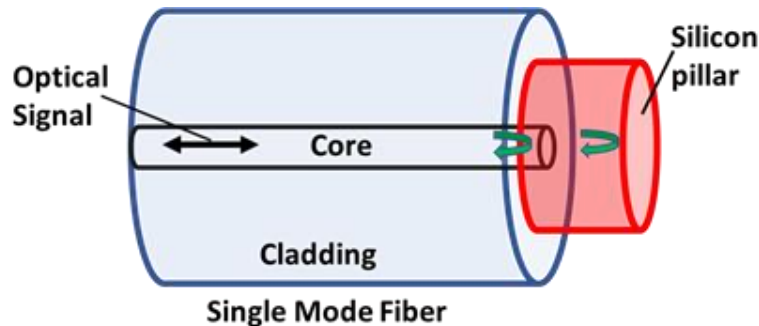


Figure 1.1 Schematic diagram of the silicon Fabry-Perot interferometric sensor.

The sensing element of interference-based sensor is fabricated by attaching a silicon pillar on the tip of fiber to generate a FPI as shown in Figure 1.1. The two reflecting surfaces that causes the Fabry-Perot interference are fiber-silicon pillar interface and silicon pillar-outside atmosphere. The light emitted from light source will transmit via fiber to the silicon pillar, then reflect and generate interference fringe. If refractive index of the silicon material is defined as  $n$  and length of the cylinder is denoted as  $L$ , it follows that

$$\left(N + \frac{1}{2}\right)\lambda_N = 2nL \quad (1.1)$$

where  $\lambda_N$  is the  $N$ th order peak wavelength,  $n$  and  $L$  are, respectively, the refractive index (RI) and the length of the FPI. Both RI and cavity length are a function of temperature, and thus the peak wavelength is dependent on the temperature following. Any temperature change outside of the silicon pillar will induce a wavelength change which is the result of index gradient and coefficient of thermal expansion of silicon pillar. The  $n^{\text{th}}$  order peak wavelength is given by

$$\lambda_N(T) = \lambda_N(0) + KT \quad (1.2)$$

where  $\lambda_N(0)$  is the initial wavelength and  $K$  is the sensitivity. The phase shift  $\Delta\phi$  produced by a temperature change  $\Delta T$  is given by

$$\Delta\phi = \frac{4\pi}{\lambda} \left(n \frac{dL}{dT} + L \frac{dn}{dT}\right) \Delta T \quad (1.3)$$

where  $n$  is the refractive index of the silicon,  $L$  is the cavity thickness and  $\lambda$  is the wavelength of light. The right-hand side of equation (1.3) includes the thermo-optic coefficient (TOC) and the thermal expansion coefficient (TEC). As demonstrated in [3], the silicon material is superior for temperature sensing due to its large TOC and TEC, compared to the silica material which is widely used in fiber-optic sensors.

A fiber-optic anemometer with a silicon FPI operates in two ways. First, it can be done without active heating. Through a fiber-optic circulator, a white light source is injected into the sensor head and the returned signal is directed to a high-speed spectrometer that is based on a transmission grating and a diode array operating in the 1550 nm wavelength window. Measurement speed is faster when the active heating is used for wavelength tracking corresponding to temperature change. Figure 1.2 (a) and (b) show the experimental set up for the temperature measurement without and with active heating, respectively. The spectral notch moves right or left with increasing or decreasing the ambient temperature which was shown in Figure 1.2 (c).

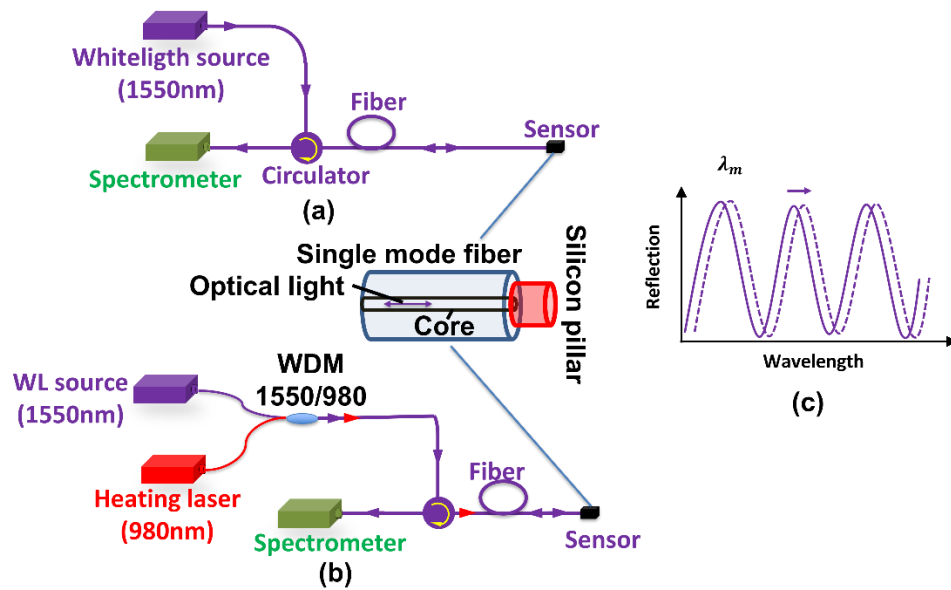


Figure 1.2 Schematic diagram of the thermometer operation without (a) and with (c) active laser heating, spectral notch shift from the temperature change (d). Inset shows the fiber-optic silicon Fabry-Perot interferometric sensor.

The convective heat transfer from water/air into the silicon pillar through its boundaries equal to the rate of increase of internal energy of the silicon pillar and vice versa. The temperature of the silicon pillar as a function of time and wavelength is a function of the heat transfer coefficient can be represented by

$$\lambda_n(T) = \lambda_n(0) + KT_w(t) + K \frac{P}{hA_s} \quad (1.4)$$

$$T(t) = T_\infty + \frac{P}{hA_s} + (T_0 - T_\infty)e^{-\frac{h A_s}{\rho C_p V}t} \quad (1.5)$$

where  $A_s$  is the surface area that exchanges heat,  $T_\infty$  is the temperature at steady state,  $T_0$  is the initial temperature and  $\rho$ ,  $C_p$ , &  $V$  are density, heat capacity and volume of the silicon pillar respectively.  $P$  should be zero when the active laser heating is not used. This temperature sensor was used as the anemometer for flow measurement with active heating.

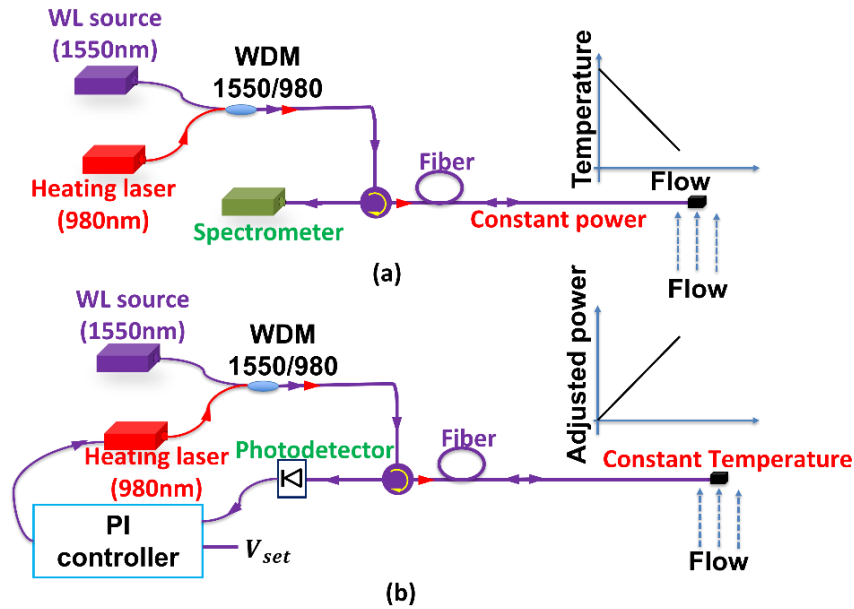


Figure 1.3 (a) Schematic diagram of the constant power operation and (b) constant temperature operation.

For the operation of fiber-optic anemometer with active heating, the sensing region is heated with a constant optical power and the measured temperature variation is used to deduce the flow velocity as shown in Figure 1.3 (a). This implementation, termed as “constant power (CP)” mode. Fiber-optic silicon anemometer can operate in another mode called “constant temperature (CT)” operation, where the temperature of the wire is kept constant by dynamically tuning the

heating current through a feedback control loop and the signal is the heating current. Constant temperature operation offers higher speed, higher 3 dB bandwidth of the frequency response, and a higher lifetime.

The silicon Fabry-Perot cavity has an ideal geometry for use as a bolometer. Bolometer can be designed by adding an absorber layer to the existing silicon FPI as shown in Figure 1.4 (b). Fiber-optic silicon bolometer with compact size, remote sensing capability, immunity to EMI, lower NEPD has made highly competitive to the other existing bolometry such as resistive bolometer, infrared video bolometer etc. The power flux from the plasma radiation can be made to fall directly on the absorber and then be conducted to the fiber. To measure the change in temperature, a white light source or narrow linewidth laser with scanning can be used for demodulation. Multichannel FOB using single light source and spectrometer helped to reduce the cost per channel and increase measurement range.

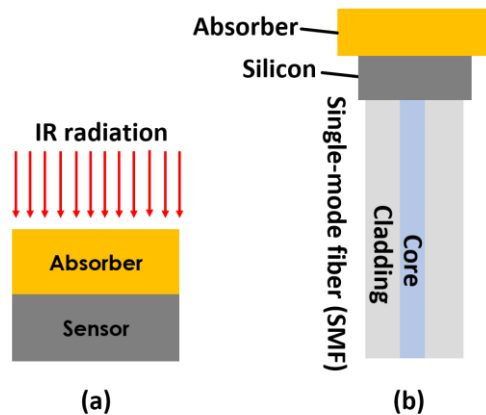


Figure 1.4 (a) Schematic diagram of the basic bolometer design and (b) extension of the fiber-optic silicon Fabry-Perot temperature sensor as bolometer.

This dissertation consists of a series of studies that allow for the development of fiber-optic Fabry-Perot interferometric sensor for the fast turbulence measurement, constant temperature operation of the anemometer, isotropic flow measurement, temperature compensation of the flow sensor, development of the bolometer using silicon FPI for radiation measurement, multichannel

bolometry system using simple bolometer structure, use of the bolometer with silicon heat sink in the vacuum with reduced time constant.

## **1.2. Organization of this report**

This dissertation is organized into four chapters, with this introduction being Chapter 1:. Chapter 2: and Chapter 3: are based on the findings on fiber-optic anemometer and bolometer, respectively. Section 2.1 provides theoretical and experimental results for constant temperature operation of the fiber-optic hot wire anemometer and its capability to dramatically increase the measurement speed of the device. Comparative study of the constant power mode and constant temperature mode was provided to gain high turbulence measurement speed along with high 3 dB frequency. A feedback system was used to keep the sensor temperature fixed irrespective of the ambient temperature change to measure the flow. This is the first-time study of the constant temperature study for fiber-optic sensor where analogous study for electronic operation were available.

Section 2.2 presents a detailed analysis of the utilization of the fiber-optic sensor with silicon FPI in the water flow measurement. It is also shown that the heat loss is strongly dependent on the flow directivity, because of the cylindrical shape of the silicon FPI. Theoretical and experimental results are provided of a new sensor structure for the measurement of flow with reduced directivity. The sensor consists of a laser-heated silicon FPI embedded in a metal microsphere. Herein, the spherical shape of the outside metal shell gives a much more symmetric response to the flow direction; thus, the directivity is reduced greatly. Section 2.3 provides the technique for temperature compensation of the water which can have influence in the flow speed measurement.

Section 3.1 presents the comprehensive analysis of the bolometer fabrication and experimental procedure to increase the detection limit from the previous design with improved NEPD and responsivity by adding a large gold disk for radiation absorption.

In section 3.2 we present an investigation on the development of a multichannel fiber-optic bolometry system with five bolometers connected to each channel of the coarse wavelength division multiplexer (CWDM), a single light source of super luminescent LED (SLED) and a single I-MON 512 OEM spectrometer. Bolometers with simple structure and a robust multichannel bolometry system can measure radiation with the same NEPD and higher responsivity compared to the scanning laser-based bolometry system which reduces the cost per channel and sensor fabrication complexity. Section 3.3 presents the bolometer performance incorporating a heat sink with the previous design and a deconvolution method for getting better temporal response.

Chapter 4 concludes this dissertation with a summary of the results obtained, and possible directions for future work.

## **Chapter 2: Turbulence measurement by Anemometer**

### **2.1. Constant temperature operation of the fiber-optic hot wire anemometer**

In this section, we present the theoretical and experimental study of the operation of the anemometer. This section begins with the introduction of constant temperature operation of the anemometer and advantages compared to the constant power operation. Theoretical analysis is shown in the following section which provides the comparative results for the two types of fiber-optic hot wire anemometer operation for the measurement speed and 3 dB frequency. Experimental results show the proof of the concept of the constant temperature operation for the flow measurement. This section contains the contents from [10] which have been reproduced with permission from OSA Publishing Group.

#### **2.1.1. Introduction**

Hot wire anemometry (HWA) has become an essential tool in the study of turbulent flows thanks to their relatively high spatial and temporal resolutions in measuring flow velocity. It is based on the forced convective heat transfer from a heated wire to the surrounding flow. In conventional HWA, the wire is heated by electronic current, and the temperature of the wire is measured through the temperature-dependent resistance of the wire. Recently, fiber-optic HWA, in which both the heating of sensing element and temperature measurement are achieved optically, has received extensive attention due to the many advantages over conventional electronic HWA, such as immunity to electromagnetic interference, resistance to harsh environment, and capability of placing the sensor in remote locations. The sensing region of the fiber is made absorptive to light for optical heating by incorporating light-absorptive elements or materials into the fiber and temperature measurement is mainly achieved by fiber-Bragg gratings (FBGs) inscribed in the sensing region of the fiber [11-15]. For the operation of reported fiber-optic HWA, the sensing

region is heated with a constant optical power and the measured temperature variation is used to deduce the flow velocity. This implementation, termed as “constant power (CP)” mode here, is analogous to the “constant-current (CC)” operation in conventional electronic HWA, where the heating current of the wire is kept constant, and the output signal is the temperature of the wire which is a function of the flow. It is well known that conventional HWA can operate in another mode called “constant temperature (CT)” operation, where the temperature of the wire is kept constant by automatically adjusting the heating current through a feedback control loop and the output signal is the heating current [16]. The advantages of CT operation over CC operation have been well recognized in conventional HWA. Because the wire temperature is kept constant, the effect of thermal inertia of the wire is suppressed, resulting in significantly increased measurement speed [16]. The sensitivity of HWA is affected by the temperature differential between the wire and the flow; therefore, the performance is more consistent for CT operation than for CC operation because the temperature differential is kept constant in CT mode. Finally, CT operation avoids the thermal cycles experienced by the wire in CC operation that may reduce the lifetime of the anemometer.

Although CT operation has been the mostly adopted operation mode in electronic HWA, its equivalence in fiber-optic HWA has not been reported. In this chapter, we demonstrate the CT operation of a fiber-optic anemometer and its capability to dramatically increase the measurement speed of the device. The anemometer used for demonstration is based a silicon low-finesse Fabry-Perot interferometer (FPI) attached to the tip of a single-mode fiber [17]. By exposing the silicon FPI to 980 nm radiation to simulate the flow-induced temperature variations, we studied the step response and frequency responses of the fiber-optic anemometer operated in both CP mode and CC mode. The results show that that the 3 dB bandwidth of the frequency response was increased

from 0.5 Hz for the CP operation to 2 kHz for CT operation. The response of the anemometer also shows good linearity to the radiation power. These benefits make the CT operation of fiber-optic HWA attractive for measuring turbulent flows.

### 2.1.2. Experimental set up and principle of operation

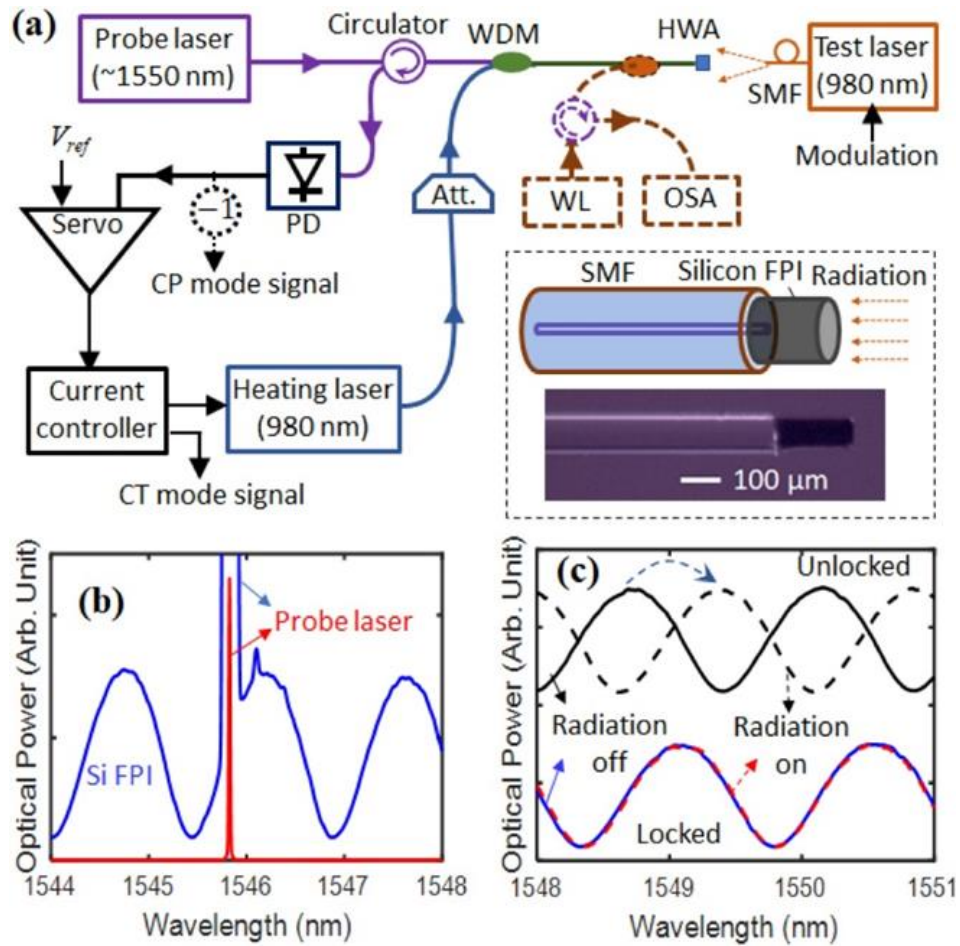


Figure 2.1 (a) Schematics of the experimental setup to study the CT operation of a fiber-optic anemometer (the inset shows the structure and a microscope image of the anemometer consisting of a silicon FPI at the tip of an optical fiber; Att., attenuator). (b) Spectrum measured by the optical spectrum analyzer (OSA) with blue and red curves plotted in different scales. (c) Spectral response of the silicon FPI to the test laser when the system was under locked and unlocked conditions (for clarity, an offset is added to the solid black and dashed black curves).

The experimental setup to study the CT operation of a fiber-optic anemometer is schematically shown in Figure 2.1 (a). The inset in Figure 2.1 (a) shows the structure and a microscope image of the anemometer. It was fabricated by splicing a small silicon pillar (100  $\mu\text{m}$

diameter and 200  $\mu\text{m}$  thickness) to the cleaved end of an SMF using the method described in Ref. [18]. The silicon pillar functions as an FPI due to the fiber–silicon and silicon–air interfaces that partially reflect the light from the fiber. The silicon FPI was placed in static air environment and was heated by a 980 nm diode laser (heating laser). This wavelength was selected because of the good absorption of silicon (the penetration depth of silicon at 980 nm is  $\sim 104 \mu\text{m}$  at room temperature [19] and the availability of high-power, low-cost, and small-footprint lasers at this wavelength. Temperature change was measured using a distributed-feedback (DFB) diode laser (probe laser) around 1550 nm, at which silicon is highly transparent. Both the heating laser and the probe laser were combined into the pigtail fiber leading to the anemometer through a 980/1550-nm wavelength division multiplexer (WDM). The probe light reflected from the silicon FPI was directed to a photodetector (PD) through a fiber-optic circulator. When the probe laser wavelength was on the slope of the spectral fringes of the FPI, the spectral shift of the FPI fringes caused by temperature changes (with a sensitivity of  $84.6 \text{ pm}/^\circ\text{C}$ ) [3] was then converted to power variations that were measured by the PD. For CT operation, a commercial servo controller (Model LB1005, New Focus) was used to lock the temperature of the FPI. The servo controller compared the voltage output of the PD and a reference voltage signal ( $V_{\text{ref}}$ ) that was used to set the locking point. The differential voltage (error signal) was then amplified and filtered to control the heating laser power through a laser current controller. When the system was in a locked state, the feedback loop kept the temperature of the silicon FPI constant by adjusting the heating laser power. The monitoring voltage output from the current controller, which was proportional to the heating laser current and proportional to the laser power over the operation range in the experiment, was regarded as the CT operation signal. At the initial stage of the experiment, a white-light system, including an amplified spontaneous emission (ASE) white-light source, a circulator, and an optical spectrum analyzer

(OSA), was incorporated into the anemometer system through a coupler to measure the reflection spectrum of the silicon FPI. For CP operation, the servo controller as well as the heating laser was turned off. The wavelength of the probe laser was tuned to the position on the spectral fringes of the silicon FPI with maximum slope. The opposite of the signal from the PD was considered as the CP mode signal. The opposite of the signal from the PD was used because, in this case, the probe laser line happened to be set at a position of the fringes with a negative slope.

It is cumbersome to generate step-change flows or flows with precisely controlled frequencies for direct testing of the frequency response of anemometers. Rather, we exposed the silicon FPI to the external radiation from another fiber-pigtailed 980 nm laser (test laser), as shown in Figure 2.1. The distance between the end face of the pigtail of the test laser and the silicon FPI was around 2 mm. By modulating the laser intensity, we simulated the changes in the heat transfer from various flow conditions such as step-change flows and sinusoidal flows of different frequencies. Different levels of radiation received by the silicon FPI were equivalent to the different flow velocities applied on the anemometer. This indirect test method is analogous to the electrical testing method commonly used for conventional HWA, where a perturbation or modulation to the wire current is introduced and the response of the anemometer is observed [20].

The red curve in Figure 2.1 (b) is the spectrum measured by the optical spectrum analyzer (OSA) when the system was in locked state. The spectrum is dominated by the probe laser line with a large spectral density. The enlarged view of the spectrum (blue curve) reveals the sinusoidal fringes from the ASE sources. The relative position between the laser line and the spectral fringes of the FPI shows that the locking point was on the positive slope of the fringes. Figure 2.1 (c) shows the reflection spectrum of the silicon FPI at various conditions of the system measured by the OSA. After the heating laser was turned on, we measured the reflection spectrum of the

silicon FPI in unlocked state, shown as a solid black curve in Figure 2.1 (c). Then we turned on the test laser, and the radiation from the test laser increased the temperature of the silicon FPI, causing  $\sim 1.0$  nm shift of the fringes toward longer wavelength, shown as the dashed black curve in Figure 2.1 (c), which is equivalent to a temperature increase of  $\sim 12.5$  °C. Next, we turned off the test laser then activated the locking system; the reflected spectrum of the silicon FPI is shown as the solid blue curve in Figure 2.1 (c). Then, under the locked state, we turned on the test laser with the same power that had increased the temperature of the silicon FPI by  $\sim 12.5$  °C under the unlocked state. The spectrum, shown as the dashed red curve in Figure 2.1 (c), coincided with the solid blue curve, which verified that the locking system kept the temperature of the silicon FPI constant before and after the testing laser was turned on.

### **2.1.3. Theoretical analysis**

In this section, constant temperature operation of fiber-optic hot wire anemometer was studied theoretically. First, the transfer function was deduced from the experimental approach used to demonstrate constant temperature operation. Transient characteristics were compared for a step input as a simulation of the flow for both constant temperature and constant power operations along with the frequency response. Theoretical results show that response time is shorter, and the 3 dB frequency is higher for constant temperature operation compared to constant power operation. The theoretical result is overestimated due to the assumption of different constants, as it is hard to find straightforward approach to find the constant equivalent for experimental condition. Overall, this study will provide the prospect of constant temperature operation over constant power operation to be used in high-speed turbulence measurements. In the case of a constant temperature mode, reflected optical power from the temperature sensor was taken as the input to the feedback controller through a photodetector (PD) as shown in Figure 2.1 (a). The feedback system was used

to keep the wavelength constant providing equivalent variable power to the heating laser corresponding to the atmospheric temperature change as shown in Figure 2.1 (a). The radiation laser is used to heat the sensor to introduce temperature change externally to simulate flow. The reflected power from the sensor due to the radiation was converted to a voltage using a photodetector (PD). The reference voltage is the PD output after locking before applying radiation. A proportional integral (PI) controller was used to determine how much power needed to be injected in the laser controller to lock the laser in the sensor spectrum. The feedback-controlled laser source then delivered the required power to the sensor. The radiation laser was used as the input and the laser power required to compensate for temperature effects was the output. This phenomenon is shown in Figure 2.2 (a). Figure 2.2 (b) shows the transfer function of the constant power mode.

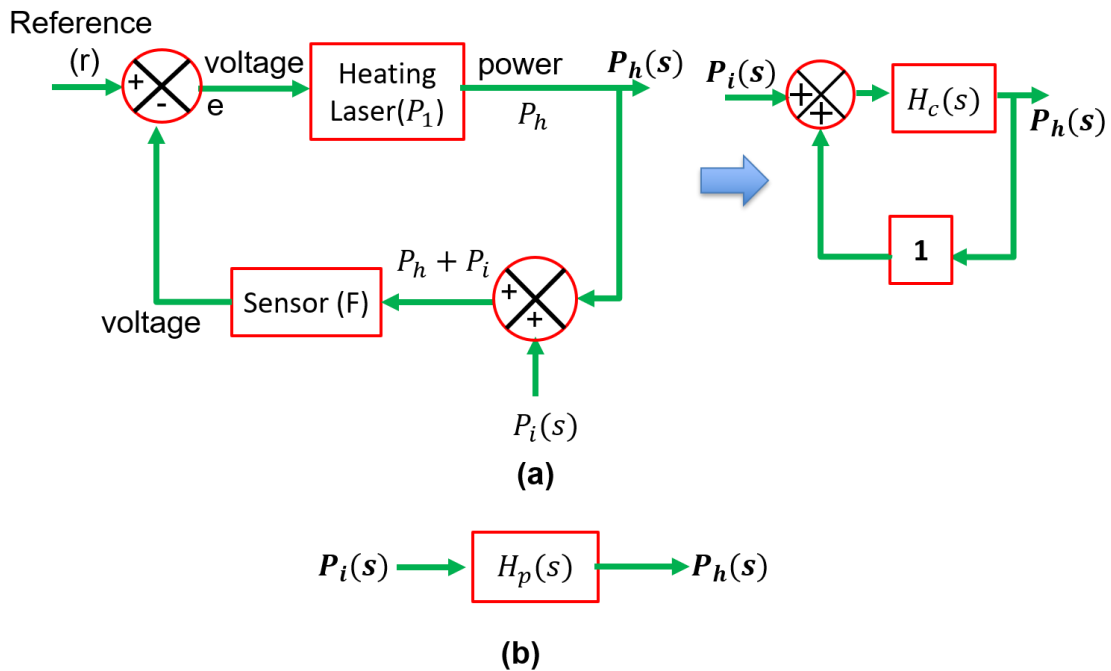


Figure 2.2 Transfer function of the constant temperature (a) and constant power operation (b) of fiber-optic hot wire anemometer.

The photodetector voltage,  $V_{sig}(t)$  depends on the sensor ambient temperature as

$$V_{\text{sig}}(t) = V_0 + K_\lambda \Delta\lambda = V_0 + K_D T_s(t) \quad (2.1)$$

where  $V_0$  is the initial voltage,  $K_D$  is the proportional constant for converting voltage from temperature and  $T_s$  is the temperature of the sensor.

The difference between the voltage when the system is locked ( $V_{\text{set}}$ ) and the voltage corresponding to the ambient temperature ( $V_{\text{sig}}(t)$ ) is the error voltage,  $e(t)$ . It can be expressed as

$$e(t) = V_{\text{set}} - V_0 - K_D T_s(t) \quad (2.2)$$

The differential amplifier input of the feedback control system will be the error signal. The output of the differential amplifier was controlled by the PI controller. The output from the PI controller depends on the error voltage as

$$u(t) = K_p e(t) + K_i \int_0^t e(\tau) d\tau \quad (2.3)$$

where  $K_p$  and  $K_i$  are the proportional and integral constant of the PI controller. The PI controller output will be input of the heating laser and the output of the heating laser is the system output for the constant temperature operation. The system input is the radiation coming from the test laser. The characteristic equation of the system output is

$$P_h(t) = k_{\text{sys}} u(t) + P_0 \quad (2.4)$$

where  $P_0$  is the initial power and  $k_{\text{sys}}$  is the constant for converting the PI controller voltage to laser power. Temperature produced from the heating and radiation laser is governed by the following equation [11]

$$T_s(t) = T_w + \frac{P(t)}{hA_s} + (T_0 - T_w - \frac{P(t)}{hA_s}) \exp(-\tau t) \quad (2.5)$$

where  $\tau = \frac{hA_s}{\rho_s C_s V_s}$ ,  $A_s$  is the surface area for heat exchange,  $T_w$  is the wind temperature,  $P$  is the heating power within the silicon wafer,  $\rho_s$ ,  $C_s$  and  $V_s$  are respectively, the density, the thermal capacity, and the volume of the silicon pillar [20]. Transfer function of each block can be found from the characteristic equation depending on the input and output. The PI controller transfer function is given by the following equation where  $e(s)$  and  $u(s)$  are the input and output of the PI controller.

$$C(s) = \frac{u(s)}{e(s)} = K_p + \frac{K_i}{s} \quad (2.6)$$

The heating laser transfer function is the ratio of the heating laser output  $p_h(s)$  to the PI controller output  $u(s)$ .

$$P_h(s) = \frac{p_h(s)}{u(s)} = K_{sys} \quad (2.7)$$

The overall transfer function of the  $C(s)$  and  $P_h(s)$  is shown by the heating laser transfer function  $P_1(s)$  shown in Figure 2.2 (a).

$$P_1(s) = K_{sys}K_p + \frac{K_{sys}K_i}{s} \quad (2.8)$$

The transfer function of the temperature produced from the sensor due to the heating laser, considering the input power as  $P_0$  is

$$\frac{T_{sh}(s)}{P_0/s} = \frac{\frac{1}{\tau}}{hA_s(s + \frac{1}{\tau})} \quad (2.9)$$

The relationship between temperature and voltage can be considered linear for a certain temperature range. The transfer function for the photodetector is

$$D(s) = K_D \quad (2.10)$$

The transfer function of the radiation laser and measured by the sensor for a step function input is given by

$$\frac{T_{sr}(s)}{1/s} = \frac{\frac{1}{\tau}}{hA_s(s + \frac{1}{\tau})} \quad (2.11)$$

The overall transfer function of the  $T_{sh}(s)$ ,  $T_{sr}(s)$  and  $D(s)$  are combined to obtain the overall sensor transfer function  $F(s)$ .

$$F(s) = \frac{K_D \frac{1}{\tau}}{hA_s(s + \frac{1}{\tau})} \quad (2.12)$$

Considering the derived transfer function of each block, the overall transfer function for constant temperature,  $H_c(s)$  and constant power,  $H_p(s)$  are given by

$$H_c(s) = \frac{As + B}{s^2\tau + (1 + A)s + B} \quad (2.13)$$

where  $A = \frac{K_{sys}K_DK_p}{hA_s}$  and  $B = \frac{K_{sys}K_DK_i}{hA_s}$

$$H_p(s) = \frac{K_D}{(s\tau + 1)hA_s} \quad (2.14)$$

$K_{sys}$ ,  $K_D$  were experimentally found by recording the output from the photodetector for the corresponding input power. Typical value of  $K_p$  and  $K_i$  were used which were found from the Routh table using the transfer function for a stable system.

Figure 2.3 (a) and (c) shows the step response for constant temperature and constant power operation, respectively. Response time in constant temperature operation (0.6 ms) is found to be shorter compared to the constant power mode (3.1 s). 3 dB frequency was found to be 2.4 kHz and 0.43 Hz for constant temperature and constant power mode, respectively.

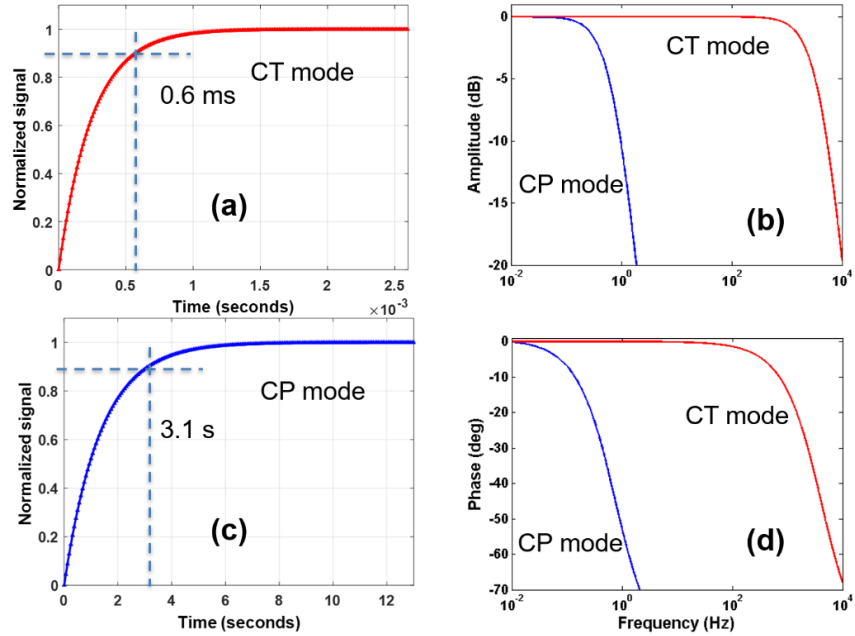


Figure 2.3 Step response of the fiber-optic anemometer operated in constant temperature operation (a) and constant power operation (c) respectively. Amplitude (b) and phase response (d) of the transfer function for CT and CP operation.

#### 2.1.4. Experimental Results

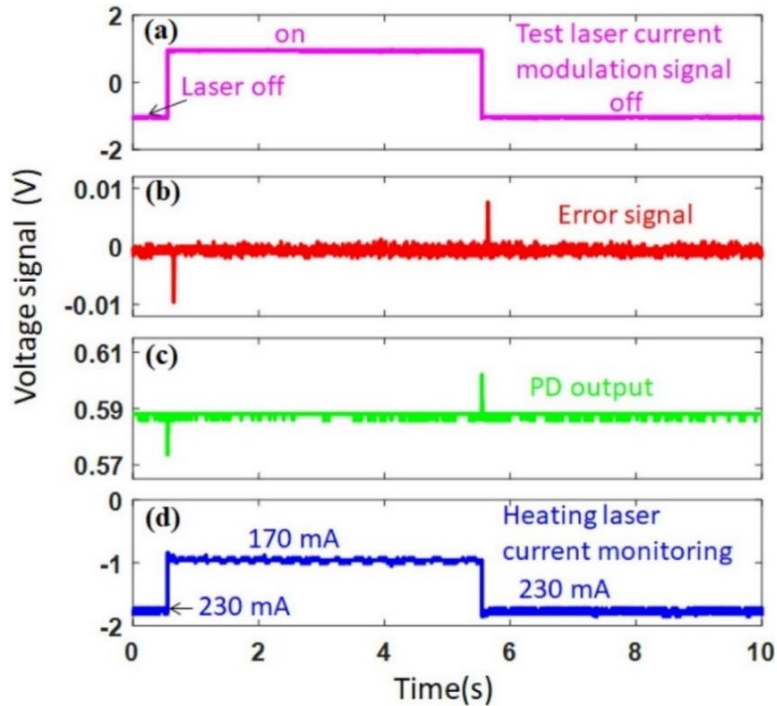


Figure 2.4 Control and monitor signals of the feedback control system when the anemometer is operated in CT mode.

We removed the white-light system in Figure 2.1 (a) and further studied the locking process by recording different signals of the feedback system, as shown in Figure 2.4, when the system was in the locked mode and the anemometer was excited with step changes of radiation. The current of the test laser was modulated by a 0.1 Hz, 2 V peak-to-peak square wave, as shown in Figure 2.4. The modulation signal produced a current alternating between 0 mA and 200 mA that turned on and off the testing laser (step excitation). The feedback system continuously monitored the PD output, as shown in Figure 2.4 (c) and tried to keep the FPI at a constant temperature by adjusting the power of the heating laser. The initial locking was confirmed by the zero-error signal shown in Figure 2.4 (b). At  $t=0.5$  s, as the sensor was exposed to the radiation from the test laser, the spectrum of the sensor tried to shift toward the longer wavelength and move out of the locking position. The PD output deviated from the reference voltage indicated by the deviation of the error signal from zero at the time of the step change of the radiation power. The locking system reduced the current of the heating laser from  $\sim 230$  mA to  $\sim 170$  mA (corresponding to monitor voltage change from approximately  $-2$  V to  $-1$  V) to maintain the wavelength position of the sensor, as shown in Figure 2.4 (d). Note that optical attenuation was introduced to the heating laser path to ensure the laser was operated well above the laser threshold where good linearity between laser power and current was maintained. The feedback system brings back the FPI spectrum to the locking wavelength position. The repositioning of the FPI spectrum wavelength to the locking position was confirmed by the zero-error signal after the deviation. Another perturbation occurred when the test laser was turned off and the radiation returned to zero at  $t=5.5$  s. Similarly, the error signal deviated from zero for a short period of time for this change, and the feedback control system increased the current of the heating laser from  $\sim 170$  mA to  $\sim 230$  mA to maintain the same PD output, which in turn maintained the temperature of the FPI. The relocking process was completed

when the error signal returned to zero. As discussed earlier, the monitor signal of the heating laser current is regarded as the CT mode signal [Figure 2.4 (d)], which changed according to the radiation power of the test laser [Figure 2.4 (a)] used for simulating changes in flow velocities.

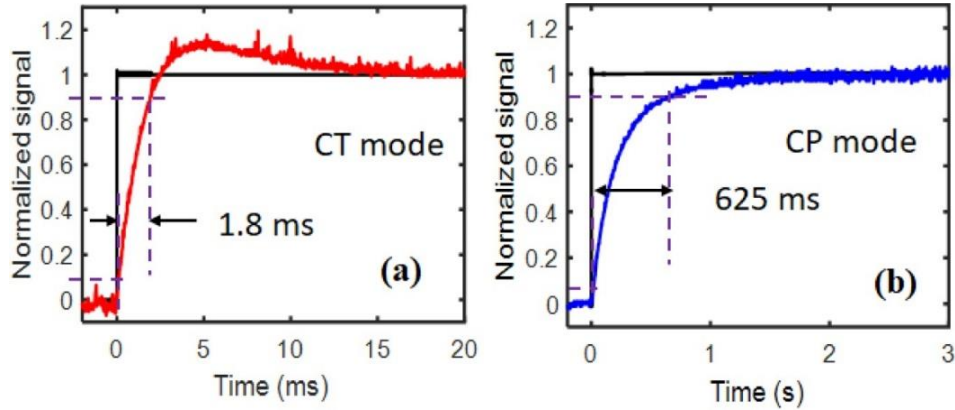


Figure 2.5 Step response of the fiber-optic anemometer when operated in CT mode (a) and CP mode (b).

To demonstrate the benefit of the CT operation for improved measurement speed, the transient response of the anemometer to step excitation in CT mode was studied in detail and compared with results obtained in CP mode. Figure 2.5 (a) shows the normalized signal in response to a step increase in radiation power when the system was operated in CT mode (red curve) and the step function was used to modulate the current controller for the test laser (black curve). The transient response resembles that of a typical underdamped second-order system as the normalized signal rose from zero with an overshoot before it settled at the final steady-state value. The rise time, defined as the time taken by the signal to change from 10% to 90% of the steady-state value, was found to be 1.8 ms. To verify that the response time was attributed mainly to the anemometer and the feedback control system rather than the finite response time of the test laser power to the modulation, we measured the power of the test laser in response to the step modulation using a high-speed PD and found that response time was only 10  $\mu$ s, much shorter than the response time of the anemometer system. For comparison, we recorded the step response of the same

anemometer operated in CP mode when the servo controller was turned off (open loop operation). Figure 2.5 (b) shows the inverted voltage signal from the PD (blue) and the modulation signal for the test laser controller (black). The transient response is consistent with that of a first-order system, and a rise time of 625 ms was found for the CP operation, more than 300 times larger than that for the CT operation.

We then obtained the transfer function of the fiber-optic anemometer. To this end, the radiation power from the test laser was modulated with sinusoidal functions at different frequencies, and the output signal from the anemometer system, which was also sinusoidal curves, was recorded. Comparing the amplitude and phase between the excitation signal and system output signal yields the transfer function of the anemometer system. For example, Figure 2.6 (a) shows the response (red) of the anemometer operated in CT mode to an excitation signal (blue) at 30 Hz. The response has a peak-to-peak output of 0.52 V and a small phase delay of  $\sim 5^\circ$  compared to the excitation signal. When the excitation frequency was increased to 3 kHz (the amplitude of the excitation remained unchanged), as shown in Figure 2.6 (b), the response exhibited a decrease in amplitude (a 7.5 dB reduction from 0.52 V to 0.22 V) and an increase in phase delay (from  $5^\circ$  to  $97^\circ$ ). The amplitude of the transfer function for both CT and CP modes is shown in Figure 2.6 (c). Note that the amplitude is normalized to the response toward dc excitation. The 3 dB bandwidths are estimated to be 2 kHz for CT operation and only 0.5 Hz for CP operation, proving that CT operation can dramatically improve the frequency response of a fiber-optic anemometer. The phase of the transfer function for both CT and CP modes is shown in Figure 2.6 (d). The CT mode shows no significant phase delay for the frequency range  $< 200$  Hz and a phase delay close to  $90^\circ$  at the 3 dB frequency of 2 kHz. For comparison, the CP operation shows a phase delay of  $\sim 40^\circ$  at its 3 dB frequency of 0.5 Hz.

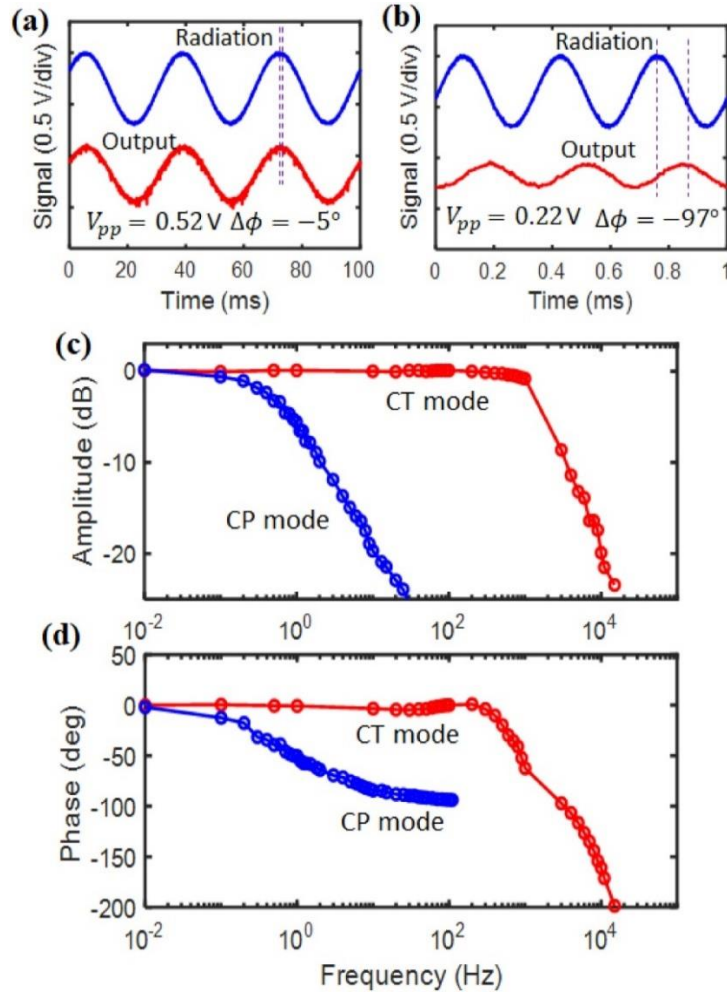


Figure 2.6 Step response of the fiber-optic anemometer when operated in CT mode (a) and CP mode (b).

Finally, we studied the linearity of the anemometer operated in CT mode. Figure 2.7 shows the output of the anemometer measured at different radiation power levels from the test laser and the linear fitting of the data. Note that only a small fraction of the radiation power was absorbed by the anemometer because the divergence of the laser beam when it exited the pigtail SMF of the test laser. The output signal is a voltage indicative of the current applied to the heating laser and is proportional to the heating laser power. The signal increased from  $-2.43 \text{ V}$  to  $-2.29 \text{ V}$  with the increasing of the radiation power from 0 to 60mW. The heating laser current decreased from 123.8

mA to 116.9 mA accordingly. The output signal vs radiation power was found linear with the coefficient of determination  $R^2 = 0.995$ .

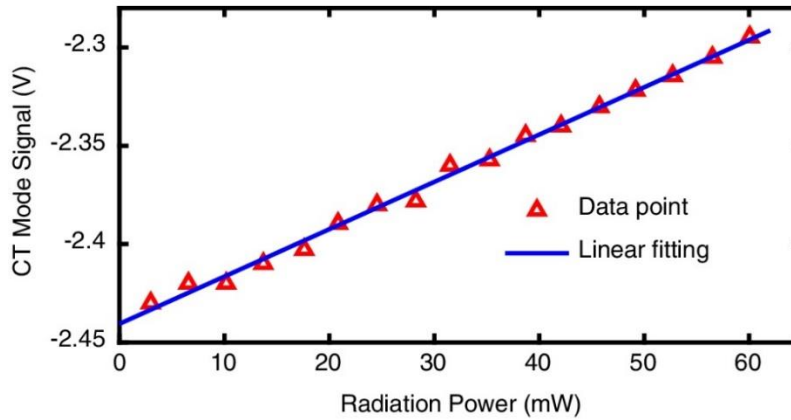


Figure 2.7 Output signal versus radiation power from the test laser.

### 2.1.5. Summary

In summary, we have studied the CT operation of a laser-heated fiber-optic hot-wire anemometer where the temperature of the FPI is kept constant by adjusting the heating laser power through a feedback control loop and the signal is the heating laser power. We show that the CT operation can dramatically improve the frequency response over the commonly used CP operation where the laser heating power is kept constant, and the signal is the temperature of the FPI. The fiber-optic anemometer is based on a 100  $\mu\text{m}$  diameter, 200  $\mu\text{m}$  thick silicon FPI and heated by a 980 nm diode laser. The 10%-90% rise time of the step response was reduced from 650ms for CP operation to 2 ms for CT operation, an improvement of more than 300 times. Compared with the CP operation, the CT operation also exhibited a dramatic increase in the 3 dB bandwidth from 0.5 Hz to 2 kHz. The response of the anemometer also shows good linearity to the radiation power. The significantly improved frequency response and linear response make fiber-optic hot-wire anemometers attractive for measuring turbulences with rapidly changing flows.

## **2.2. Reduction of directivity of the fiber-optic water flow sensor**

In this section, we present a detailed analysis of the utilization of the fiber-optic silicon Fabry-Perot anemometer as the water flow sensor. Fiber-optic flow sensor based on a laser-heated silicon Fabry-Perot interferometer (FPI) exhibits a strong directivity owing to the cylindrical shape of the sensor head. In this work, a new sensor structure has been designed to effectively reduce the directivity. Changing the shape of the flow sensor from cylindrical to spherical helps to get uniform response. Theoretical and experimental results are shown for the validation of the concept for uniform response.

This section contains all the contents from [21] which have been reproduced with permission from SPIE.

### **2.2.1. Introduction**

Flow measurement is a key technique for many industrial applications. As a promising platform, optical fiber flow sensors have been extensively investigated. Among them, many fiber-optic sensors are based on mechanical deformations or hot wire anemometry [22-26]. Recently, we proposed a fiber-optic hot-wire anemometer using a laser heated silicon Fabry-Perot interferometer (FPI) attached to tip of a cleaved single-mode fiber (SMF) [17, 27]. Wavelength shift of the heated silicon FPI is a function of the flow speed, attributed to the dependence of heat loss on the flow speed. This sensor has shown a large dynamic range in water [28] and excellent sensitivity (especially in the low speed end) in comparison to commercial water flowmeters [29]. It is also shown that the heat loss is strongly dependent on the flow directivity as well [28], because of the cylindrical shape of the silicon FPI, as seen in Figure 2.1 (a). The forced convective heat loss is strongly affected by the flow direction relative to the shape of the laser-heated silicon pillar. This strong directivity is usually an advantage if the extra direction information besides the flow

speed is obtained, which is why a vector flow sensor [30] was devised for measuring the flow microstructures of turbulence in water [31]. However, reliable reconstruction of the flow vector is a complexed process and may need multiple sensors to work simultaneously.

In cases where knowledge of flow direction is not demanding, a flow sensor that reliably reads the flow speed only may be enough. In this report, we investigate a new sensor structure for the measurement of flow with reduced directivity. The sensor consists of a laser-heated silicon FPI embedded in a metal microsphere, as seen in Figure 2.8 (b). A similar sensor has been proposed for the measurement of electric current [32]. Herein, the spherical shape of the outside metal shell gives a much more symmetric response to the flow direction; thus, the directivity is reduced greatly. Experiments have been carried out to determine the directivity of the new flow sensor.

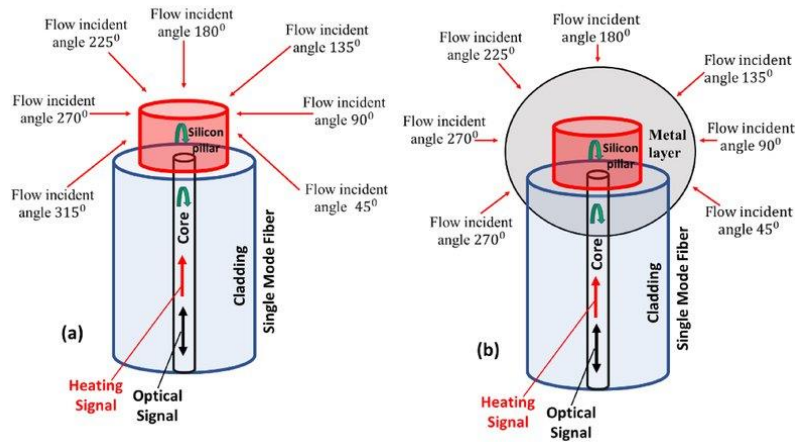


Figure 2.8 Schematic diagram of the sensor with (a) only silicon pillar and (b) silicon pillar embedded in a metal sphere.

### 2.2.2. Principle of operation

The peak or valley wavelengths of the silicon FPI can be expressed as

$$\lambda(T) = \lambda(0) + KT \quad (2.15)$$

where  $\lambda(0)$  is the initial wavelength and  $K$  is the temperature sensitivity. As will be shown later, the sensor was made by carefully embedding the silicon pillar attached to a single-mode fiber to a

small melt tin sphere, therefore, the silicon pillar is in tight contact with the tin sphere when it cools down. The small size and high thermal conductivity of the tin sphere along with the tight contact with the silicon FPI, which also has a high thermal conductivity, lead to a lumped analysis model for sensor [3]. Thus, a simple expression is reached to relate the temperature of the sensor head with laser heating [33].

$$T(t) = T_{\infty} + \frac{P}{hA_s} + \left(T_0 - T_{\infty} - \frac{P}{hA_s}\right) e^{-\frac{h A_s t}{\rho C_p V}} \quad (2.16)$$

where  $T(t)$  is the temporal temperature of the silicon pillar,  $A_s$  is the surface area exposed to the air,  $T_{\infty}$  is the temperature of air,  $P$  is the heating laser power absorbed by the silicon pillar, and  $\rho$ ,  $C_p$ , and  $V$  are, respectively, the density, the thermal capacity, and the volume of the silicon pillar. When the flow direction changes, if the minute temperature dependence is ignored, all the parameters are constant except the heat transfer coefficient (HTC)  $h$ . The HTC is dependent on the flow direction and is related to Nusselt number  $Nu$  through [34-39].

$$Nu = \frac{hD}{k} \quad (2.17)$$

where  $D$  is the characteristic length,  $k$  is the thermal conductivity of the flow medium. The  $Nu$  number for water flowing over a spherical cylinder object was proposed by Whitaker and is expressed as [34, 40]

$$Nu_{sph} = \frac{hD}{k} = 2 + \left[0.4Re^{1/2} + 0.06Re^{2/3}\right] Pr^{0.4} \left(\frac{\mu_{\alpha}}{\mu_s}\right)^{1/4} \quad (2.18)$$

where  $Re$  is the Reynold number and  $Pr$  is the Prandtl number, which are given, respectively, by

$$Re = \frac{\rho_f v D}{\mu} \quad (2.19)$$

where  $\rho_f$ ,  $v$  and  $\mu$  are the density, velocity of the fluid and the kinetic viscosity. Again, the Prandtl number is a measure of relative thickness of the velocity and thermal boundary layer. The Prandtl number determines the fastness of the heat diffusion which is given by

$$Pr = \frac{\mu C_p}{k} \quad (2.20)$$

Again, the Nu number for water flowing over a cylindrical object was proposed by Churchill and Bernstein and is expressed as [35]

$$Nu_{cyl} = \frac{hD}{k} = 0.3 + \frac{0.62Re^{1/2}Pr^{1/3}}{[1 + (0.4Pr)^{2/3}]^{1/4}} \left[ 1 + \left( \frac{Re}{282000} \right)^{5/8} \right]^{4/5} \quad (2.21)$$

The difference in calculating the Nu number for different shapes (i.e., Equations (2.18) and (2.21)) clearly indicates that the heat loss would be significantly different for flow from different directions. However, for the spherical sensor shown in Figure 2.8 (b), the directivity is greatly reduced because of the symmetrical geometry, except the flow from the lead-in fiber. Nevertheless, this effect can be mitigated by making the metal shell larger, but with the cost of decreased response speed and increased mechanical instability of the sensor in the water.

### 2.2.3. Sensor fabrication and experimental procedure

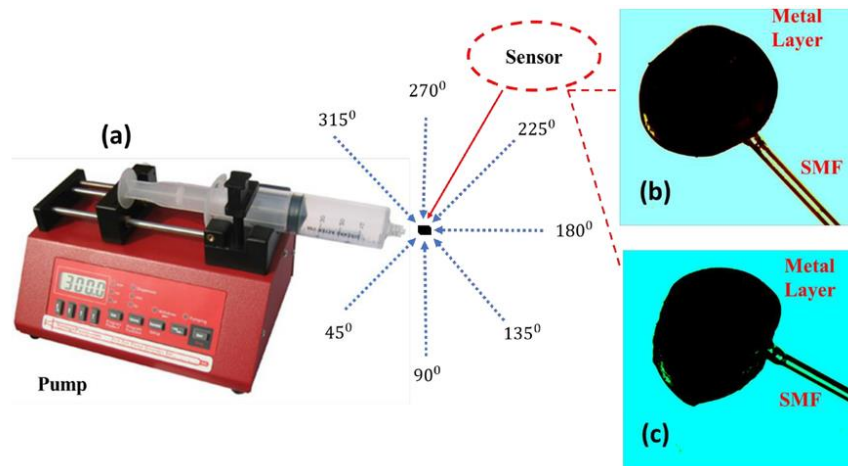


Figure 2.9 Measurement of the sensor directivity, (a) Definition of incident angle of the flow. and (b), (c) images of the sensor taken from two different angles.

The sensor was prepared following the similar process described in [32]. First, a silicon pillar with 200  $\mu\text{m}$  thickness and 100  $\mu\text{m}$  diameter was attached to the cleaved end face of a piece of single-mode fiber using fusion splicing. A portion of solder wire was melted and formed into a small sphere using a heated soldering iron. Then, the final sensor head was obtained by inserting the silicon pillar into the melted tin ball. In the meantime, the sensor spectrum was continuously monitored throughout the process to make sure that sensor has a good reflection spectrum. The experimental set up for measuring the flow of water was the same as the one described in the previous work [27]. Briefly, a white light source was incident on the silicon FPI through a fiber-optic circulator. As silicon is transparent in 1550 nm wavelength, the reflected light from the first surface and second surface creates interference which is detected by a high-speed spectrometer (I-MON 256 USB, Ibsen). A 980 nm heating laser (LC95A74, Bookham) was used to heat the sensor. Water flowed continuously at a rate of 1.4 m/s from the syringe pump to the sensor head. Figure 2.9 (a) demonstrates the definition of the flow directions. Two images taken from different angles are shown in Figure 2.9 (b) and (c).

#### **2.2.4. Experimental Results**

Figure 2.10 (a) shows the typical sensor spectrum recorded by a spectrum interrogator (sm125, Micron Optics). It is mentionable that, the flow sensor fabricated using metal spherical shell has a similar pattern as the sensor with silicon pillar only. The sensor had a visibility of  $\sim 4$  dB, which was good enough for obtaining the wavelength shift in response to flow. For flow measurements, the high-speed spectrometer (I-MON 512, Ibsen) was used to record the spectrum. Multiple fringe peaks were tracked to find out the peak wavelength shift. According to Equation (3.1) and (3.2), the wavelength difference between the heating laser turned on and off is measured to get rid of the dependence on the medium temperature. To do this, water flow was introduced at

a speed of  $\sim 1.4$  m/s throughout each cycle of measurement, the heating laser was turned on after the flow became stable, the wavelength difference upon heating was recorded. The driving current of 80 mA was used, and the experiment was repeated 10 times for each direction. The average wavelength shift of ten peaks in response to the laser heating was obtained for the water flow from different directions, and the results are shown in Figure 2.10 (b) and Figure 2.10 (c) for the sensor with silicon pillar only and with metal spherical layer, respectively. In all cases, the average value of the peak wavelength shift was considered for the full interval of heating laser on. For the sensor with silicon FPI only, the wavelength was increased by an amount of 1.27 nm (or a temperature rise of 14.94 °C) for the water flow at an angle of 180°, however, the wavelength shift was only 0.54 nm at the incident angle of 90°.

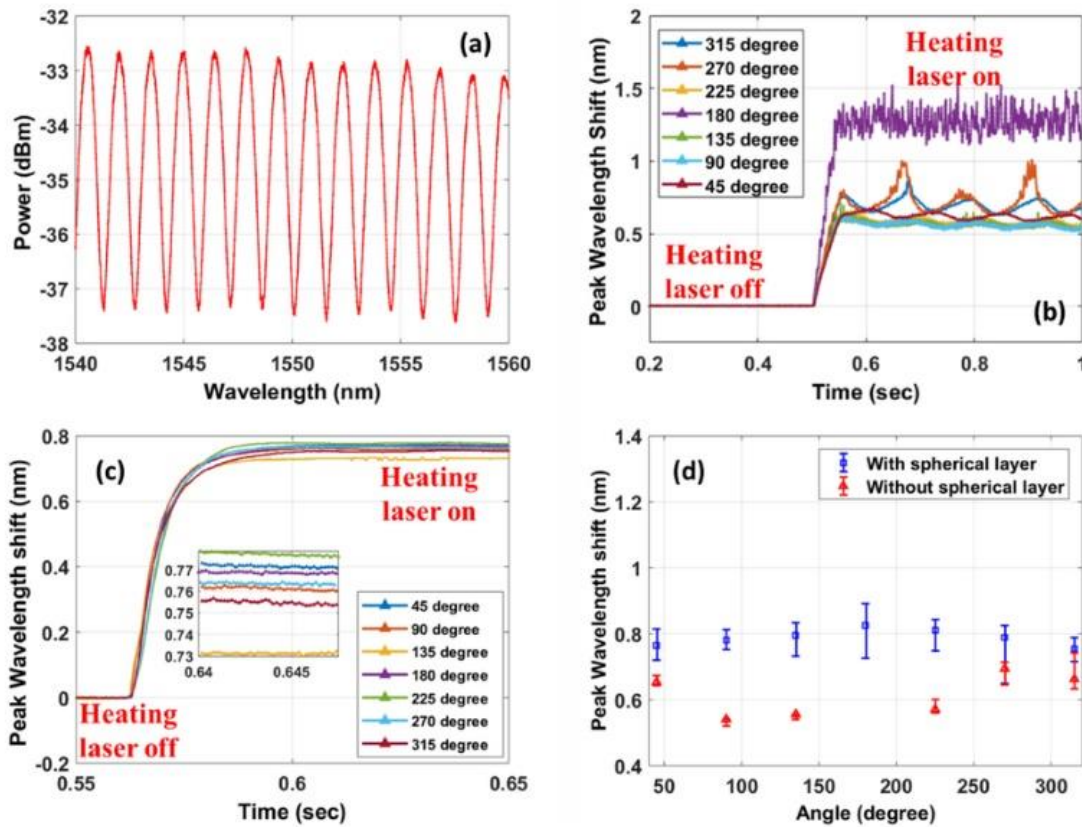


Figure 2.10 A typical reflection spectrum obtained from the fabricated sensor (a), and directional response for the sensor having silicon pillar only (b) and metal spherical layer (c), respectively, which is summarized and compared in (d).

Note that there are a series of spikes in the curve for  $90^\circ$  incidence, which is believed to originate from the vibration during the testing. However, the wavelength difference for different directions was considerably reduced for the sensor with metal shell. The wavelength difference upon heating for both cases is summarized in Figure 2.10 (d). The deviation in response for the sensor with silicon pillar only and with Tin shell has been found 44% and 4% respectively. Directivity has been significantly reduced by using metal sphere with silicon pillar for the flow from different directions.

### **2.2.5. Summary**

Reduced directivity of a fiber-optic water flow sensor based on laser-heated silicon Fabry-Perot cavity was reduced by using a metal spherical layer. Directional heat transfer between the sensor head and water flow was more uniform for the sensor with spherical outer surface than the cylindrical surface. Therefore, the new sensor head delivers a much more uniform response to different flow directions. Experimental results suggest that the variation is reduced from 44% to 4% by adding a tin shell to the original silicon FPI.

### **2.3. Temperature compensation of fiber-optic water flow sensor**

In this section, we report a technique to compensate the effect of water temperature change in the flow measurement by using another sensor which will track the temperature of the water. Flow measurement by the hot-wire fiber-optic water flow sensor based on laser-heated silicon Fabry-Perot interferometer (FPI) need to compensate the temperature variation of the water. This temperature compensation is required to get the flow speed from a unique calibration irrespective of the initial water temperature. Flow measurement is the wavelength change from the baseline wavelength to the final wavelength due to the laser heating of the silicon FPI and cooling by the flow. Temperature variation of the water will also induce wavelength change in the measurement.

This will change the baseline resulting different wavelength shift for different water temperature for a given flow speed. By using the information of the water temperature change, baseline can be defined which will provide unique wavelength change for the flow. Finally, wavelength change corresponding to the flow speed were calibrated using the sensor pair after compensating for the water temperature.

This section contains the contents from [41] which have been reproduced with permission from OSA.

### **2.3.1. Introduction**

Flow velocity is an important parameter for the analysis of oceanic processes including turbulent energy dissipation, sediment transport, air-sea material, and momentum exchange, which can be key in the accuracy of large-scale simulation such as forecasting ocean dynamics and coupled atmospheric events (hurricanes) etc. [28]. They are also sources of deviation in measurements, and at times noise in various ocean sensing applications [42]. Flow velocity measurement was demonstrated by the fiber-optic hot wire water flow sensor fabricated by attaching 200- $\mu\text{m}$ -long, 100- $\mu\text{m}$ -diameter silicon pillar at the end of the cleaved single mode fiber [27]. Flow speed was calibrated with the wavelength position change of the reflection fringes generated from FPI of the silicon pillar. This wavelength change is the transition from the baseline wavelength to the final wavelength resulting from the laser heating of the silicon FPI and cooling by the flow. Baseline wavelength is also dependent on the initial temperature of the water. Baseline wavelength for measuring the flow speed will be different at different ambient temperatures. Measurement of the flow speed needs to be independent of the temperature change of the water, not only to avoid unnecessary calibration steps each time before starting the measurement, but also to decouple dynamic changes often observed in the natural environments such as frontal zones.

Otherwise, the wavelength changes of the spectral notch for a certain flow would be different for water of different temperatures. Therefore, the measurement of flow speed would likely be inaccurate without the compensation of the water temperature. Previously, an optical fiber vector flow sensor based on a silicon array was proposed to measure the flow and direction which was designed by using four silicon FPIs [27]. This sensor was able to partially compensate the effects of water temperature variation on the flow measurement. The vector flow sensor was not able to fully compensate for the temperature change of the water because, the heat generated from the center silicon pillar spread to the other three equally distributed silicon FPIs. To tackle this problem, we fabricated the flow sensor using two sensors fabricated by attaching a silicon FPI (40  $\mu\text{m}$  thickness and 100  $\mu\text{m}$  diameter) to the cleaved end face of a piece of a single-mode fiber (Figure 2.11 (a)). The reason for using the thin silicon pillar was to get a large range of peak wavelength change due to the heating of the silicon pillar. The free spectral range (FSR) of the fabricated sensor is 7 nm which will allow to track 82  $^{\circ}\text{C}$  temperature change following one spectral notch as the sensitivity of the silicon FPI was found 84.6 pm/ $^{\circ}\text{C}$  [3]. Flow measurement information can be found by tracing one of the peak wavelengths for each silicon FPI. One of the sensors will be used to measure the flow of the water using the laser heated silicon FPI (heated sensor) whereas the other sensor will be used to track the temperature of the water without using any laser heating (a cold or “passive” sensor). Temperature change of the water can be compensated for the flow measurement by subtracting the wavelength of the cold sensor from the heated sensor which will be only dependent on the laser power and flow.

In this work, we report on a water flow sensor scheme capable of measuring the flow speed accurately after compensating for the temperature change of the water. Two channels of the coarse wavelength division multiplexer were used for the two sensors. A broadband light source was used

centering at 1550 nm for getting the sensor spectrum. A 980 nm heating laser was used to get the transition for the flow measurement. Finally, the differential wavelength was calibrated for different flow speeds.

### 2.3.2. Principle of operation

The Nth peak wavelength is related with refractive index (RI),  $n$  and length,  $L$  of the FPI by the following equation

$$\left(N + \frac{1}{2}\right) \lambda_N = 2nL \quad (2.22)$$

The peak wavelength of the FPI is related to temperature as shown below [27, 30]

$$\lambda_N(T) = \lambda_N(0) + KT_w + K. \Delta T (\vec{v}, P) \quad (2.23)$$

where  $\lambda_N(0)$  is the initial wavelength and  $K$  is the temperature sensitivity of the silicon FPI,  $T_w$  is the water temperature,  $\Delta T (\vec{v}, P)$  is the temperature rise owing to the combination of heating of the FPI by the heating laser and cooling by the flow. So, the peak wavelength shift is dependent on the temperature rise of the silicon FPI which is related with the flow and heating power. The peak wavelength of the heated sensor is governed by the following equation

$$\lambda_1(T) = \lambda_1(0) + KT_w(t) + K \frac{P}{hA_s} \quad (2.24)$$

where  $h$  and  $A_s$  are the heat transfer coefficient and surface area of the silicon pillar. The peak wavelength of the cold sensor which measures the water temperature given by

$$\lambda_2(T) = \lambda_2(0) + KT_w(t) \quad (2.25)$$

To remove the temperature effect of the water, the flow measurement was deduced from the wavelength difference of the heated sensor and cold sensor. Thus, the flow measurement will

be independent of the water temperature. A typical reflection sensor spectrum is shown in Figure 2.11 (b) from the two FPIs of the sensors collected by the high-speed spectrometer.

$$\Delta\lambda = (\lambda_1(T) - \lambda_2(T)) - (\lambda_1(0) - \lambda_2(0)) = K \frac{P}{hA_s} \quad (2.26)$$

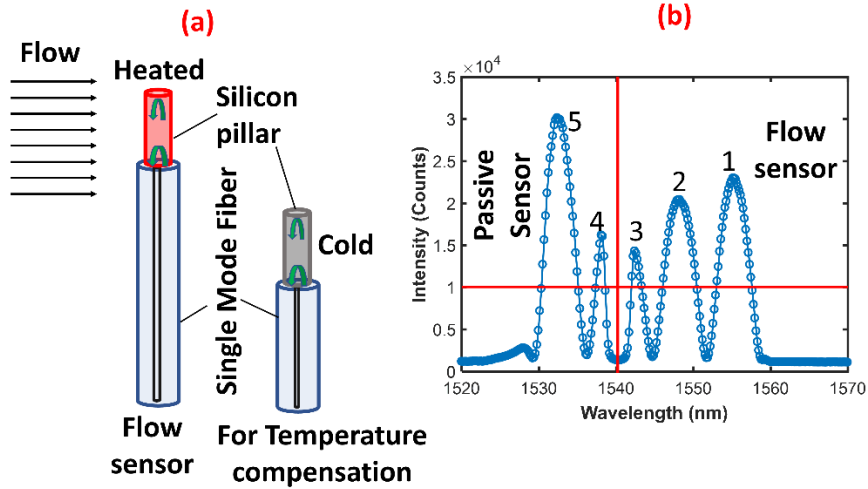


Figure 2.11 (a) Schematic diagram of the sensor and (b) typical sensor spectrum from the two silicon FPIs.

### 2.3.3. Experimental set up

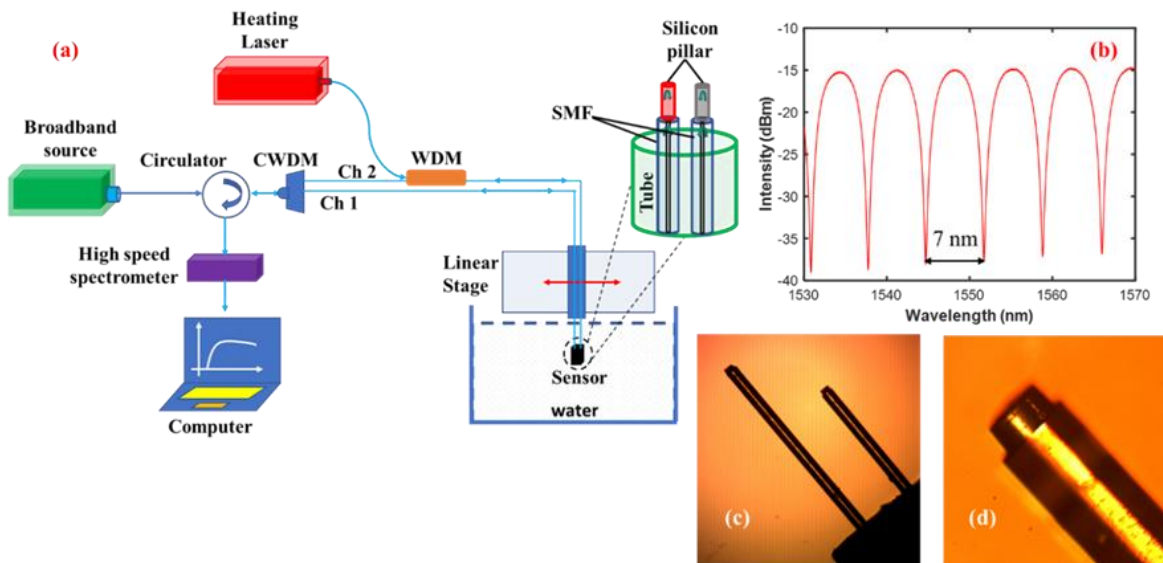


Figure 2.12 Experimental setup for measuring the flow (a), sensor spectrum from in air (b) and microscopic image of the sensor head (c) and (d).

Figure 2.12 (a) shows the experimental set up of the flow measurement using the proposed sensor. FPI was formed by attaching the thin silicon pillar (80  $\mu\text{m}$  diameter and 40  $\mu\text{m}$  thickness) at the end of the cleaved single mode fiber (SMF). Two sensors were attached at the end of a tube (outer diameter  $\sim 2$  mm) to fix them at  $\sim 1$  mm distance sidelong from each other. One end face of the sensor head was slightly more protruded from the other one [Figure 2.12 (c)], to avoid creating any black zone of flow as well as to avoid any heating effect from the heated sensor. A broadband light source centered at 1550 nm was used to illuminate the two FPIs of the flow sensor through a coarse wavelength-division-multiplexer (CWDM), with a channel bandwidth of  $\sim 17$  nm and channel spacing of  $\sim 20$  nm. Light was reflected from the interfaces of the FPI and directed to a spectrometer (I-MON 512 OEM, Ibsen Photonics) via a circulator. A 980 nm diode laser was used via a 980/1550 nm WDM as the heating source and connected to one of the sensors which was connected to the channel 2 (1550-1570 nm channel). The cold and heated sensors were connected to the channel 1 and 2 respectively having a wavelength of 1520 and 1530 nm respectively. A linear stage was used to generate water flow of different speeds. The tube was attached in the linear stage which move along with the linear stage. The sensor head was dipped in the water to have the same background temperature. Figure 2.12 (b) shows the spectrum of the sensor in air measured by optical sensing interrogator (sm125). Microscopic images of the sensor head at lower and higher magnifications are shown in Figure 2.12 (c) and Figure 2.12 (d) respectively.

#### **2.3.4. Experimental results**

The wavelength change with time can be deduced by continuously monitoring the wavelength position of the two FPIs. The wavelength transition due to the laser heating is shown in Figure 2.13 (a) for both channels. Sensors were immersed in still water initially. Then the laser was turned on to get the active heating which provided a wavelength shift corresponding to the

laser power. The laser was then turned on with a driving current of 75 mA which corresponds to an optical power of 10 mW that reached the silicon FPI. Base wavelengths of the cold and heated sensor were 1534.07 nm and 1553.55 nm respectively, which correspond to the initial water temperature. Wavelength positions for both channels were separated due to the center wavelength of the CWDM. When the sensor was heated by turning on the 980 nm pump laser, the heated sensor notch moves 0.71 nm (equivalent to 8.4 °C temperature rise) due to the light absorption (Figure 2.13 (a)). The cold sensor also experienced a wavelength change of 0.04 nm (equivalent to a 0.47 °C temperature rise) due to the heat generated from the heated sensor. This suggests that 1 mm distance between the two sensors is probably not enough to be free from the heat interference. A portion of the heat generated in the cold sensor was carried away when the flow started. There was a flow induced wavelength change of 0.38 nm due to 70 mm/s water flow generated by the moving linear stage. The heated sensor wavelength value was subtracted from the cold sensor wavelength to get the compensation of the temperature variation of the water. This wavelength difference provided a baseline after compensating for the water temperature variation. The baseline would be different without using the cold sensor, which would provide an erroneous flow speed. If the water temperature would be varied after turning on the laser, the cold sensor would compensate this water temperature variation. Finally, the flow speed was deduced from the base wavelength to final wavelength shift due to the heating of the silicon pillar and cooling by the flow. This measurement was taken when the linear stage was stable enough to provide specific flow speed. This process was repeated for the flow of other speeds (10 mm/s, 20 mm/s, 30 mm/s, 40 mm/s, 50 mm/s, 60 mm/s) to calibrate the wavelength difference between the heated and cold sensor with the flow speed of the water.

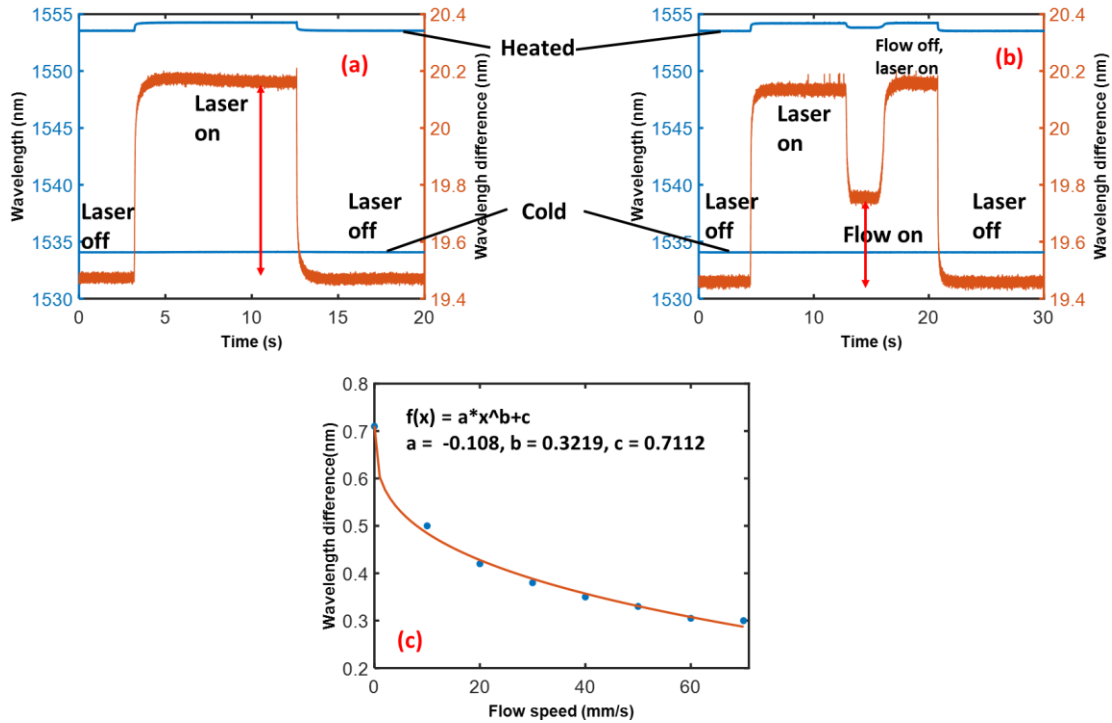


Figure 2.13 Wavelength position of the heated and cold sensor at no flow (a), 70 mm/s (b) and (c) calibration of the flow sensor.

### 2.3.5. Conclusion

In summary, temperature compensation approach of the fiber-optic hot wire flow sensor has been proposed by using two silicon FPIs. Flow speed can be deduced by using the calibration of wavelength change with respect to flow speed for a certain laser power. Accuracy can be further improved by placing the cold sensor at a distance further away where it would not be affected by the heat generated by the heated sensor. Overall, this sensor can be useful to get the flow velocity underwater without having an effect in the flow measurement by the variation of the initial water temperature.

## **Chapter 3: Fiber-optic silicon Fabry-Perot interferometric Bolometer**

### **3.1. Fiber-optic silicon Fabry-Perot interferometric bolometer**

As mentioned in Chapter 1, the fiber-optic silicon Fabry-Perot interferometric temperature sensor has an ideal geometry as a bolometer to measure radiation from plasma fusion devices. Several reports can be found which utilize silicon FPI sensors as a bolometer [43, 44]. The detection limit needed to improve for the bolometer previously reported for its use in plasma profiling. We engineered an absorber layer to modify the previous structure for a higher detection sensitivity. We have demonstrated the design, fabrication, and characterization of the new FOB for plasma radiation measurements.

This section contains figures and excerpts from [45] which have been reproduced with permission from Review of Scientific Instruments.

#### **3.1.1. Introduction**

Bolometers are commonly used for measurements of plasma radiation in tokamaks, stellarators, and other magnetic-confinement fusion devices [46]. Different types of bolometers, such as pyroelectric bolometers [47], resistive bolometers [48-50], capacitive bolometers [51], IR imaging bolometers [52], thermistor bolometers [53], semiconductor bolometer [54] have been studied for the application. Low noise-equivalent power density (NEPD) is usually preferred because it enables high spatial resolution when the bolometers are used in pinhole or collimator cameras. A fundamental challenge in achieving low NEPD is to overcome the large electromagnetic interference (EMI) present in magnetic-confinement fusion devices that can induce significant noise to the bolometer system. A fiber-optic bolometer (FOB) is an attractive alternative technology owing to its inherent advantages of immunity to EMI of the sensor head and the capability to remotely interrogate the sensors. FOBs have additional advantages of small

size, light weight, and potential high-temperature capability. Recently, we started the first attempts at exploring a fiber-tipped temperature sensor for plasma bolometer applications [43]. The sensor is made by attaching a small silicon pillar of about 200  $\mu\text{m}$  thickness and 80  $\mu\text{m}$  diameter to the free end of a single-mode fiber (SMF) using a vacuum compatible adhesive. The silicon pillar functions as a low-finesse Fabry-Perot interferometer (FPI) whose reflection spectrum is measured by a broadband source along with a high-speed spectrometer. Temperature variations are deduced by the shift of the spectral fringes of the FPI caused by the thermo-optic effect of the silicon material. The silicon pillar also functions as the absorber for bolometer applications. The initial FOB has a relatively large NEPD of 5-10  $\text{W}/\text{m}^2$  with a time constant of  $\sim 100$ -200 ms tested using a 405 nm laser [43]. A later design was able to reduce the NEPD significantly to 0.27  $\text{W}/\text{m}^2$  with a time constant of  $\sim 400$  ms tested at the same wavelength of 405 nm [44]. The NEPD improvement was achieved through two mechanisms. The first is to improve the temperature measurement resolution using a high-finesse design of the FPI where the silicon pillar was coated with a dielectric mirror on one side and a thin (100 nm) gold mirror on the other side. In addition, a short section of graded-index multi-mode fiber was sandwiched between the silicon pillar and the SMF as a collimator to reduce the diffraction of the light from the SMF. The second is to increase the responsivity of the FOB by reducing the thickness of the silicon pillar so that the thermal mass per unit cross-sectional area is decreased. It is estimated that reducing the thickness of the silicon pillar from 200  $\mu\text{m}$  in the initial design to 75  $\mu\text{m}$  in the later design resulted in a  $\sim 3$  times increase in the responsivity at the test wavelength of 405 nm. However, reducing the thickness of the silicon pillar would not be as effective in practical plasma applications where radiation over a broad frequency range from soft x-ray to near infrared needs to be measured. Due to the relatively low stopping power of silicon to high energy photons (e.g., silicon has an attenuation length of  $\sim 70$   $\mu\text{m}$  at photon

energy of 10 keV), reducing the thickness of the pillar will also reduce the absorption of the radiation.

In this work, we report the design, fabrication, and characterization of an FOB with improved NEPD performance and increased absorption to high-energy photons by engineering the absorber of the FOB. Specifically, attaching a relatively thick and large gold disk at the end of a small high-finesse silicon FPI a bolometer leads to a significant increase of the FOB responsivity. The high stopping power of gold also renders more effective absorption of high-energy photons. We developed a fabrication process for the FOB of the new design and compared its NEPD with the design where the gold disk has the same diameter as the silicon pillar. We show that the FOB of the new design has a much smaller NEPD (0.13 vs. 0.77 W/m<sup>2</sup>) tested using a laser at 405 nm. FOB with gold disk has a NEPD of 0.13 W/m<sup>2</sup> which is even smaller than the FOB with a shorter silicon and larger time constant (0.27 W/m<sup>2</sup>) [44].

### **3.1.2. Principle of operation**

It is useful to briefly explain the principle of operation using an FOB with a structure shown in Figure 3.1 (a). The light from a SMF is expanded and collimated using a collimator made from a short section of graded-index multimode fiber before illuminating a silicon FPI, which is made by coating the near side of silicon pillar with an ultrathin (~25 nm) gold mirror and the far side with a gold layer that has the same diameter as the silicon pillar. Both the gold coatings and the silicon pillar function as the FOB absorber. The reflection spectrum of the FOB has several narrow notches at the resonant wavelengths of the silicon FPI, as shown in Figure 3.1 (b). The plasma radiation increases the temperature of the silicon FPI, resulting in a red shift of the spectral notches that can be measured by a broadband light source or a wavelength-scanning laser. This structure is similar to the FOB we reported in Ref. [44].

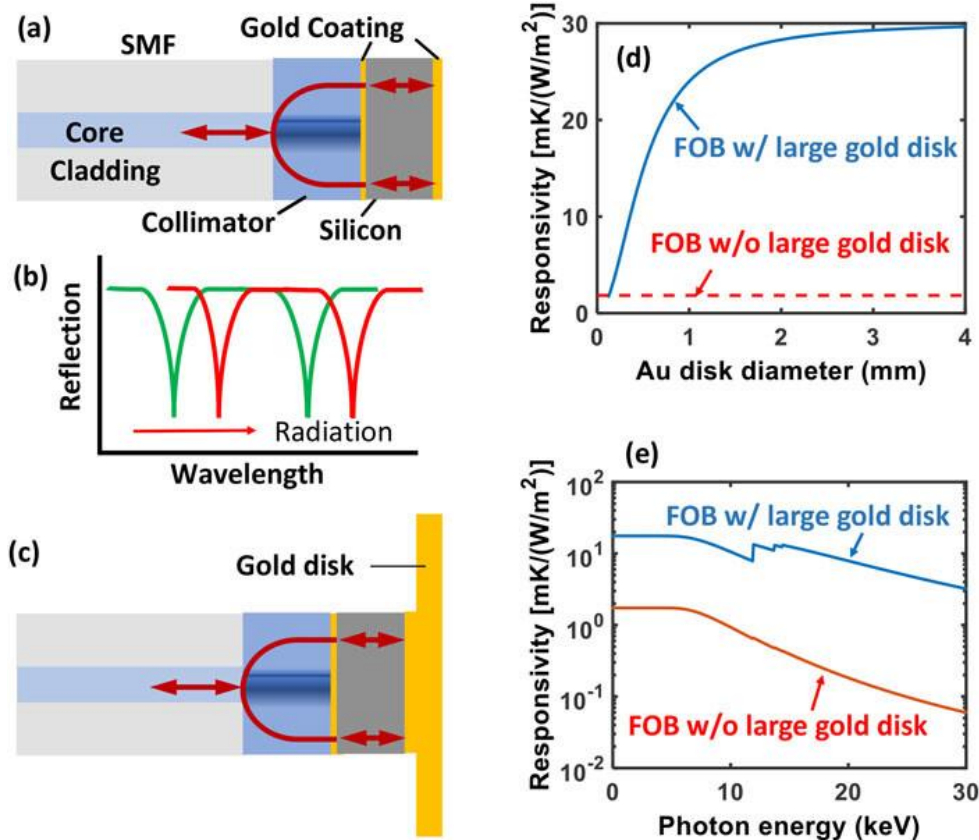


Figure 3.1 Schematic of the (a) FOB head with a gold disk flush with the silicon pillar (old design), (b) resonant wavelength shift in response to radiation absorption, (c) FOB head with a large gold disk (new design), (d) responsivity, defined as the temperature change to an incident power flux of  $1 \text{ W/m}^2$  (assuming 100% absorption) as a function of the Au disk diameter for the FOB of new design with a  $100\text{-}\mu\text{m}$ -thick,  $125\text{-}\mu\text{m}$ -diameter silicon pillar and a  $4\text{-}\mu\text{m}$ -thick gold disk (for comparison, responsibility for the FOB without the gold disk is also shown), and (e) responsivity as a function of photon energy considering the attenuation length of the materials for the two FOBs.

Gold has much larger x-ray stopping power than silicon. For example, a  $4 \mu\text{m}$  thick gold layer results in 80% absorption of radiation for photons at 8 keV, while a  $112 \mu\text{m}$  thick silicon is needed to achieve the same amount of absorption. Compared with a silicon pillar, a gold film with the same radiation absorption will show a much higher temperature rise from a given power density even though gold has a slightly larger volumetric heat capacity ( $2.49$  vs.  $1.63 \text{ J}/(\text{cm}^3 \cdot \text{K})$ ). Using this fact, we propose a modified structure of FOB, shown schematically in Figure 3.1 (c), that can provide a significant increase of the responsivity. In this structure, the surface area of the gold absorber is made much larger than the cross section of the silicon pillar so that the response of the

FOB is dominated by the gold layer that shows higher sensitivity to radiation. It is worth noting that this improvement is applicable to the low-finesse fiber-optic bolometer design as well. To estimate the improvement in sensitivity of this modified structure, we assume a lumped thermal mass where the temperature distribution in the gold disk and the silicon pillar is uniform. We consider a power density,  $q$  deposited on the front surface of gold absorber. The resulting temperature rise due to the absorption of photons in the gold disk under steady state,  $\Delta T$ , is given by

$$\Delta T = \frac{q S_{Au} \tau}{C_{v,Au} S_{Au} d_{Au} + C_{v,Si} S_{Si} d_{Si}} \quad (3.1)$$

where  $\tau$  is the time constant,  $C_{v,Au}$  ( $C_{v,Si}$ ),  $S_{Au}$  ( $S_{Si}$ ) and  $d_{Au}$  ( $d_{Si}$ ) are, respectively, the volumetric heat capacity, cross-sectional area, and the thickness of the gold coating (silicon pillar). For  $\tau = 300$  ms, and the silicon pillar with a diameter of  $125 \mu\text{m}$  and a thickness of  $100 \mu\text{m}$ , and for the gold layer thickness of  $4 \mu\text{m}$ , Figure 3.1 (d) shows the FOB responsivity ( $\Delta T/q$ ) as a function of the diameter of the gold absorber. It is seen that the responsivity monotonically increases with the diameter of the gold disk and the responsivity enhancement seems to follow an exponential function where the effect of the gold diameter is more prominent initially and gradually tapers off as the diameter increases, eventually approaching its maximum value, which is determined by the thermal properties and the thickness of the gold layer. A moderately enlarged disk diameter can provide a significant improvement. For example, from Figure 3.1 (d), the responsivity for a  $0.6$  mm diameter gold disk is  $\sim 18 \text{ mK}/(\text{W}/\text{m}^2)$ . For comparison, the detection sensitivity for the case where there is only a thin ( $100 \text{ nm}$ ) gold mirror with the same diameter as the silicon pillar is  $\sim 1.8 \text{ mK}/(\text{W}/\text{m}^2)$ . It is seen that by using an enlarged gold disk with a diameter  $0.6$  mm, the sensitivity can be improved by approximately 10 times due to the increase in radiation absorption. It is worth noting that the maximum diameter of the gold disk that can be used in practice may be

limited by other factors such as the mechanical integrity of the structure and the fabrication challenges. In addition, the size of the gold disk will ultimately determine the spatial resolution of the FOB. These factors need to be considered in determining the diameter of the gold disk in practice. Note that we have assumed that the radiation is absorbed completely by the sensors in Figure 3.1 (d). Such assumption is only valid for low-energy photons. Figure 3.1 (e) shows the calculated responsivity of the FOB of the two designs as a function of the photon energy using the data for the attenuation length of silicon and gold from literature[55]. In Figure 3.1 (e), the gold disk of the FOB has a diameter of 0.6 mm and other parameters are identical to those used for Figure 3.1 (d). Due to the large stopping power of gold, the FOB with the large gold disk shows further improved responsivity at high photo energy levels. Despite this improvement, the responsivity for the FOB with the 4  $\mu\text{m}$  thick, 0.6 mm diameter gold disk drops to 80% when the photon energy increases to 8.1 keV. A thicker gold disk can be used to enhance the absorption for high energy photons. However, using a thicker gold disk also results in a larger thermal mass of the sensor. Therefore, an optimized gold disk thickness may exist for a given radiation spectrum. The maximum disk thickness that can be obtained in practice may also be limited by the same factors that limit the disk diameters such as mechanical integrity of the sensor structure and fabrication challenges. This analysis assumes that the heat transfer, e.g., the time constant, is essentially the same and that energy absorbed by the larger diameter Au disk is conducted into the Si pillar. For test results done in air, the increased surface area of the gold disc could potentially allow heat to be removed prior to it raising the temperature of the pillar, and thus not measurable by our interferometric approach. But the application for a plasma bolometer would place the sensor in vacuum, removing the air conduction as a thermal sink.

### 3.1.3. Design and fabrication of the FOB

We developed a fabrication method for the proposed FOB structure shown in Figure 3.1 (c). In this method, the gold disks with enlarged diameters and the fiber-tipped high-finesse silicon FPI are separately prepared and subsequently glued together using UV epoxy.

#### 3.1.3.1. Gold disk preparation

Figure 3.2 schematically shows the fabrication process of the gold disks used as the absorber of the FOB. A 380 $\mu\text{m}$  thick, 3-inch diameter silicon wafer, used as the substrate, was cleaned in an ultrasonic bath filled with isopropanol for 30 minutes. Then it was dried using nitrogen blow prior to deposition. The silicon wafer was annealed before subsequently depositing a 100 nm thick adhesion layer of titanium (Ti) and a 300-nm thick copper (Cu) layer (Figure 3.2 (a)) using the RF sputtering [56]. The Cu layer was used as a conductor for electroplating of the gold layer in the following step and it also serves as a sacrificial layer that will be eventually removed to free the gold disks for FOB fabrication. The Ti layer was used because of its good adhesion to both the silicon wafer and the Cu layer [57]. Next, gold electroplating was used for growing thick gold layer of  $\sim 4\ \mu\text{m}$  on the top of the Cu layer (Figure 3.2 (b)). Gold electroplating was selected because of its low cost and fast deposition rate. Total duration of the electroplating for the 4  $\mu\text{m}$  thick gold coating was around 4 hours. Then, a thin layer of positive photoresist (AZ 4620) was deposited on the top of the gold layer using spin coating at a speed of 2000 rpm (Figure 3.2 (c)). The photoresist layer was patterned by exposing it to UV light through a mask having different circular apertures of diameter varying from 300  $\mu\text{m}$  to 700  $\mu\text{m}$  after the application of thermal heating; and afterwards, UV light exposed photoresist was removed by using developer (Figure 3.2 (d)). Next, a gold etchant was used to remove the unprotected gold which was not covered by the photoresist to obtain the gold disks (Figure 3.2 (e)). The photoresist on top of the

gold disks was removed by rinsing the wafer in acetone, leaving arrays of gold disks sitting on the Cu layer (Figure 3.2 (f)). Finally, copper etchant was applied to remove the sacrificial Cu layer, freeing the gold disk from the silicon wafer (Figure 3.2 (g)). Finally, the gold disks were collected from the Cu etchant and further cleaned in DI water for use in FOB fabrication (Figure 3.2 (h)).

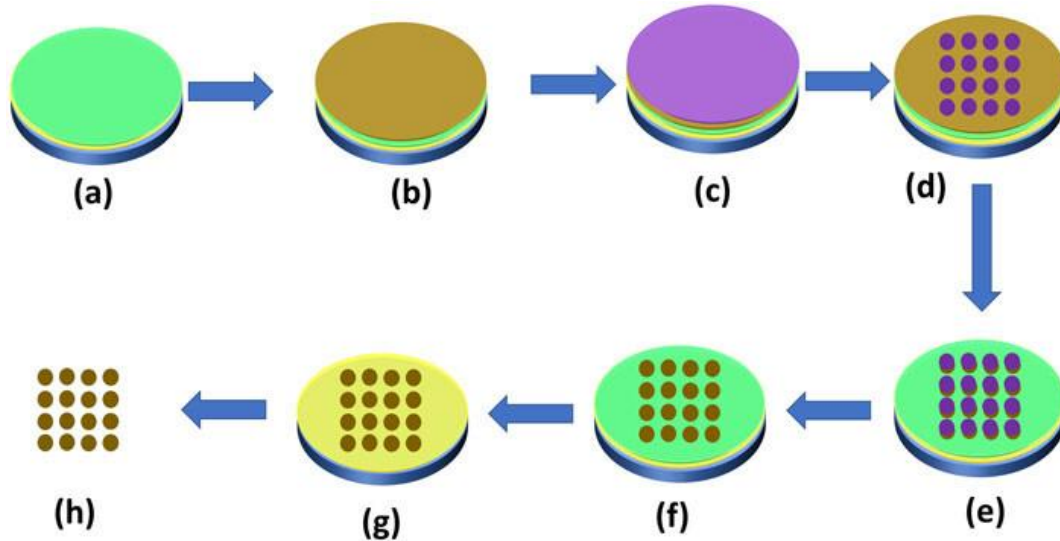


Figure 3.2 Schematic diagram of the fabrication process of the gold disk: (a) silicon wafer deposited with Ti and Cu; (b) silicon wafer deposited with Ti, Cu, and Au; (c) spin-coated photoresist layer on the top of Au layer; (d) the photoresist patterned layer by lithography; (e) Au etching; (f) deposited photoresist removed; (g) Cu etching; and (h) gold disk.

Figure 3.3 (a) shows the image of the gold disks attached in the silicon wafer after removing the UV light exposed photoresist (Figure 3.2 (e)). SEM image of the top view and side view of one of the fabricated gold disks are shown in Figure 3.3 (b) and Figure 3.3 (c), respectively, which show that the diameter and thickness of this gold disk were  $600\ \mu\text{m}$  and  $4\ \mu\text{m}$  respectively. The elemental composition of the fabricated gold disk was studied using energy-dispersive x-ray spectroscopy (EDS) and the EDS spectrum is shown in Figure 3.3 (d), indicating that the majority content was gold along with a small number of other impurities, which are not expected to cause significant negative effects on the FOB performance.

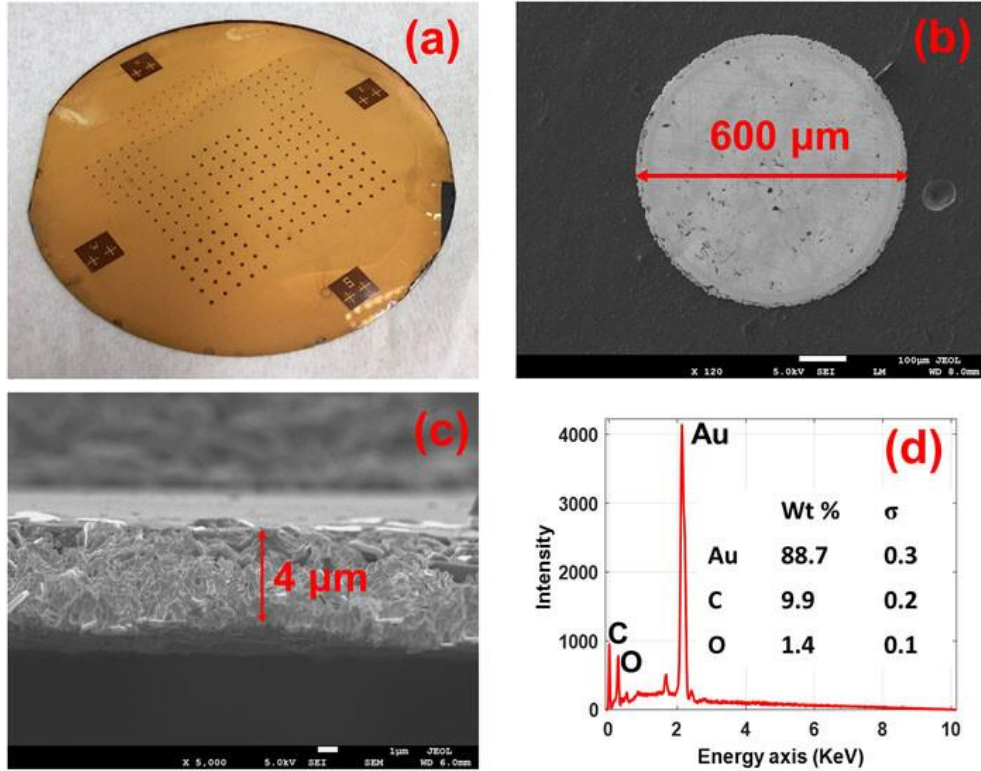


Figure 3.3 (a) Image of the gold disk on silicon wafer. (b) SEM image of the gold disk separated from the wafer (top view), (c) side view, and (d) EDS spectrum of the gold disk.

### 3.1.3.2. FOB fabrication

Silicon pillars were prepared using standard silicon micromachining technique involving patterning a 100 nm thick double-side polished silicon wafer using photoresist followed by deep-reactive ion etching and cleaning. The process generated arrays of silicon pillars with a diameter of 200  $\mu\text{m}$  connected to the main silicon frame through two narrow scaffolds, as shown in Figure 3.4 (a). Then, using ion beam sputtering, one side of the pillars along with the wafer frame was coated with a  $\sim 100$  nm gold layer resulting in 98% reflectivity at 1550 nm and the other side with  $\sim 25$  nm thick gold, which has a reflectivity of  $\sim 92\%$  and transmissivity of 5% at the same wavelength. The rest of the processes are similar to those reported in Ref [44]. Briefly, a span of graded-index multimode fiber was spliced to the lead-in single-mode fiber using an optical fiber splicer and then was cleaved under a microscope to leave a short stub about 250  $\mu\text{m}$  connected to

the lead-in single mode fiber functioning as a collimator. Then, a small amount of UV glue was transferred to the end of the fiber and the fiber is aligned with one of the silicon pillars on the wafer guided by a white-light system that monitored the reflection spectrum of the silicon pillar in real time. After alignment, the glue was cured to bond the fiber with the pillar on the side with the  $\sim 25$  nm gold coating. Next, the fiber was pushed down to break the scaffolds through which the pillar was connected to the wafer, resulting in an FOB like the previous design that does not have a large, thick gold disk, as shown in Figure 3.1 (a). Figure 3.4 (g) is a microscopic image of such a bolometer and Figure 3.4 (h) is the reflection spectrum measured by an optical sensing interrogator (Micron Optics, Model: sm125). The spectrum shows a free-spectral range (FSR) of  $\sim 3.0$  nm for the silicon FPI, consistent with the thickness ( $100 \mu\text{m}$ ) of the silicon pillar, a fringe visibility of 4 dB, and a full-width at half-width (FWHM) of 0.34 nm for the spectral notches, corresponding to a finesse of 8.8 for the FPI. Finally, one of the fabricated gold disks (diameter  $600 \mu\text{m}$  and thickness  $\sim 4 \mu\text{m}$ ) was attached to the silicon pillar on the side with 100 nm gold coating using UV glue to complete the fabrication. The UV glue (Model: EPO-TEK OG142-87, Epoxy Technology) has a suggested maximum (intermittent) operating temperature of  $300^\circ\text{C}$ . Figure 3.4 (i) is an image of the FOB with the large gold disk clearly visible. Figure 3.4(j) is the reflection spectrum, which shows a similar FSR (3.0 nm), slightly larger fringe visibility (6 dB) and narrower FWHM (0.29 nm) compared with from the FOB of the previous design without the large gold disk. The differences in fringe visibility and FWHM are attributed to the variations from fabrication process.

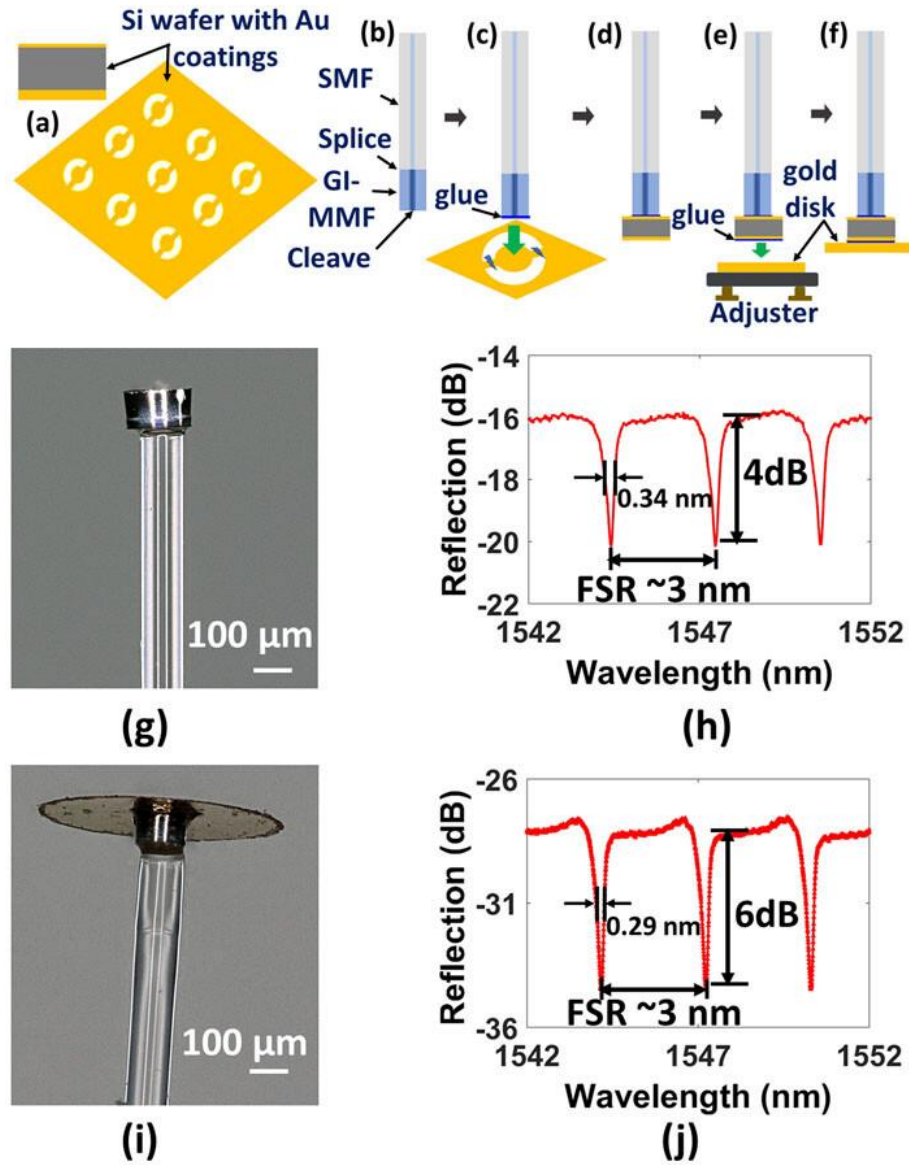


Figure 3.4 (a)–(f) Schematics of the fabrication steps for the FOB without and with a large gold disk; microscope images of the FOBs of the previous design (g) and the new design (i); reflection spectra of the FOBs of the previous design (h) and the new design (j).

### 3.1.4. FOB characterization

FOB was demonstrated using the experimental set up shown in Figure 3.5. A narrow linewidth distributed feedback (DFB) diode laser at 1550 nm was used for demodulation. The laser wavelength was scanned by modulating the injection current with a triangle wave with a frequency of 2 kHz that resulted in a wavelength scanning range of 623 pm. The light from the DFB laser

was split into two paths using a 33/67 coupler, with 67% fed to the new the FOB with the large gold disk and 33% fed to the one without the large gold disk. Using the optical absorption of gold coatings to the laser light, we included attenuators in the system to tune the optical power in each path and consequently the temperature of the silicon FPI, providing a small tuning capability of the spectral notch positions for both FOBs so that they were close enough and could be scanned by the DFB laser at the same time. In each path, a fiber-optic circulator was used to direct the reflected light from the FOB to a photodetector (PD). The signal from the PD was recorded using a data acquisition (DAQ) system with a sampling rate of 2 MHz. The data points around the center of the spectral notch were fitted using a third order polynomial function to find the wavelength position of the spectral notch and the wavelength shift of the notch was converted to temperature variations using the temperature sensitivity of 84.5 pm/K [3]. Another fiber-pigtailed DFB laser at 405 nm was used as the radiation source for testing. Each of the FOB was separately tested. The two FOBs were placed horizontally and side-by-side with a lateral distance about 5 mm between the FOB heads. A pair of apertures were placed in front of an FOB to ensure that the radiation only fell onto that FOB for testing.

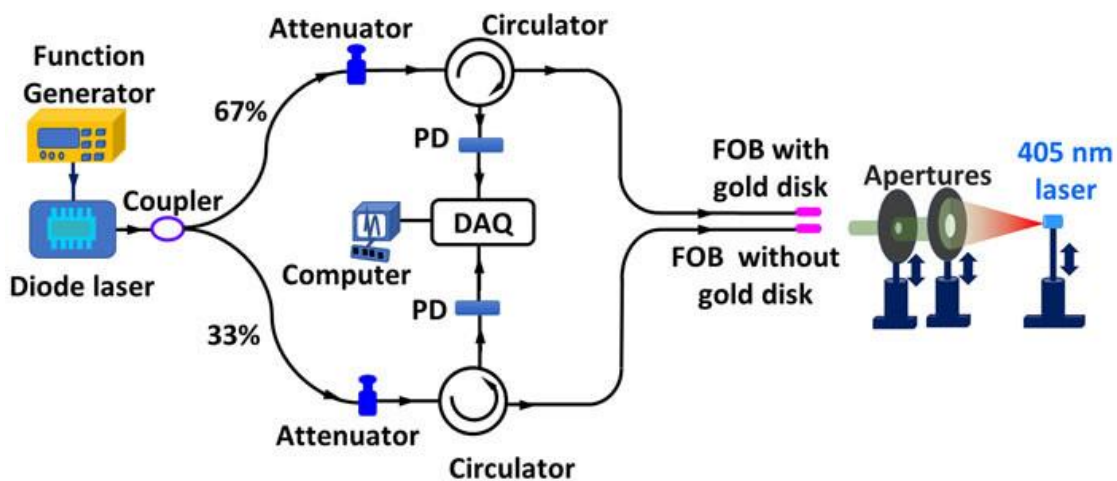


Figure 3.5 Experimental setup to characterize the noise and responsivity of the FOB.

### 3.1.5. Results

First, we characterized the noise of the two FOBs. For this purpose, the 405 nm test laser was not used, and data were continuously recorded using DAQ for around 60 seconds simultaneously for both FOBs when they were in ambient environment. The results were then translated to relative temperature variations as shown in Figure 3.6 (a). To obtain the noise of the FOB without the large gold disk, common noises from the ambient temperature variations and the laser wavelength drifts were first removed. Because these noises were expected to vary slowly, a moving average of 10 consecutive data points were used for the results from the FOB of the new design to obtain the slow drift from these common noise sources. Then the time-averaged signal was subtracted from the results of the FOB without a large gold disk (Figure 3.6 (b)). It is seen that the common noise was reduced significantly. However, a small residual drift that is mostly linear over the testing period persisted. The exact sources of the drift are still under investigation. The initial tests show that at least two sources potentially contributed to the observed residual drift. One is the intensity drift of the 1550 nm laser source for sensor interrogation. The absorption of the gold mirrors can increase the temperature of the FOBs. The other is the movement of the air around the two FOBs that can slightly change the efficiency of heat transfer from the FOBs to the air and, consequently, the temperature of the FOBs. In both cases, the changes may not be identical so they may not be completely removed. The drift was obtained by the linear fitting of the data (green line in Figure 3.6 (b)) and was subtracted from the data. The standard deviation of the relative temperature change after the linear drift is removed is 0.12 mK, which was used as characterization of the noise of the FOB without the large gold disk. Similar processes were performed to obtain the noise of the FOB of the new design. Figure 3.6 (c) shows the results after the common noise was removed and its linear fitting also indicates it had a persisting residual

linear drift. After the linear drift was removed, a standard deviation of 0.16 mK is obtained for the FOB of the new design.

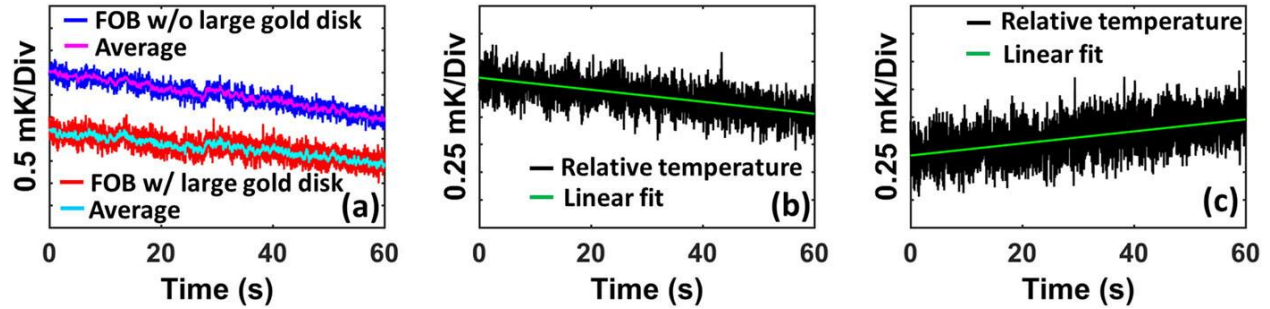


Figure 3.6 (a) Original data captured using DAQ for the two bolometers without any radiation; relative temperature variation of the (b) FOB without a large gold disk, and (c) FOB with a large gold disk in the absence of radiation laser.

To characterize the responsivity of each of FOBs, the FOB was exposed to the 405 nm laser modified by 0.1 Hz square waves with the maximum power at different levels. The time history change of the two FOBs in response to radiation with a maximum power density level of  $\sim 37 \text{ W/m}^2$  and  $\sim 57 \text{ W/m}^2$  are shown in Figure 3.7 (a) and (c), respectively, for the FOB of the previous design, and in Figure 3.7 (b) and (d), respectively, for the FOB of the new design. Temperature rise of 11 mK and 19 mK occurred for the FOB without a large gold disk for an incident radiation power density of  $\sim 37 \text{ W/m}^2$  and  $\sim 57 \text{ W/m}^2$ , respectively, corresponding to a responsivity of  $\sim 0.3 \text{ mK}/(\text{W/m}^2)$ , whereas for the new FOB with a large gold disk, the temperature rises were 100 mK and 167 mK, respectively, for the same power density levels, corresponding to a responsivity of  $\sim 2.8 \text{ mK}/(\text{W/m}^2)$ . The FOB with the large gold disk shows more than 9-fold increase in the responsivity.

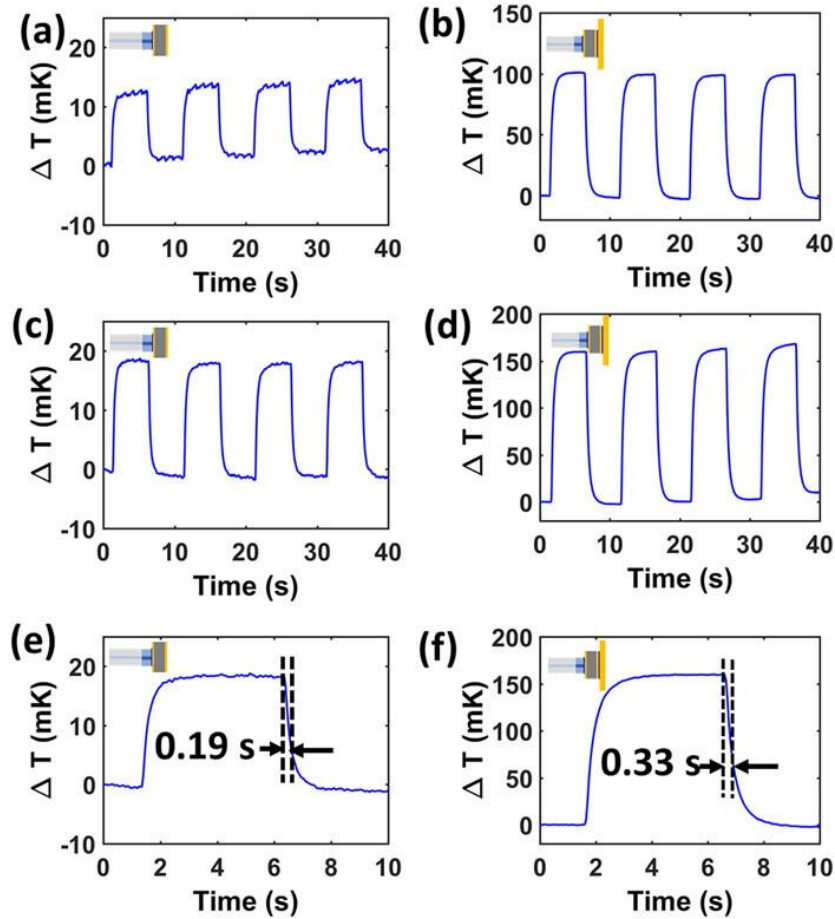


Figure 3.7 Time history of the temperature change in the FOB without a large gold disk [(a) and (c)] and the FOB with a large gold disk [(b) and (d)], exposed to a 0.1 Hz square wave power flux at  $\sim 37 \text{ W/m}^2$  and  $\sim 57 \text{ W/m}^2$ , respectively. Close-up view of a response circle of the FOB without a large gold disk (e) and the new FOB with a large gold disk (f).

Next, we characterized the time constant of the FOBs, which is obtained from the falling signal of the FOB response of a single cycle and corresponds to the time required to have 63% of the overall change. As shown in Figure 3.7 (e) and (f), response time for the FOB without a large gold disk is 190 ms, whereas it is 330 ms for the new FOB with a large gold disk. The test was performed in still air in the lab environment where the heat of the FOB can be transferred to the air through convection, to the silica fiber base through conduction, and to the surrounding environment through radiation. The time constant is determined by all these thermal paths; however, among these three heat-transfer mechanisms, the natural convective heat transfer

between the FOB head and the air is dominant. The silica fiber has a small size and a relatively low thermal conduction coefficient. The radiation from the test laser and the laser for sensor interrogation only raise the temperature of the FOB head slightly above the surrounding environment. The natural convection heat transfer coefficient is strongly affected by the geometry, size, and orientation of the associated solid surface. Although the FOB with the large disk has a much larger surface area compared with the one without the disk, the large gold disk has a much smaller heat transfer coefficient, leading to an increase in the time constant of the FOB. In practical applications, the FOB would be placed in a vacuum environment where natural convection is removed. In this case, a much longer time constant is expected for the FOB. To reduce the time constant, a heat sink should be added to the FOB structure to dissipate the heat more quickly from the FOB.

Finally, we characterized the NEPD by measuring the signal-to noise-ratio (SNR) at different power density levels for both FOBs. SNR is calculated from the temperature rise ( $\Delta T$ ) due to radiation divided by  $\sqrt{2}\sigma_T$ , where  $\sigma_T$  is the standard deviation of the noise for the corresponding bolometer. Figure 3.8 shows measured SNR vs. power density and its linear fitting for both FOBs. NEPD is the power density corresponding to unity SNR which is found from the linear fitting of the experimental data. respectively. The NEPD for the FOB without the gold disk was  $0.77 \text{ W/m}^2$ , whereas the FOB with the gold disk shows an NEPD of  $0.13 \text{ W/m}^2$ , which is six times smaller. For comparison, the FOB reported in Ref. [44] that uses a  $75 \text{ }\mu\text{m}$  thick silicon pillar as both the FPI for temperature measurement and the absorber. It shows a noise level of  $0.12 \text{ mK}$ , a responsivity of  $0.74 \text{ mK}/(\text{W/m}^2)$ , a time constant of  $400\text{ms}$ , and an NEPD of  $0.27 \text{ W/m}^2$ . The new FOB reported here has much stronger absorption to high-energy photons, a similar noise level ( $0.16 \text{ mK}$ ), a three-times increase in responsivity ( $\sim 2.8 \text{ mK}/(\text{W/m}^2)$ ), a shorter time constant

(330 ms), and a two-fold decrease in the NEPD ( $0.13 \text{ W/m}^2$ ). Moreover, the new FOB is expected to have a stronger stopping power to the radiations in the soft x-ray due to the use of the  $4 \mu\text{m}$  thick gold layer as the main absorber.

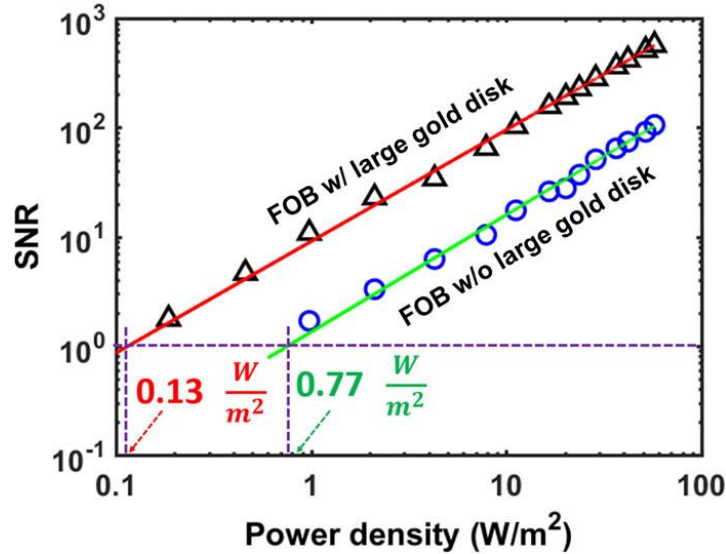


Figure 3.8 Measured SNR vs power density for the bolometer without and with a large gold disk.

### 3.1.6. Summary

We have reported the design, fabrication, and characterization of an FOB with improved detection sensitivity intended for plasma diagnosis in magnetic confinement thermal fusion devices. The FOB is based on a silicon high finesse FPI with the gold absorber made much larger than the cross section of the silicon FPI. A fabrication method was developed for FOBs with such structures. Experiments were performed to characterize the noise, responsivity, response time, and NEPD for an FOB with a  $4 \mu\text{m}$  thick,  $0.6 \text{ mm}$  diameter gold disk attached to a  $200 \mu\text{m}$  diameter,  $100 \mu\text{m}$  thick silicon FPI and compared it with the previous design that does not have the large gold disk and whose absorber is mainly the silicon FPI itself. The results show that the FOB proposed in this work has higher responsivity (approximately nine times higher) and improved NEPD (approximately six times smaller) tested using a  $405 \text{ nm}$  laser. In addition, the thick gold

disk can improve the absorption of the FOB for high-energy photons and the use of ultra-thin gold coating (rather than dielectric coating) on the front side of the silicon FPI as the partial mirror reduces the cost associated with the fabrication of the FOB.

### **3.2. Multichannel fiber-optic silicon Fabry-Perot interferometric bolometer**

In this section, we present a study on the use of FOB to the multichannel system intended to reduce the cost per channel and higher measurement range. FOB used in this multichannel bolometry system was fabricated by using the silicon pillar and gold disk. We have developed a multichannel fiber-optic bolometry system with five bolometers connected to each channel of the coarse wavelength division multiplexer (CWDM), a single light source of super luminescent LED (SLED) and a single I-MON 512 OEM spectrometer. Bolometers with simple structure and a robust multichannel bolometry system can measure radiation with the same NEPD and higher responsivity compared to the scanning laser-based bolometry system which reduces the cost per channel and sensor fabrication complexity.

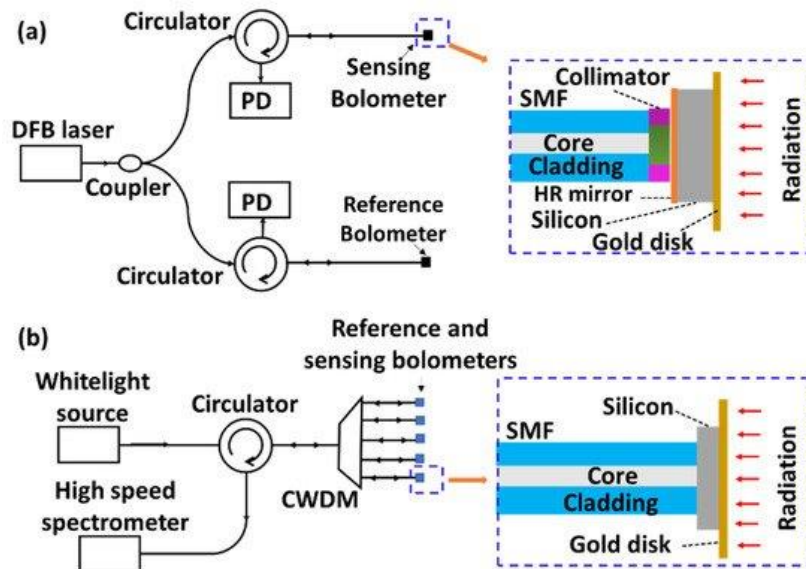
This section contains figures and excerpts from [58] which have been reproduced with permission from MDPI.

#### **3.2.1. Introduction**

Obtaining the temporal and spatial profiles of plasma radiation is important for analyzing plasma behaviors quantitatively in the fusion system. Due to the broad range of the plasma radiation spectrum that spans from soft x-ray to near infrared, bolometers that consist of an absorber and a thermometer are typically used for measuring the radiation of plasma in different types of fusion devices [59-62]. Various bolometers for thermal fusion applications have been developed in the past, including resistive bolometers, infrared imaging video bolometers, absolute extreme ultraviolet diode bolometers, fiber-optic bolometers, and ferro-electric bolometers [63].

Among them, fiber-optic bolometers have the unique advantage of immunity to electromagnetic interference that makes them particularly attractive for measuring radiation in magnetically confined fusion [63]. In addition, they have a small size and can potentially operate in an environment with elevated temperatures. Previously, we demonstrated fiber-optic bolometers based on high-finesse silicon Fabry–Perot (FP) interferometers (FPIs) that show promising noise performance [44]. The most recent system features a noise-equivalent power density (NEPD) of  $\sim 0.13 \text{ W/m}^2$  and a time constant of 330 ms tested at around normal temperature and pressure [45]. As shown in Figure 3.9(a), such a system typically employs two bolometers: one as the sensing bolometer for the radiation measurement and the other as the reference bolometer for removing the drift from environmental perturbations and laser wavelength drift. The bolometers have rather complicated structures, and precise optical alignment in fabrication is needed to achieve high finesse and good visibility of the FP fringes. The structure of the bolometer is shown schematically in the inset of Figure 3.9 (a). One side of the silicon pillar is coated with a high-reflection dielectric multi-layer thin-film coating or an ultrathin gold layer, and the other side is attached to a gold disk that functions as both a high-reflection mirror and an absorber. A collimator made by a short section of graded-index multimode fiber of appropriate length [64, 65] is sandwiched between a single-mode fiber (SMF) and the dielectric mirror to expand the light beam from the SMF and combat the diffraction loss of light from the SMF. Temperature rise of the FPI from radiation can be measured by measuring the spectral shift of the FP fringes. The high-finesse design of the FPI results in narrow reflection spectral notches that typically cannot be resolved by a spectrometer in a white-light system. Both the sensing and the reference bolometers are interrogated by a distributed feedback (DFB) laser whose wavelength is scanned through current-injection wavelength modulation along with a photodetector. As wavelength scanning of the DFB laser is

limited to a small range ( $\sim 1.0$  nm) that is smaller than the free spectral ranges (FSRs) of the FP cavities of the bolometers, precise control of the FP cavity length is needed to ensure that the reflection spectral notches of both bolometers (sensing and reference) are within the scanning range of the DFB laser. The complicated bolometer structure and the stringent requirements on the optical alignment and on the FP cavity length control impose significant challenges in bolometer fabrication and implementation in practice. Ambient temperature variations and radiation of higher power density may produce temperature changes in the bolometer head beyond the limit of the wavelength scanning range of the laser (a temperature change of  $\sim 12$  °C will produce a shift of 1.0 nm of the FPI spectrum). The limitation in the measurement range can be more prominent when the bolometers are operated in a vacuum environment where the temperature rise is expected to be much higher due to the lack of heat transfer to the ambient air compared with the air environment. These drawbacks may render significant challenges in the practical applications of fiber-optic bolometers.



In this work, we report a multi-channel fiber-optic bolometer system, as shown in Figure 3.9 (b), with five bolometers multiplexed using a coarse wavelength division multiplexer (CWDM) and interrogated using a single broadband light source and a high-speed spectrometer. The system can overcome many of the challenges described above. The bolometers here have much simpler structures fabricated by attaching an uncoated silicon pillar and a gold disk at the end of the SMF, as shown schematically in the inset of Figure 3.9 (b), which is easier to fabricate with reduced fabrication steps and less stringent requirement on the optical alignment compared to the earlier bolometers. The low-finesse design of the silicon FPI allows the use of the white-light system for interrogation whose wavelength range covers several FSRs of the fringes from the bolometer. It eliminates the need for the alignment of spectral notches of the reference and sensing bolometers as each bolometer is operated at a different wavelength range and can accommodate much larger environmental temperature variations. All five bolometers (four as sensing and one as reference) share a single light source and spectrometer (Figure 3.9 (b)), which reduces the cost per channel. Although temperature measurement noise is higher compared to the DFB laser-based high-finesse bolometer system, an optimized design of the bolometer structure improves its responsivity to radiation, ultimately leading to better NEPD performance ( $\sim 0.1 \text{ W/m}^2$  with a time constant of  $< 250 \text{ ms}$  tested at normal temperature and pressure). We describe the system design, including the power management of the CWDM challenges and the signal processing that led to the reported NEPD performance. We also study the system noise due to mechanical vibration and its mitigation through a polarization scrambler.

### 3.2.2. Bolometer fabrication and experimental procedure

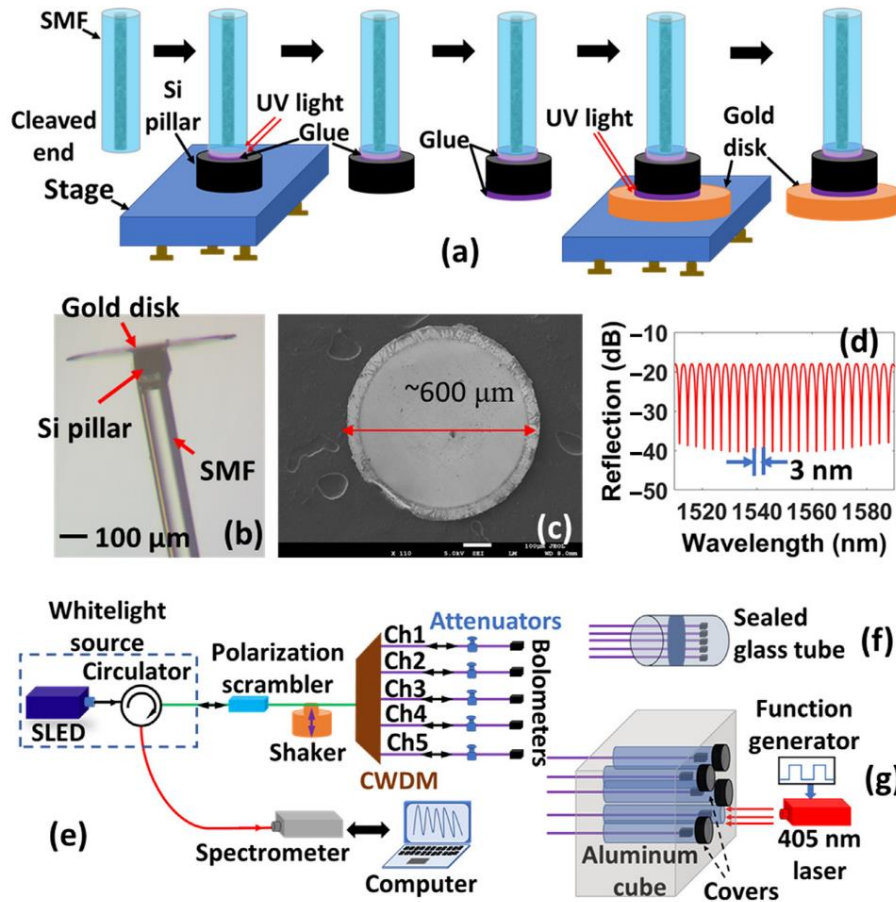


Figure 3.10 (a) Fabrication steps of the fiber-optic bolometers; (b) microscopic image of one of the fabricated bolometers; (c) scanning electron microscope image of the gold disk used to fabricate the bolometer shown in (b); (d) reflection spectrum of the bolometer measured by a fiber-optic sensor interrogator; (e) experimental setup for demonstrating and testing the multichannel bolometer system; (f) bolometers in a sealed glass tube for noise test, and (g) bolometers sealed in an aluminum cube for radiation response measurement.

Fabrication of the fiber-optic bolometers shown in Figure 3.10 (b) has many steps common to those described in [45] and is outlined in Figure 3.10 (a). The silicon pillar was attached at the end of the SMF using UV-curable glue. The thickness and diameter of the silicon pillar were 100 and 150  $\mu\text{m}$ , respectively. A 4  $\mu\text{m}$  thick, 600  $\mu\text{m}$  diameter gold disk was attached on the other side of the silicon pillar using the UV glue. Figure 3.10 (b) shows the microscopic image of one of the fabricated bolometers. Scanning electron microscope images of the gold disk and reflection

spectrum captured by a fiber-optic interrogator (Model: sm125, Micron Optics, Atlanta, GA, USA) in the wavelength range from 1510 to 1590 nm of typical fiber-optical bolometers are shown in Figure 3.10 (c), (d) respectively. The reflection spectrum shows an FSR of  $\sim 3$  nm, consistent with the 100  $\mu\text{m}$  cavity length, and a good fringe visibility of about 20 dB throughout the wavelength range.

The proposed five-channel fiber-optic bolometer system is schematically shown in more detail in Figure 3.10 (e). The light source (Model: DL-BP1-1501A, Ibsen Photonics, Farum, Denmark) was a super luminescent light-emission diode (SLED) centered at 1550 nm with an integrated fiber-optic circulator. The light from the SLED passed through a fiber-optic circulator, and its polarization was randomized using a 5 MHz polarization scrambler (Model: NOPS, Agiltron, Woburn, MA, USA) before the light arrived at an eight-channel CWDM and was split into different channels. Five of them whose center wavelengths ranged from 1510 nm (channel 1) to 1590 nm (channel 5) with a spacing of 20 nm matched the spectral range of the spectrometer and were thus selected for the system. Each of the channels had a 3 dB bandwidth of  $\sim 13$  nm and was connected to a fiber-optic bolometer. An attenuator was also used in each channel before the bolometer to adjust the optical power reflected from the bolometer. The light reflected from the five bolometers was combined using the same CWDM and, after passing through the polarization scrambler, was directed to a high-speed spectrometer based on diffractive gratings and a linear photodiode array (Model: IMON 512 OEM, Ibsen Photonics, Farum, Denmark) through the circulator. The spectrometer recorded the spectrum of the light at a frame rate of 1 kHz over a wavelength range from 1510 to 1595 nm. Note that channel 1 centered at 1510 nm, and channel 5 centered at 1590 nm of the CWDM were only partially covered by the spectrometer. The bolometer

connected to the CWDM channel 1 was used as the reference bolometer and the other four were used for radiation measurement.

Experiments to characterize the bolometer system performance were performed in two ways: one for noise performance analysis and the other for the response to radiation. A noise test was performed by placing all the bolometers in a sealed glass tube, as shown in Figure 3.10 (f), and data were recorded continuously without any radiation applied on the bolometers. To obtain the response to radiation, the light from a 405 nm DFB laser was used to simulate the radiation with the bolometers placed in the sealed holes of an aluminum block whose front side was covered by a glass plate that allowed the radiation to shine on to the gold disk of the fiber-optic bolometer. Radiation was applied only to the intended bolometer for the radiation test, while other bolometers were covered by opaque covers to shield them from the incident light, as shown in Figure 3.10 (g). To test the effect of mechanical vibration on the system performance, an electromagnetic shaker was used to introduce vibration in the fiber connected to the common port of the CWDM, as shown in Figure 3.10 (e).

### **3.2.3. Results**

This section is divided into four parts. Section 3.2.3.1, 3.2.3.2, 3.2.3.3 concern the noise performance and describe, respectively, the effects of the optical power distribution, the choice of fringe peaks or valleys for wavelength tracking, and the mechanical vibration on the temperature resolution of the fiber-optic bolometers. The results justify the use of the attenuator and polarization scrambler in the final setup. Section 3.2.3.4 concerns the characterization of the NEPD performance and the time constants of the fiber-optic bolometers.

### 3.2.3.1. Optical power management

One of the key components in the fiber-optic bolometer system that determines the noise performance of the system is the high-speed spectrometer. We found that the peak intensity of the signal output from the spectrometer and the exposure time set for the spectrometer can affect the noise performance of each of the channels. The exposure time of the spectrometer is the integration time of the on-chip charge amplifier in the photodiode array of the spectrometer that integrates the photodiode current from each pixel. Our results justify the use of attenuators to equalize the peak intensity of the spectrometer for the five channels for optimized overall noise performance.

Specifically, we first studied the effect of the exposure time on the measurement resolution using channel 3 as an example. In this case, we increased the exposure time of the spectrometer from 200 to 900  $\mu\text{s}$  in steps of 100  $\mu\text{s}$ . Note that increasing the exposure time results in a larger gain of the on-chip charge amplifier that amplifies the photodiode current, leading to increased peak intensity of the spectrometer output. For each value of the exposure time, the peak intensity of the spectrum recorded by the spectrometer was maintained at a constant level of  $\sim 55,000$  counts (close to the maximum output value of the spectrometer) by adjusting the attenuator on the channel. Figure 3.11 (a) shows the reflection spectra measured by the spectrometer at three different exposure time values (200, 400, and 800  $\mu\text{s}$ ). For each measured spectrum, the wavelength position of each of the fringe valleys was found by fitting the data points around the valley with a sinusoidal function. Then, the shift of the average of the wavelength position of the five valleys within the wavelength range of the CWDM channel was found and converted to temperature variations using a responsivity of 84 pm/K at 1550 nm [3] (the responsivity was corrected using the center wavelength of the channel). To obtain the noise performance, the reflection spectrum was continuously recorded by the spectrometer for around 60 s at a frame rate of 1 kHz while the

bolometer was kept in a sealed glass tube without applying radiation from a 405 nm laser. To remove the drift generated by the environmental temperature variation, the moving average with an averaging window size of 100 data points (corresponding to 0.1 s in time) of the temperature reading from the reference bolometer was subtracted from the reading of the sensing bolometer. Residual drift was removed by subtracting the linear temperature variation from the actual temperature variation in the fiber-optic bolometer. The standard deviation of the relative temperature variation was used to specify the resolution of the bolometer. The relative temperature variation in the fiber-optic bolometer connected to Ch. 4 is shown in Figure 3.11 (b) when the exposure time of the spectrometer was set at 200, 400, and 800  $\mu\text{s}$ . A resolution of 0.42, 0.38, and 0.32 mK was found for the exposure time of 200, 400, and 800  $\mu\text{s}$ , respectively. Figure 3.11 (c) shows the resolution of the fiber-optic bolometer vs. different exposure times of the spectrometer. It is seen that the value of the resolution reduced as the exposure time increased, which is expected as an increased exposure time corresponds to an increased integration time of the charge amplifier for each of the detector pixels in the photodetector array, resulting in reduced noise from the pixel output. In practice, the maximum exposure time that can be used is determined by the required measurement speed. We also noticed that the improvement in noise performance by increasing the exposure time was moderate. The value of resolution reduced from 0.42 to 0.31 mK when the exposure time increased from 200 to 900  $\mu\text{s}$ .

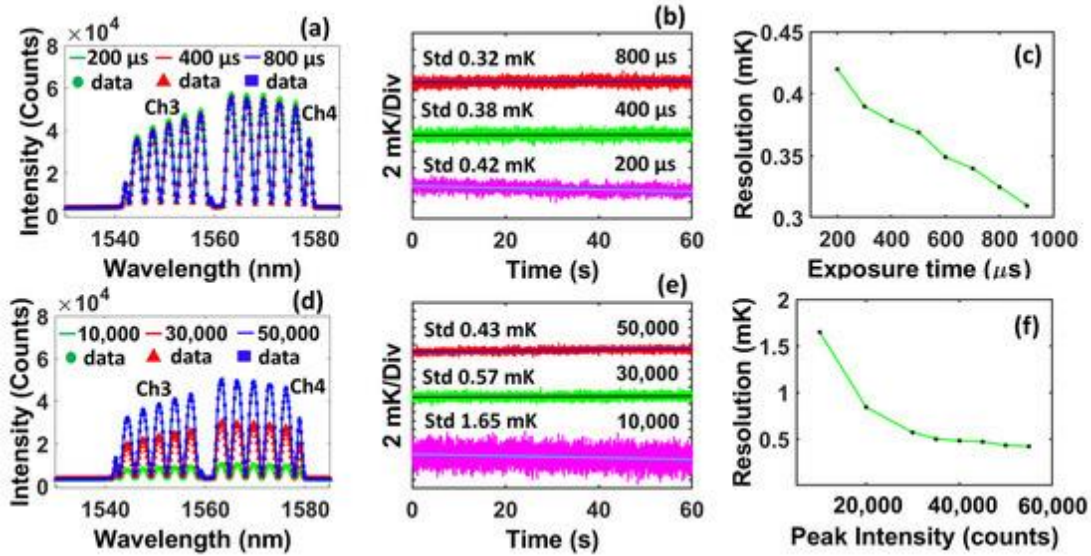


Figure 3.11 (a, d) Reflection spectrum from the fiber-optic bolometers measured by the spectrometer at different exposure times and peak intensities, respectively; (b, e) relative temperature variation measured by the bolometers connected to Ch. 4 at different exposure time values and peak intensities, respectively; and (c, f) variation in the measurement resolution with exposure time values of the high-speed spectrometer and peak intensities, respectively.

Next, we studied the effect of the peak intensity from the spectrum output on the noise performance of the bolometer. In this case, the exposure time was set at 200 μs and maintained at this value during the experiment. The peak intensity of the spectrometer output was increased from 10,000 to 55,000 counts by adjusting the attenuation using an attenuator connected to the light source. Figure 3.11 (d) shows the reflection spectra measured by the spectrometer with three different peak intensity levels (10,000, 30,000, and 50,000 counts). The resolution of the bolometer was characterized following the same process described above. The relative temperature variation measured by the bolometers connected to the channel 4 is shown for three different peak intensities in Figure 3.11 (e). A noise of 1.65, 0.57, and 0.43 mK was found when the maximum peak intensity counts were set to 10,000, 30,000, and 50,000, respectively. Figure 3.11 (f) shows the bolometer resolution as a function of peak intensity. It shows that the value of resolution exponentially increased as the peak intensity reduced, and the resolution was strongly influenced by the peak

intensity when the peak intensity was below  $\sim 35,000$  counts. To achieve optimized measurement resolution, the peak intensity should be maintained at  $>35,000$  counts.

The light source and the spectrometer were shared by all five channels through the CWDM. Because of the non-uniform spectral profile of the light source and the variations in the reflection spectra of individual bolometers, the power spectral densities of the reflected light had large variations among the five channels without the attenuators. Figure 3.12 (a) shows a spectral frame containing the signal from all five bolometers. The exposure time was set at  $\sim 50 \mu\text{s}$  to prevent the saturation of the spectrometer output for channel 4, which had the largest peak intensity at  $\sim 55000$  counts. The fringe valleys used for signal processing are also indicated by the numbers in the figure. The spectrum shows large discrepancies in the peak intensity among the five channels with average peak intensities below 35000, the threshold above which the measurement resolution was not sensitive to the peak intensity, for channels 1, 2, and 5 and above the threshold for channels 3 and 4. Figure 3.12 (b) shows the resolution of the four sensing bolometer channels (channels 2–5) after compensating for the environmental drift from the reference bolometer channel (channel 1). The result shows that channels 3 and 4 had similar resolutions of 0.61 mK. Although the peak intensity for channel 4 was higher than that for channel 3, they exhibited similar resolutions because the intensity of both channels exceeded the threshold of 35000 counts, as shown in Figure 3.11 (d). The resolution increased to 0.72 mK for channel 2 and 0.83 mK for channel 5 due to the reduced peak intensity below 35000 counts for these channels. It is worth noting that the number of fringe valleys available for signal processing for channel 5 was less than that for other channels connected to the sensing bolometers because of the limited wavelength range of the spectrometer. Five fringe valleys were used for channel 2, while only four valleys were available for channel 5.

Thus, channel 5 showed a worse resolution despite its stronger peak intensity compared with channel 2.

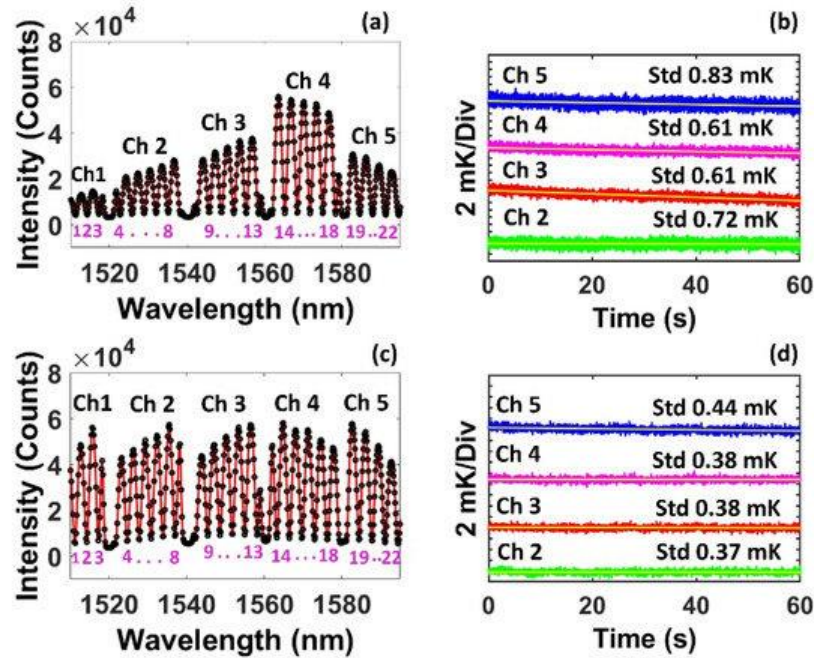


Figure 3.12 (a, c) Reflection spectrum from the fiber-optic bolometers captured by the spectrometer without the attenuator and with the power balanced by the attenuators, respectively; (b, d) relative temperature variation for channels 2–5 without the attenuator and with the power balanced by the attenuators, respectively.

Using the attenuators in the five channels, we adjusted the peak intensity of each of the channels and the exposure time of the spectrometer, which brought the peak intensities for the five channels to a similar level of 55000 counts, as shown in Figure 3.12 (c). Reaching this maximum peak intensity for all the channels required a larger exposure time set for the spectrometer, which offered additional enhancement to the noise performance. Figure 3.12 (d) shows the noise performance for this power-balanced configuration. The four sensing bolometers showed a similar measurement resolution around 0.4 mK (ranging between 0.37 and 0.44 mK), which was smaller than the case without attenuators shown in Figure 3.12 (b). The variation in the resolution is

attributed to the difference in the power variations within each channel that cannot be balanced by the attenuator.

### **3.2.3.2. Difference in Tracking of Fringes Valleys and Fringe Peaks**

In theory, wavelength tracking can be performed on either fringe valleys or fringe peaks. However, we found that the choice of tracking valleys and tracking peaks has a large effect on the noise performance. Figure 3.13 (a) represents the reflection spectrum for tracking the peaks for the five bolometers with a balanced peak intensity. Note that the spectrum is identical to that shown in Figure 3.12 (c). The number of peaks used for signal processing is identical to the number of valleys used for signal processing for channels 1 and 5; while the number of peaks is greater than the number of valleys by one for the other three channels (channels 2–4). The peak wavelength was found following the same algorithm used for finding the valley wavelength. Figure 3.13 (b) shows the resolution for the four sensing bolometers using fringe peak tracking. Compared with valley tracking, peak tracking exhibited remarkably worse noise performance for all channels despite using more peaks than valleys in channels 2–4. The measurement resolutions also show large variations ranging from 0.60 mK for channel 2 to 1.56 mK for channel 5. The degradation in the noise performance from fringe valley tracking to peak tracking can be explained as follows: the noise of the pixel output is proportional to the light intensity; thus, the pixels around the fringe peaks show larger noise than those around the valleys, resulting in larger variations in the results from the curve fitting using the data points around the peaks.

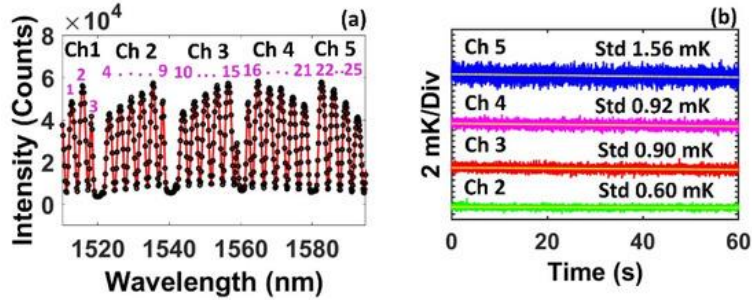


Figure 3.13 (a) Reflection spectrum from the fiber-optic bolometers captured by the spectrometer with the power balanced by the attenuators for peak tracking; (b) relative temperature variation for channels 2–5 found from peak tracking.

### 3.2.3.3. Effect of Mechanical Vibration

Large mechanical vibration can be present in a magnetic-confinement fusion system that may affect the signal from an optical diagnostic system. For example, it has been shown that mechanical vibration can cause movements up to 1 cm at frequencies of a few hertz for the interferometry measurement system on tokamaks [66, 67]. Signal contamination from mechanical vibration is also a concern for the fiber-optic bolometer system. Silicon pillars that form the FP cavity in a bolometer may have a small birefringence due to the thermal stress and elastic strains of the silicon wafer from which the pillars are manufactured [68]. The birefringence makes the bolometer sensitive to light polarizations. Previously, we demonstrated that fiber-optic bolometers interrogated using linearly polarized light from a DFB laser show significant noise degradation from mechanical vibration that induces birefringence to the fiber and subsequently changes the polarization of the light in the fiber [69]. The light source used here is a SLED, which may have non-negligible degree of polarization. Therefore, it is important to study the effect of mechanical vibration on the noise performance of the system.

After optimizing the experimental setup with an attenuator to balance the peak intensity of the channels and using fringe valley tracking for signal processing, mechanical vibration was applied by using an electromagnetic shaker in the fiber before the CWDM. The vibration was

applied using frequencies of 5, 10, and 100 Hz with peak-to-peak sinusoidal displacements of  $\sim 7$ ,  $\sim 5$ , and  $\sim 1$  mm, respectively. Figure 3.14 (a) shows the relative temperature variation for the sensing bolometers in channels 2–5 in the case of the 5 Hz vibration applied on the fiber. It was seen that the vibration significantly degraded the noise performance with the temperature resolution being 0.73, 4.2, 6.2, and 0.92 mK for channels 2–5, respectively. It is believed that the degradation of noise performance is determined by the birefringence of the silicon pillars and the orientation of the light polarization relative to the principal axes of the birefringence, both of which are uncontrolled during the construction of the bolometer and during the operation of the bolometer system. Therefore, the level of performance degradation shows a great variation among the four sensing bolometers.

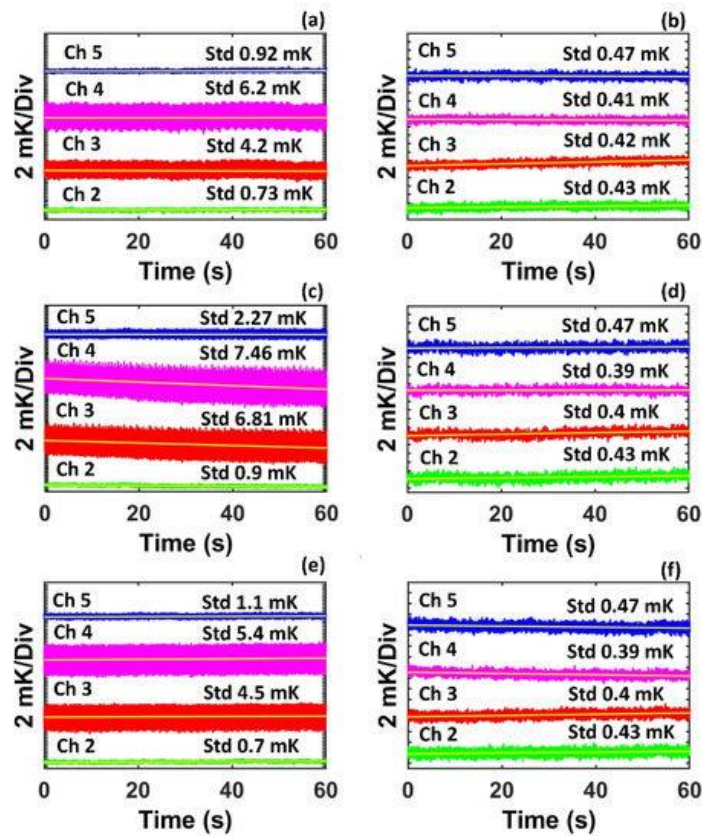


Figure 3.14 (a, c, e) System noise under 5, 10, and 100 Hz vibration, respectively, without a polarization scrambler; (b, d, f) system noise 5, 10, and 100 Hz vibration, respectively, when the polarization scrambler was on.

To mitigate the effect of the mechanical vibration, a polarization scrambler was used after the SLED to randomize the polarization state at a speed (5 MHz) much higher than the frame rate (1 kHz) of the spectrometer. Therefore, the light injected into the bolometer can be considered as unpolarized, which is insensitive to the changes in the birefringence induced by the mechanical vibration. Figure 3.14 (b) shows the resolution after the polarization scrambler was applied when the fiber was experiencing the 5 Hz mechanical vibration. The results show that channels 2–5 had a much lower and similar noise level of ~0.43 mK (ranging between 0.41 and 0.47 mK), which is comparable to the noise performance when there was no vibration, as shown in Figure 3.12 (d).

A similar effect was found when vibration was applied at a frequency of 10 and 100 Hz. Noise levels were higher and non-uniform among the sensing bolometers with the application of vibration and without polarization scrambling; the noise levels reduced to ~0.42 mK, uniformly for all bolometers after the use of the polarization scrambler, as shown in Figure 3.14 (c)–(f). The results show that the polarization scrambler is effective for mitigating the degradation from mechanical vibration.

#### **3.2.3.4. NEPDs and Time Constants**

The responsivities and time constants of the four sensing bolometers (channels 2–5) were characterized by exposing the bolometers to radiation from a 405 nm laser modulated by a square wave of 0.1 Hz with different levels of amplitude. Figure 3.15 (a)–(d) shows the relative temperature changes of the bolometer when radiation with a power density amplitude of  $74 \text{ W/m}^2$  impinged on to the bolometers. The average temperature rise when the bolometers reached a steady state was 272 mK (range: 222–312 mK), corresponding to an average responsivity of  $3.68 \text{ mK}/(\text{W/m}^2)$  (range: 3.0–4.2  $\text{mK}/(\text{W/m}^2)$ ). The insets of Figure 3.15 (a)–(d) show the close-up views of the responses at the transient in response to the step changes of the radiation. The time

constant of each bolometer, which is a measure of the measurement speed of the bolometer, was found by the time it took for the temperature to fall to 63% of the overall temperature change during the cycle when the laser was switched off. The average time constant of the bolometer was 223 ms (range: 192–235 ms). The variations in the responsivity and the time constant among the four bolometers are believed to arise from different amounts of glue and/or from the variation in the gold disk sizes used to fabricate each of the bolometers that affect the thermal mass of the bolometers and the heat transfer process between the bolometers and the ambient air.

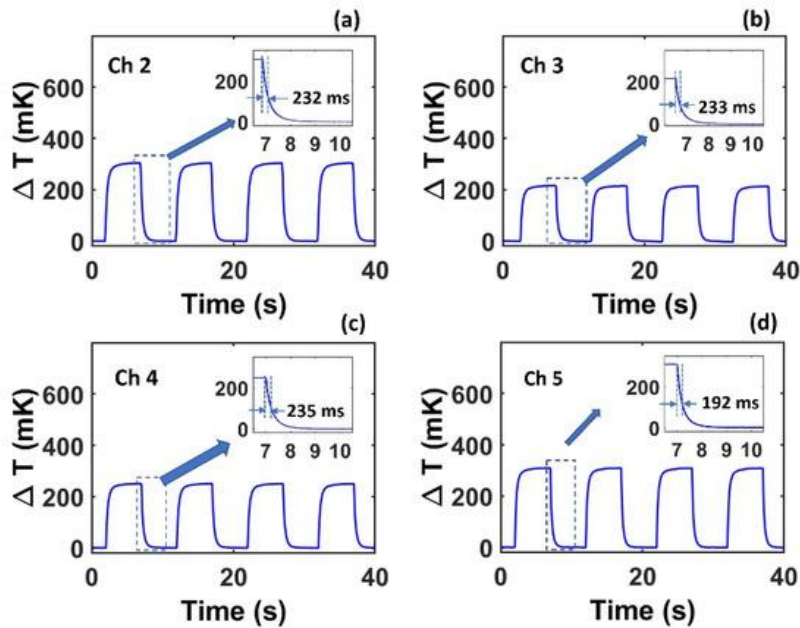


Figure 3.15 The response of the bolometers connected to channels 2 (a), 3 (b), 4 (c), and 5 (d) when each of them was exposed to a 0.1 Hz square wave power flux at  $\sim 74$  W/m<sup>2</sup>. Insets are the close-up view of the falling transients of the responses.

To characterize the NEPD for each bolometer, we exposed the bolometer with radiation of different levels of amplitude and calculated the signal-to-noise ratio (SNR) at each radiation level. The SNR was found by dividing the temperature rise from the radiation when the bolometer reached a steady state by  $\sqrt{2}\sigma_T$ , where  $\sigma_T$  is the temperature resolution of the bolometer defined in Section 3.2.3.1, Section 3.2.3.2, Section 3.2.3.3, and Section 3.2.3.4. Figure 3. (a)–(d) shows

the SNR vs. power density for the four sensing bolometers. The NEPD is the power density level corresponding to a unity SNR, which can be found from the linear fitting line shown in Figure 3.. The average NEPD for the four bolometers was  $0.10 \text{ W/m}^2$  (range:  $0.07\text{--}0.12 \text{ W/m}^2$ ), which is similar to the NEPD of the fiber-optic bolometer based on a high-finesse silicon FPI interrogated using a wavelength-scanning DFB laser [7]. Again, the variation in the NEPD among the sensing bolometers is attributed to the fabrication variations resulting in different thermal masses of bolometers.

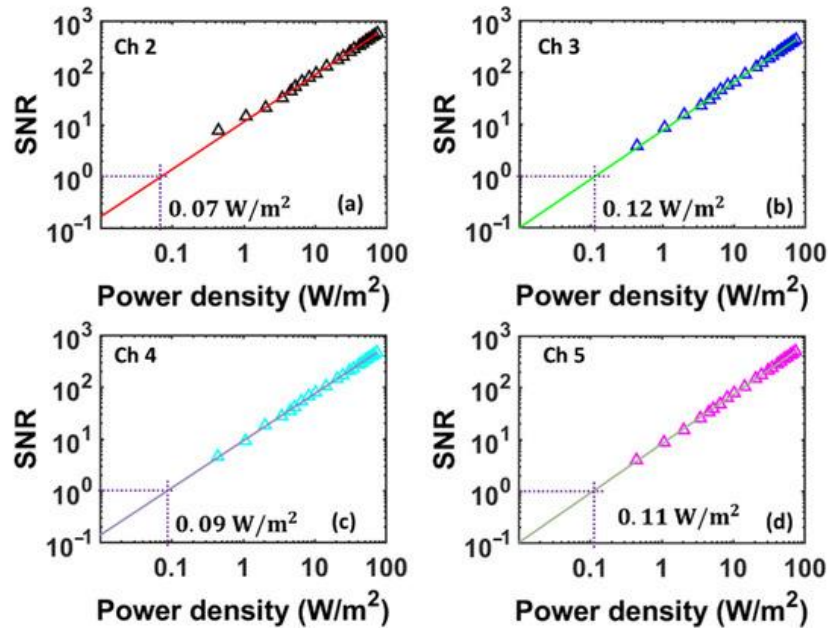


Figure 3.16 (a–d) Measured SNR vs. power density for the bolometers connected to channels 2–5, respectively.

### 3.2.4. Summary

Several factors need to be considered in choosing the diameter and thickness of the silicon pillars used for fabrication of the fiber-optic bolometers. A silicon pillar with a smaller diameter will have a shorter response time. However, the diameter needs to be sufficiently large to provide a sufficient end surface for robust bonding between the silicon pillar and the relatively large gold disk. The thickness of the pillar determines the cavity length of the FPI and consequently the FSR

of the FPI. Short pillars have coarse fringes that may result in reduced wavelength measurement resolution; while long pillars may result in dense fringes that cannot be resolved by the spectrometer.

Both the responsivity and the time constant of a fiber-optic bolometer are affected by the efficiency of the thermal pathways for the heat dissipation from the bolometer head to the surrounding environment. In this work, they were measured at around normal temperature and pressure, and the heat transfer involves the natural convection to the ambient air and the conduction to the fiber stub. The responsivity and the time constant characterized in these conditions may not be representative of the bolometers in a vacuum environment where there is no convection. However, they can be used for performance comparison with other fiber-optic bolometer systems that have been tested under similar conditions.

In conclusion, we report a multichannel fiber-optic bolometer system intended for measuring the plasma radiation from the fusion chamber. The system consists of five bolometers (one reference bolometer and four sensing bolometers) that are multiplexed using a CWDM and interrogated using a single light source and a high-speed spectrometer. System parameters are configured to achieve optimized noise performance and resistance to mechanical vibration. The experimental result suggests that the bolometers have an NEPD of  $\sim 0.1 \text{ W/m}^2$  with a time constant of  $\sim 220 \text{ ms}$  under normal temperature and pressure. These performances are comparable to the more complicated fiber-optic bolometer system based on high-finesse FPIs. This multichannel fiber-optic bolometer system offers simple bolometer fabrication, good noise performance, lower cost per channel, and large dynamic range, which makes it attractive for plasma radiation measurement in magnetic-confinement fusion systems.

### **3.3. FOB with heat sink for plasma radiation measurement in vacuum**

The intended application of the FOB is in vacuum condition to measure the plasma radiation. Fewer particles will be present in the vacuum condition and mean free path will be high which will make the convective heat transfer very insignificant. Conduction and radiation will be the only way to dissipate the heat in vacuum whereas radiation is unlikely to happen at this low temperature (several 100 mK). FOB fabricated by using the silicon pillar and gold disk has no efficient path of heat conduction as the silicon pillar is connected to the optical fiber made of glass. A heat sink can be added to increase the heat dissipation from the heated silicon to the heat sink by conduction process in vacuum condition. FOB without the heat sink will take long time to reach in thermal equilibrium after being exposed with radiation in vacuum. Response time of the current FOB with the silicon pillar and gold disk in vacuum is very high (several seconds) which will make the FOB utilization challenging for reconstructing the fast-changing radiation profile. 405 nm laser was modulated by a square wave with a 120 s period to simulate the radiation keeping the FOB in  $\sim 10^{-6}$  Torr pressure level as shown in Figure 3.18 (a). Absorbed heat was dissipated in vacuum through inefficient radiation and conduction which increased the time required to reach in thermal equilibrium. The response time of more than 5 s was found for the FOB with gold disk and silicon pillar in vacuum condition as shown in Figure 3.17 (b) and (c).

Sensor configuration needed to change to make the heat transfer more efficient in vacuum by adding a heat sink along with the signal demodulation method. This chapter describes some of the work done to make the FOB operation efficient for vacuum application in fusion devices. Firstly, FOB fabrication was changed to incorporate a silicon heat sink and secondly the input radiation was recovered using deconvolution method with reduced time constant. Also, we describe some of the future direction of the FOB operation in the real fusion devices.

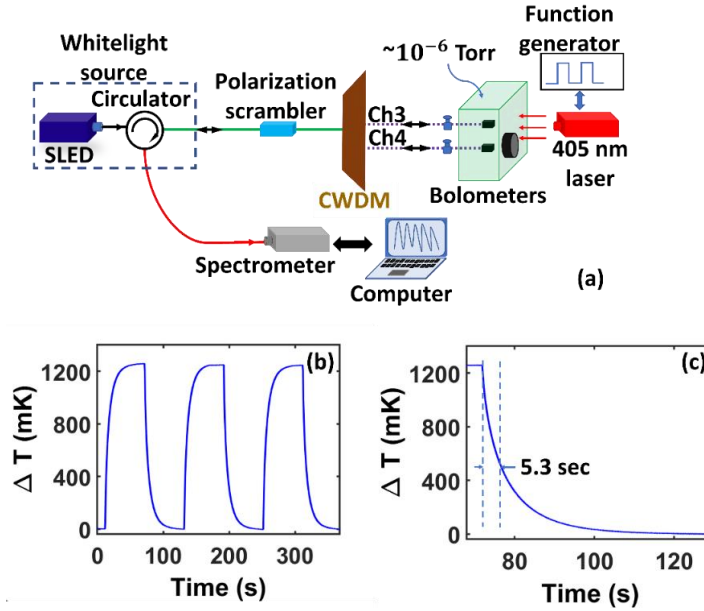


Figure 3.17 (a) Experimental set up for FOB radiation response in vacuum, (b) Time history change of temperature for square wave modulated radiation, (c) zoom in view of the falling temperature change.

Section 3.3.1 will discuss the deconvolution method to reconstruct the input radiation profile. To improve the temporal response of the FOB, deconvolution method can be applied to the FOB response using the information of the impulse response for the same FOB system. Besides, sensor configuration can be modified to incorporate heat conduction to facilitate the heat transfer in vacuum condition which will be discussed in section 3.3.2. Both processes have been applied to make FOB applicable for plasma radiation measurement in the fusion devices will be on section 3.3.3.

### 3.3.1. Deconvolution method

Deconvolution implies the process of decomposing of a spectrum into its separate additive peak components where the underlying peak shape is unknown with the information of the broadening function. The practical significance of Fourier deconvolution in signal processing is that it can be used as a computational way to reverse the result of a convolution occurring in the physical domain, for example, the finite resolution of a spectrometer.

### 3.3.1.1. Background

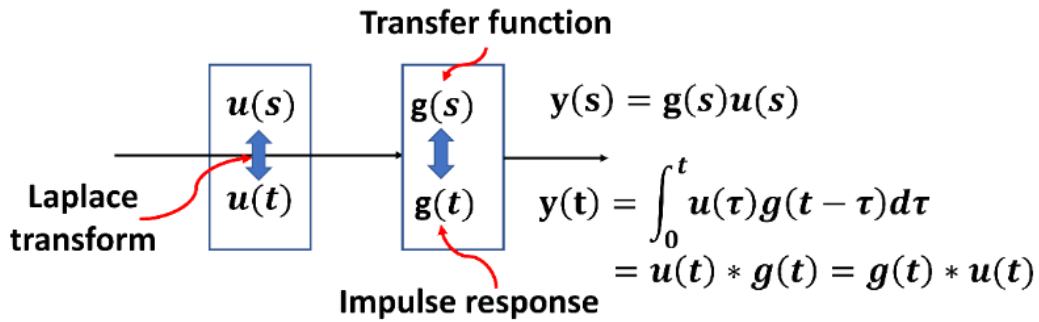


Figure 3.18 Convolution theorem in time and frequency domain.

Given the input to a linear time-invariant system, the output can be determined in time and frequency domain using the convolution theorem. In the time domain, the output can be found as the convolution of the impulse response and the input. On the other hand, in the Laplace domain the output is found as the multiplication of the transfer function and the Laplace transform of the input. Deconvolution method will be the reverse process of the convolution method where output and impulse response will be used to reconstruct input signal. Figure 3.19 (a) and (b) shows the experimental set up for measuring the radiation response by the FOB and photodetector, respectively. The impulse response can be found by using the radiation with the shortest possible pulse. This will be the transfer function of the system as it contains the information for all frequency components. This transfer function was used to find the deconvoluted input. A photodetector (PD) was used to measure the radiation and compared with the deconvoluted input to find the feasibility of the deconvolution method.

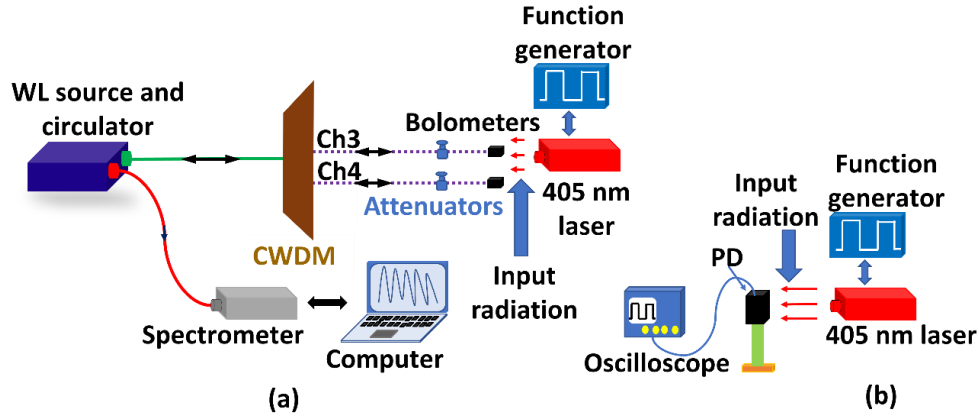


Figure 3.19 (a) Experimental set up for radiation test and to measure the incident radiation using photodetector (b).

Input radiation was measured by using photodetector and compared with the reconstructed input signal by deconvolution method using the transfer function derived from impulse response and output response for the intended radiation.

Figure 3.20 (a) shows the impulse response from the FOB for the radiation modulated by the square wave with the period and pulse width of 10 s and 1 ms, respectively. FOB was irradiated by the 405 nm laser modulated by an arbitrary radiation generated by using the three gaussian pulse.

To find out the transfer function,  $F(s)$  of the system, first impulse response was obtained in time domain,  $h(t)$  by applying radiation modulated by short pulse square wave in time domain and which is  $h(s)$  in frequency domain.

$$\delta(t) \rightarrow \text{FOB} \rightarrow h(t) \quad (3.2)$$

$$1 \rightarrow F(s) \rightarrow h(s) \quad (3.3)$$

This impulse response is the transfer function of the system. So, the transfer function,  $F(s)=h(s)$ . The FOB response was found out by the radiation modulated by gaussian pulses;  $y(t)$  as shown in

Figure 3.20. This FOB response in time domain can be converted to frequency domain by using Fourier transform.

$$g_3(t) \rightarrow \text{FOB} \rightarrow y(t) \quad (3.4)$$

$$g_3(s) \rightarrow F(s) \rightarrow y(s) \quad (3.5)$$

The FOB response for a three pulse gaussian waveform can be found by the ratio of the FOB output and the transfer function in frequency domain. At the same time, the input can be measured by the photodetector directly which is shown in

Figure 3.20 (c). The PD output and deconvoluted input are compared in

Figure 3.20 (c). The two signals match with each other which proves the feasibility of using the deconvolution in reconstructing the radiation profile.

$$F(s) = y(s)/g_3(s) \quad (3.6)$$

$$g_3(s) = y(s)/F(s) \quad (3.7)$$

$$g_3(t) = L^{-1}(g_3(s)) \quad (3.8)$$

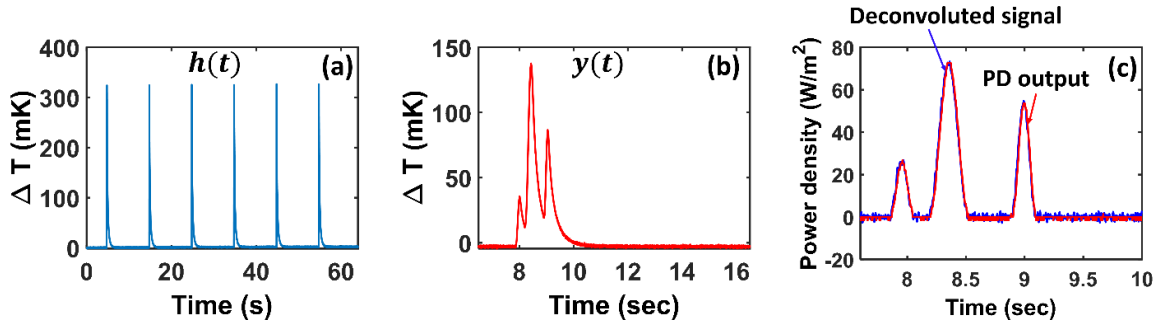


Figure 3.20 (a) impulse response, (b) FOB output and (c) deconvoluted and photodetector signal.

### 3.3.1.2. Signal processing

Figure 3.21 shows the signal processing method for finding the input radiation using the deconvolution method. Impulse response was found by radiating the FOB with short square wave pulse of 1ms in ambient condition. Noise was subtracted to get the actual impulse response shown

in Figure 3.21 (a). A close look of the impulse response showed the existing linear drift which can be easily removed by using linear fitting (Figure 3.21 (c)). The average of the multiple (six in this case) pulses of the impulse response was used as the impulse signal in time domain for further process. Fourier transform of the impulse response can be converted to the actual power density by dividing the zero-frequency amplitude by the same amplitude and setting the zero-frequency amplitude to the original power density measured by the photodetector. Fourier transform of the FOB response for the radiation modulated by four arbitrary gaussian pulses was used as the output response. Input radiation in the frequency domain can be found by the ratio of the output response of the FOB and the transfer function (impulse response) in frequency domain. Input radiation can be reconstructed after using a filter with a cut off frequency of 60 Hz in terms of the power density by using inverse Fourier transform. Then the deconvoluted signal and photodetector signal was compared in terms of actual power density of the input radiation. Exact match of the input radiation measured by the photodetector and reconstructed by the deconvolution proves the feasibility of the deconvolution method. Main advantage of this method is visible from the comparison of the original FOB response (Figure 3.21 (h)) and deconvoluted signal (Figure 3.21 (j)). The FOB response for arbitrary input radiation was not able to follow the fast-changing input radiation whereas the deconvoluted signal shows the exact shape and amplitude of the input radiation. The NEPD was found  $1.1 \text{ W/m}^2$  using the above-mentioned signal processing.

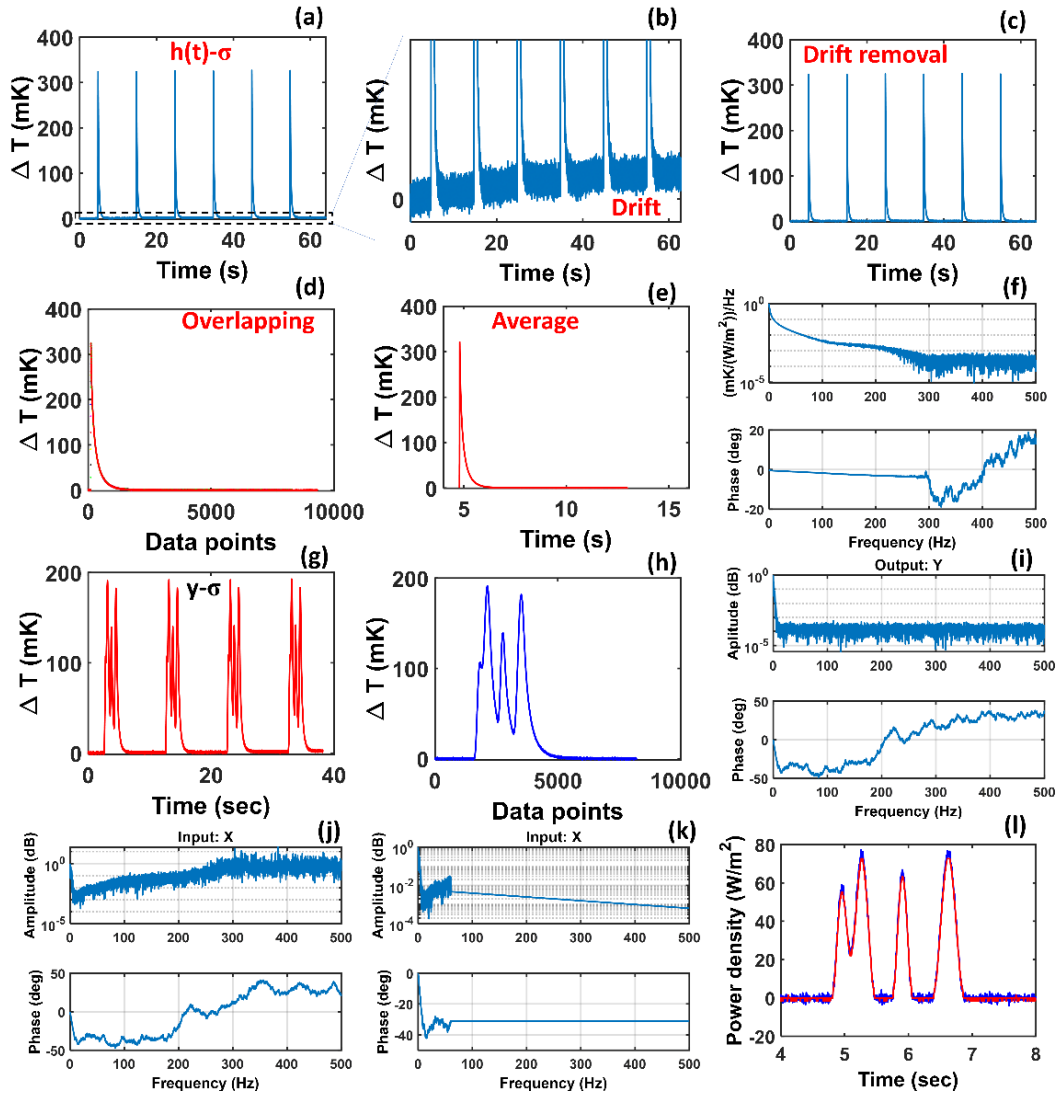


Figure 3.21 Deconvolution algorithm (a) noise subtracted impulse response, (b) zoom in view which shows the temperature drift, (c) linear temperature drift removed, (d) overlapping six pulses with each other, (e) average of six impulse responses, (f) impulse response in frequency domain with actual amplitude using the power density of dc response, (g) FOB response with radiation of four pulses with different amplitude, (h) noise subtracted FOB response in time domain and drift compensated, (i) FOB response for four pulses in frequency domain, (j) input which can be found by dividing the output by the transfer function from (f), (j) converting the signal into double side with complex conjugate, and (l) input radiation with actual amplitude.

The response time of the FOB using the deconvolution can be found from the FOB response with the input radiation modulated by the square wave. Figure 3.22 (a) shows the FOB response for the radiation coming from the 405 nm laser modulated by a square wave with period of 10 s. The FOB response time was found more than 200 ms for the case when it was measured

in air directly from the response of FOB for the square modulated radiation. A response time of  $\sim 10$  ms was found from the deconvoluted signal for the same FOB with radiation applied. Deconvolution helped to improve the underlying unknown peaks by improving the time resolution. A NEPD of  $1.1 \text{ W/m}^2$  was found from the deconvoluted signal.

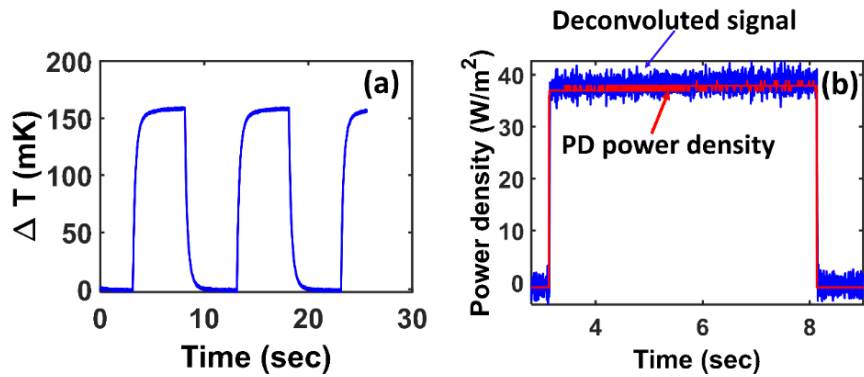


Figure 3.22 (a) FOB response for square modulated radiation, (b) Deconvoluted input and radiation measured by the photodetector.

### 3.3.2. FOB with heat sink

#### 3.3.2.1. Fabrication of the FOB

This section describes the new FOB fabrication to reduce the time constant with the addition of a heat sink to make the thermal heat transfer efficient in the vacuum condition.

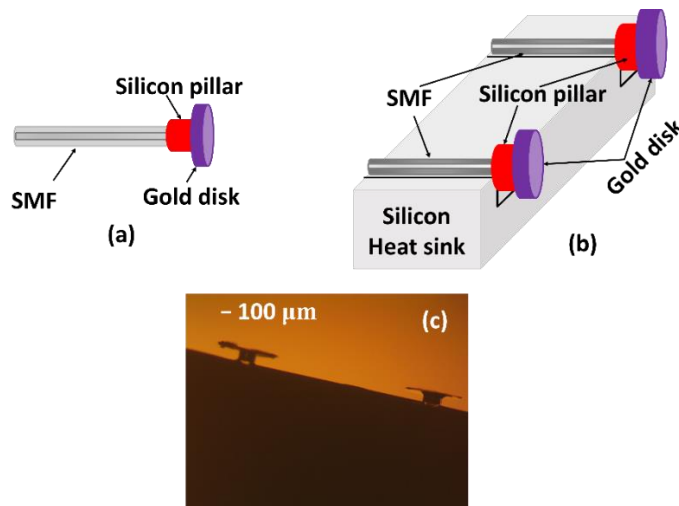


Figure 3.23 (a) Schematic diagram of FOB with silicon pillar and gold disk, (b) Schematic diagram of the FOBs with Silicon heat sink, (c) microscopic image of the fabricated FOB with Silicon heat sink.

Heat transfer in the FOB without the heat sink as shown in Figure 3.23 (a) which was used to measure radiation profile in air was mostly through the convection. The intended use of the FOB to measure plasma radiation from the fusion devices can be done efficiently by using the FOB with the heat sink. Responsivity is proportional to time constant. It is obvious that, responsivity will be sacrificed while reducing the time constant. A FOB was fabricated by using a silicon pillar (100  $\mu\text{m}$  thick and 200  $\mu\text{m}$  diameter) at the end of a single mode fiber and 5  $\mu\text{m}$  thick and 700  $\mu\text{m}$  diameter gold disk was attached at the other side silicon pillar (Figure 3.23 (a)). This FOB was placed in a silicon heat sink (length 5 mm, width 3 mm, height 0.5 mm) with a trench of (length 5 mm, width 0.15 mm, height 0.25 mm) and a thermal connection was made using UV curable glue as shown in Figure 3.23 (b). The same procedure was followed for the other FOB in another trench of the silicon heat sink. A microscopic image of the fabricated two FOBs with Si heat sink is shown in Figure 3.23 (c). One of the FOBs will be radiated for measuring the plasma radiation coming from the fusion devices

### **3.3.2.2. Experimental results in air**

Square modulated 405 nm laser radiation was used to radiate one of the FOBs (sensing bolometer) with heat sink and other FOB (reference bolometer) was covered by opaque sample so that radiation does not fall on the reference bolometer (RB). The sensing bolometer (SB) response shows a periodic change of temperature corresponding to the laser power variation. When radiation is applied to the gold disk of the SB, it absorbs the laser radiation and gets heated. The silicon pillar gets heated as soon as the heat is transferred from the gold disk. This fast response is the sharp transition of temperature as shown in Figure 3.24. Then the heat is transferred to the silicon heat sink from the heated silicon pillar eventually. The heat transfer from the silicon pillar to the silicon heat sink is an ongoing process for a very long time. This is obvious from the slowly rising

temperature response from FOB even in the period of 10 s as shown in Figure 3.24 (a). The heat was conducted to the reference bolometer and the slowly rising temperature was prominent due to this conducted heat from the sensing bolometer. The opposite phenomena occurred when the laser was turned off. This slowly rising/falling temperature needed to be compensated for finding the equilibrium temperature to find the response time of the fabricated bolometer with heat sink. Using the reference bolometer, the slowly rising/falling temperature can be compensated, and a flat response can be obtained after the sharp transition. Figure 3.24 (b) shows the slowly rising/falling compensated result which can be used to find the response time of the FOB with the heat sink. A response time of 36 ms was found which is shown in the zoom in falling transition in Figure 3.24 (c). The FOB with silicon heat sink shows a promising prospect for reducing the time constant.

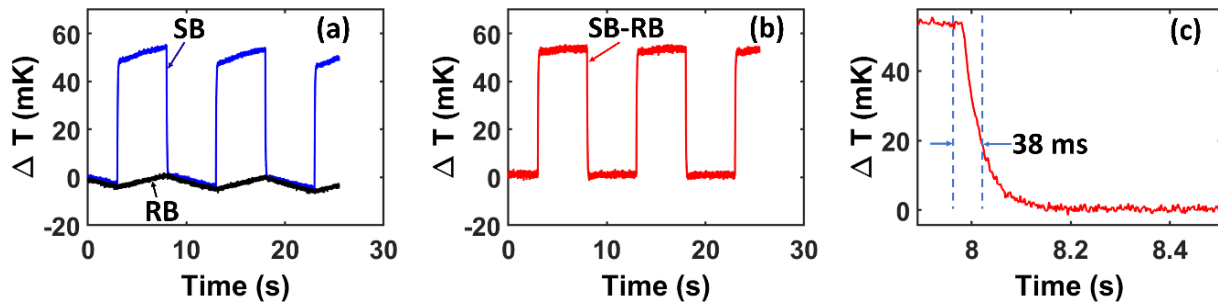


Figure 3.24 (a) FOB response for the radiation modulated by square wave, (b) zoom in view of the falling edge. SB: sensing bolometer, RB: reference bolometer.

FOBs with the silicon heat sink can be kept in between two metal sinks to incorporate more heat conduction. This structure was also studied using simulation and experiment but not included in this dissertation. Overall, modifying the sensor structure and using deconvolution method helped to reduce the time constant when the bolometer was tested in air. Deconvolution method reduced the time constant to  $\sim 10$  ms from  $\sim 230$  ms. On the other hand, response time reduced to  $\sim 38$  ms from  $\sim 230$  ms adding a silicon heat sink. This proves the feasibility of using the two methods to reduce the time constant. Modification of the sensor structure and utilization of the

deconvolution method was analyzed separately for the experiment performed in air. Now the FOB with a heat sink can be utilized in a vacuum condition and the deconvolution method can be applied to reconstruct the input radiation profile with satisfactory response time.

### **3.3.3. FOB with heat sink in vacuum**

The FOB connected to the silicon heat sink will dissipate the absorbed heat through conduction, convection, and radiation. This makes the current configuration of the FOB with silicon heat sink applicable in the fusion devices. The deconvolution method additionally helped to improve the time resolution. So, the FOB with a heat sink will be the best solution for plasma radiation measurements with deconvolution method. To demonstrate this, FOBs with silicon heat sinks were tested in vacuum after applying radiation to the FOB head shown in Figure 3.25 (a). Figure 3.25 (b) shows the relative temperature variation of the FOBs with radiation when the FOB was in  $\sim 10^{-6}$  Torr pressure level. The sensing bolometer (SB) has a large temperature ( $\sim 200$  mK) variation due to the radiation directly on it. Heat was transferred to the other FOB (reference bolometer) by conduction through the heat sink. For compensating the slowly rising/falling trend due to the heat transfer from the silicon pillar to the heat sink, the response of the reference FOB was subtracted from the response of the sensing FOB on which the radiation was applied. Figure 3.25 (c) shows the slowly rising/falling compensated temperature variation. A linear drift was prominent after the compensation which was compensated using the linear fitting. Response time of 100 ms was found using the silicon heat sink in vacuum condition which is shown in Figure 3.25 (d) by zooming in the falling temperature variation.

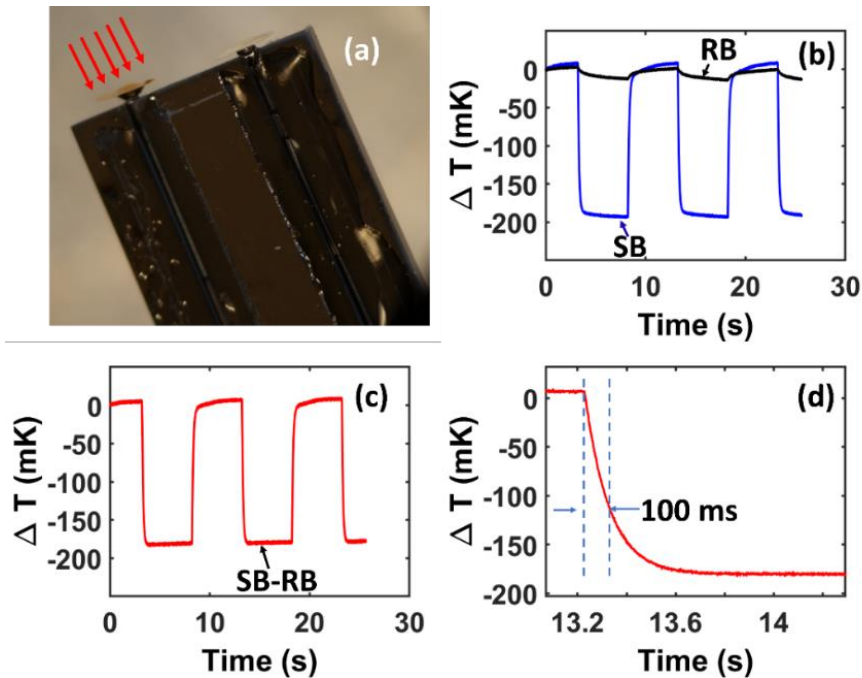


Figure 3.25 (a) microscopic image of the FOB on silicon heat sink, (b) relative temperature variation for the FOB with silicon heat sink for square modulated radiation, (c) slowly rising/falling temperature compensation, and (d) zoom in view of the falling temperature.

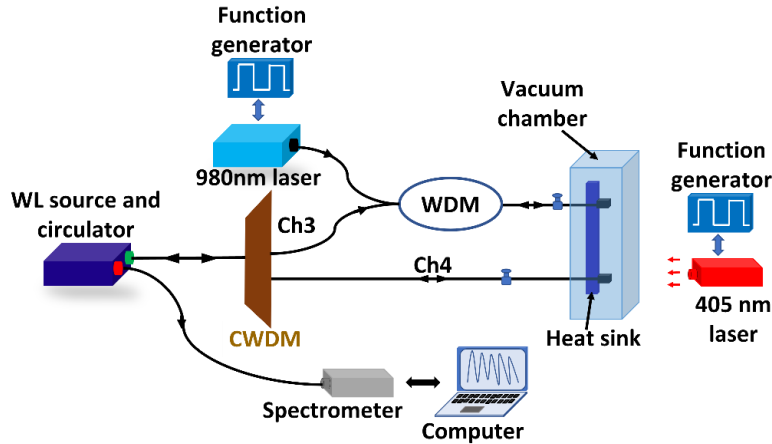


Figure 3.26 Experimental set up for testing the FOB in vacuum.

The response time of  $\sim 5$  s can be reduced to 100 ms by using the heat sink in vacuum condition. Again, using the deconvolution method response time can further be reduced. The impulse response was found by using a 980 nm laser which was used to directly heat the silicon pillar through a wavelength division multiplexer (WDM) as shown in Figure 3.26. A radiation test

was performed using a 405 nm laser, while the 980 nm was turned off. A response time of 20 ms was found using the deconvolution method which is shown in Figure 3.27. A proper FOB geometry can be finalized to get optimum response time with optimum responsivity depending on the application. Figure 3.27 (a)-(g) show the signal processing method to reconstruct the input radiation falling on the FOB head which is same as previously described.

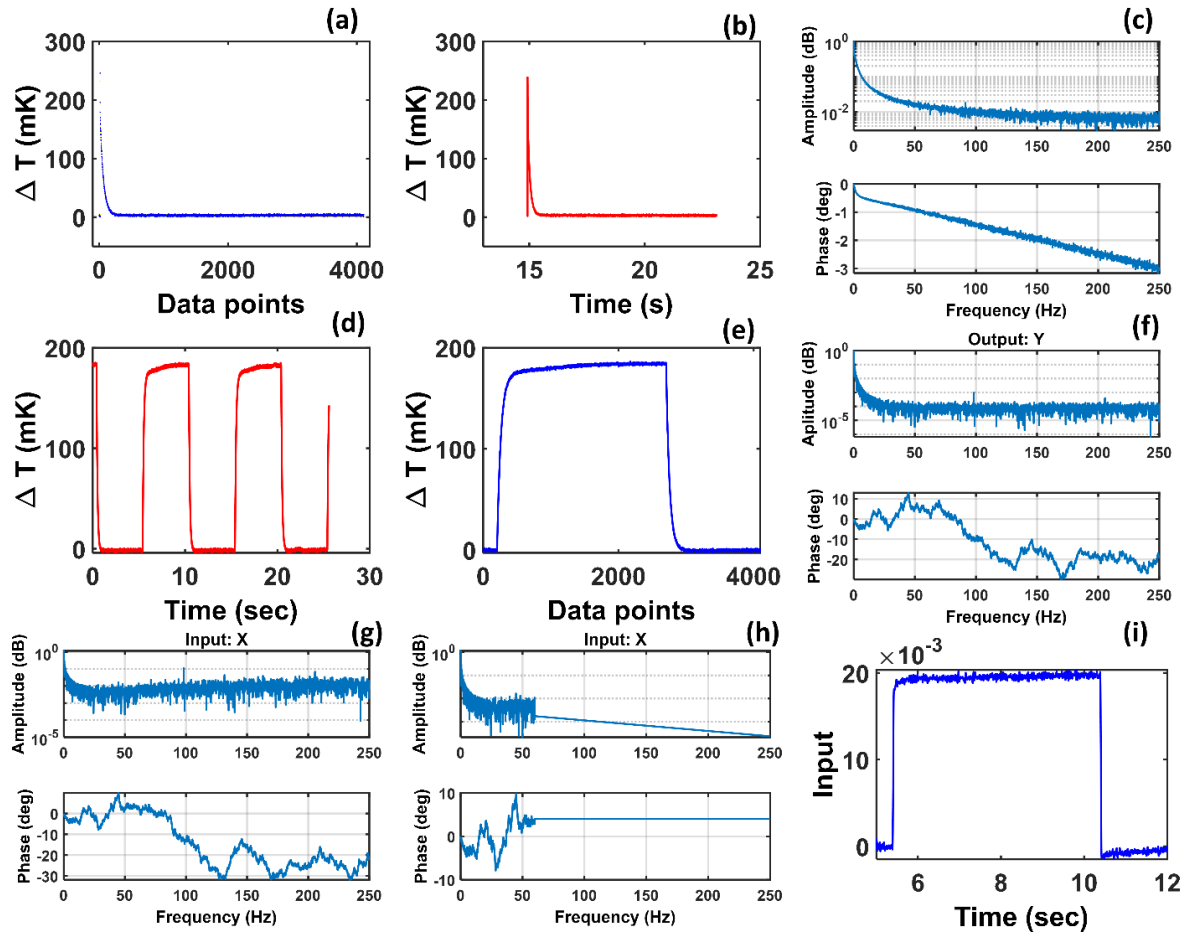


Figure 3.27 Deconvolution algorithm (a) overlapping of two impulse responses, (b) average of two impulse responses, (c) impulse response in frequency domain, (d) FOB response with the square modulated radiation, (e) chosen window of the noise subtracted FOB response in time domain, (f) FOB response in frequency domain, (g) input which can be found by dividing the output by the transfer function, (h) converting the signal into double side with complex conjugate with filter cut off 60Hz, and (i) reconstructed input radiation.

## Chapter 4: Conclusion and Future work

### 4.1. Summary

We have demonstrated the utilization of a fiber-optic silicon Fabry-Perot interferometric temperature sensor as the anemometer. Firstly, constant temperature operation of the anemometer was demonstrated. The time constant and 3 dB bandwidth were improved significantly for the constant temperature operation compared to the constant power operation of the hot wire anemometer. The significantly improved frequency response makes the fiber-optic hot-wire anemometer more attractive for measuring turbulences with rapidly changing flows. Secondly, a flow sensor head using a metal tin shell delivered more uniform response to different flow directions. Finally, compensating the effect of the water temperature variation made the fiber-optic water flow sensor more usable in the turbulence measurement.

Several experiments were performed to improve the performance of the fiber-optic bolometer based on a silicon Fabry-Perot interferometer. Firstly, a larger gold disk was added to the silicon pillar to improve the detection limit. The new FOB with the larger gold disk has higher responsivity (approximately nine times higher) and improved NEPD (approximately six times smaller) when it was tested using a 405 nm laser. In addition, the thick gold disk can improve the absorption of the FOB for high-energy photons. Secondly, multichannel FOB system performances were comparable to the more complicated fiber-optic bolometer system based on high-finesse FPIs. This multichannel fiber-optic bolometer system offers simple bolometer fabrication, good noise performance, lower cost per channel, and large dynamic range, which makes it attractive for plasma radiation measurement in magnetic-confinement fusion systems. Finally, we have investigated the utilization of the FOB with silicon pillar and gold disk on the heat sink both in air and vacuum. The response time reduction of the FOB using the silicon heat sink

along with the deconvolution method for signal processing proved very promising to be applied to the FOB system in fusion devices for radiation measurement.

#### **4.2. Future work**

In this dissertation, we have focused mainly on the development of the anemometer and bolometer based on the silicon Fabry-Perot interferometer. More research can be performed to finally implement the anemometer for turbulence measurement in a real scenario. More analysis on the resolution, measurement range etc. is needed for the constant temperature operation of the hot wire anemometer. Improving the time resolution will have some effect on the other parameters also for the constant temperature operation. Constant temperature operation, directivity reduction and temperature effect compensation were performed separately in the lab environment to demonstrate the idea. Implementation of all these findings together in the real turbulence measurement will be very promising.

There are several possible structures of the FOB to control the time constant and responsivity for the reconstruction of the plasma radiation profile from the fusion devices. FOBs with a metal ferrule, silicon heat sink with single and double trenches have been investigated. Overall, after designing the optimum multichannel bolometry system, a 2D array of this kind of multichannel bolometry system will be needed to get the plasma profile. So, future work will be the design and utilization of the FOB with proper heat sink and multiarray array design using the optimum structure for radiation measurement. Performance (NEPD, measurement range, cost) of the designed FOB should be further studied along with the other advantages such as immunity to electromagnetic interference, high temperature performance, electrical and optical multiplexing capabilities, large bandwidth, remote operation capability, resistance to harsh environment to make accurate comparisons to other available techniques. Long term drift compensation is also needed

to improve the FOB performance. Interrogation light power variation or radiation absorption in the gold disk absorber may cause the long-term drift. Intensive investigation is needed to get drift free measurement from the FOB.

## **BIBLIOGRAPHY**

## BIBLIOGRAPHY

- [1] E. Udd and W. B. Spillman Jr, *Fiber optic sensors: an introduction for engineers and scientists*. John Wiley & Sons, 2011.
- [2] B. Lee, "Review of the present status of optical fiber sensors," *Optical fiber technology*, vol. 9, no. 2, pp. 57-79, 2003.
- [3] G. Liu, M. Han, and W. Hou, "High-resolution and fast-response fiber-optic temperature sensor using silicon Fabry-Pérot cavity," *Opt Express*, vol. 23, no. 6, pp. 7237-7247, 2015.
- [4] Q. Shi, S. Sang, W. Zhang, P. Li, J. Hu, and G. Li, "Temperature sensor based on silicon microring," in *2013 13th IEEE International Conference on Nanotechnology (IEEE-NANO 2013)*, 2013: IEEE, pp. 1224-1227.
- [5] N. Y. Winnie, J. Michel, and L. C. Kimerling, "Athermal high-index-contrast waveguide design," *IEEE Photonics Technology Letters*, vol. 20, no. 11, pp. 885-887, 2008.
- [6] R. Slavík, J. Homola, J. Čtyroký, and E. Brynda, "Novel spectral fiber optic sensor based on surface plasmon resonance," *Sensors and Actuators B: Chemical*, vol. 74, no. 1-3, pp. 106-111, 2001.
- [7] Y. Liu et al., "An open-cavity fiber Fabry-Perot interferometer fabricated by femtosecond laser micromachining for refractive index sensing," in *Eleventh International Conference on Information Optics and Photonics (CIOP 2019)*, 2019, vol. 11209: International Society for Optics and Photonics, p. 1120902.
- [8] J. Botsis, L. Humbert, F. Colpo, and P. Giaccari, "Embedded fiber Bragg grating sensor for internal strain measurements in polymeric materials," *Optics and lasers in Engineering*, vol. 43, no. 3-5, pp. 491-510, 2005.
- [9] S. Mandal, V. Mishra, U. Tiwari, N. Hanumaiah, and R. G. Sarepaka, "Fiber Bragg grating sensor for temperature measurement in micro turning of optical surfaces with high surface integrity," *International journal of optomechatronics*, vol. 7, no. 4, pp. 244-252, 2013.
- [10] N. Uddin, G. Liu, Q. Sheng, and M. Han, "Constant temperature operation of fiber-optic hot-wire anemometers," *Optics letters*, vol. 44, no. 10, pp. 2578-2581, 2019.
- [11] Y. Zhang et al., "Fiber-optic anemometer based on single-walled carbon nanotube coated tilted fiber Bragg grating," *Optics express*, vol. 25, no. 20, pp. 24521-24530, 2017.
- [12] S. Gao, A. P. Zhang, H.-Y. Tam, L. Cho, and C. Lu, "All-optical fiber anemometer based on laser heated fiber Bragg gratings," *Optics express*, vol. 19, no. 11, pp. 10124-10130, 2011.

- [13] X. Wang, X. Dong, Y. Zhou, K. Ni, J. Cheng, and Z. Chen, "Hot-wire anemometer based on silver-coated fiber Bragg grating assisted by no-core fiber," *IEEE Photonics Technology Letters*, vol. 25, no. 24, pp. 2458-2461, 2013.
- [14] R. Chen, A. Yan, Q. Wang, and K. P. Chen, "Fiber-optic flow sensors for high-temperature environment operation up to 800 C," *Optics letters*, vol. 39, no. 13, pp. 3966-3969, 2014.
- [15] P. Caldas et al., "Fiber optic hot-wire flowmeter based on a metallic coated hybrid long period grating/fiber Bragg grating structure," *Applied optics*, vol. 50, no. 17, pp. 2738-2743, 2011.
- [16] H. Bruun, "Hot-wire anemometry-principles and signal analysis Oxford University Press," New York, NY, 1995.
- [17] G. Liu, W. Hou, W. Qiao, and M. Han, "Fast-response fiber-optic anemometer with temperature self-compensation," *Optics express*, vol. 23, no. 10, pp. 13562-13570, 2015.
- [18] G. Liu, Q. Sheng, D. Dam, J. Hua, W. Hou, and M. Han, "Self-gauged fiber-optic micro-heater with an operation temperature above 1000° C," *Optics letters*, vol. 42, no. 7, pp. 1412-1415, 2017.
- [19] M. A. Green and M. J. Keevers, "Optical properties of intrinsic silicon at 300 K," *Progress in Photovoltaics: Research and Applications*, vol. 3, no. 3, pp. 189-192, 1995.
- [20] P. Freymuth, "Frequency response and electronic testing for constant-temperature hot-wire anemometers," *Journal of Physics E: Scientific Instruments*, vol. 10, no. 7, p. 705, 1977.
- [21] N. Uddin, G. Liu, Q. Sheng, W. Hou, and M. Han, "Reduction of directivity of the fiber-optic water flow sensor based on laser-heated silicon Fabry-Perot cavity by using a spherical Tin shell," in *Fiber Optic Sensors and Applications XVI*, 2019, vol. 11000: International Society for Optics and Photonics, p. 110000P.
- [22] G. Wild and S. Hinckley, "Acousto-ultrasonic optical fiber sensors: Overview and state-of-the-art," *IEEE Sensors journal*, vol. 8, no. 7, pp. 1184-1193, 2008.
- [23] N. Takahashi, K. Tetsumura, K. Imamura, and S. Takahashi, "Fiber Bragg grating WDM underwater acoustic sensor with directivity," in *Fiber Optic and Laser Sensors and Applications; Including Distributed and Multiplexed Fiber Optic Sensors VII*, 1999, vol. 3541: International Society for Optics and Photonics, pp. 18-26.
- [24] J. C. Shipps and B. M. Abraham, "The use of vector sensors for underwater port and waterway security," in *ISA/IEEE Sensors for Industry Conference, 2004. Proceedings the*, 2004: IEEE, pp. 41-44.

- [25] A. Dagamseh, C. Bruinink, H. Droogendijk, R. J. Wiegerink, T. S. Lammerink, and G. J. Krijnen, "Engineering of biomimetic hair-flow sensor arrays dedicated to high-resolution flow field measurements," in *SENSORS, 2010 IEEE*, 2010: IEEE, pp. 2251-2254.
- [26] P. A. Fomitchov and S. Krishnaswamy, "Response of a fiber Bragg grating ultrasonic sensor," *Optical Engineering*, vol. 42, no. 4, pp. 956-963, 2003.
- [27] G. Liu, Q. Sheng, G. R. L. Piassetta, W. Hou, and M. Han, "A fiber-optic water flow sensor based on laser-heated silicon Fabry-Pérot cavity," in *Fiber Optic Sensors and Applications XIII, 2016*, vol. 9852: International Society for Optics and Photonics, p. 98521B.
- [28] W. Hou, M. Han, G. Liu, and Q. Sheng, "A high dynamic range in situ flow sensor," in *2018 OCEANS-MTS/IEEE Kobe Techno-Oceans (OTO)*, 2018: IEEE, pp. 1-5.
- [29] G. Liu, Q. Sheng, W. Hou, M. L. Reinke, and M. Han, "A Silicon-tipped Fiber-optic Sensing Platform with High Resolution and Fast Response," *Journal of visualized experiments: JoVE*, no. 143, 2019.
- [30] G. Liu, Q. Sheng, W. Hou, and M. Han, "Optical fiber vector flow sensor based on a silicon Fabry-Perot interferometer array," *Optics letters*, vol. 41, no. 20, pp. 4629-4632, 2016.
- [31] W. Hou, S. Woods, E. Jarosz, W. Goode, and A. Weidemann, "Optical turbulence on underwater image degradation in natural environments," *Applied optics*, vol. 51, no. 14, pp. 2678-2686, 2012.
- [32] Z. Liu, G. Liu, Q. Sheng, Z. Jing, M. Han, and W. Peng, "Fiber-Optic Current Sensor Based on Ohmic Heating of Tin Sphere With Embedded Silicon Fabry-Perot Interferometer," *Journal of Lightwave Technology*, vol. 37, no. 10, pp. 2165-2171, 2019.
- [33] G. Liu and M. Han, "Fiber-optic gas pressure sensing with a laser-heated silicon-based Fabry-Perot interferometer," *Optics letters*, vol. 40, no. 11, pp. 2461-2464, 2015.
- [34] S. Sanitjai and R. J. Goldstein, "Forced convection heat transfer from a circular cylinder in crossflow to air and liquids," *International journal of heat and mass transfer*, vol. 47, no. 22, pp. 4795-4805, 2004.
- [35] S. Churchill and M. Bernstein, "A correlating equation for forced convection from gases and liquids to a circular cylinder in crossflow," 1977.
- [36] C. Sak, R. Liu, D.-K. Ting, and G. Rankin, "The role of turbulence length scale and turbulence intensity on forced convection from a heated horizontal circular cylinder," *Experimental thermal and fluid science*, vol. 31, no. 4, pp. 279-289, 2007.
- [37] B. O. Kvamme, J. Peechanatt, O. T. Gudmestad, K. E. Solberg, and Y. A. Amith, "Heat Loss of Insulated Pipes in Cross-Flow Winds," *Journal of Offshore Mechanics and Arctic Engineering*, vol. 141, no. 2, 2019.

- [38] S. S. Pitla, E. A. Groll, and S. Ramadhyani, "New correlation to predict the heat transfer coefficient during in-tube cooling of turbulent supercritical CO<sub>2</sub>," *International journal of refrigeration*, vol. 25, no. 7, pp. 887-895, 2002.
- [39] M. H. Esfe and S. Saedodin, "Turbulent forced convection heat transfer and thermophysical properties of Mgo–water nanofluid with consideration of different nanoparticles diameter, an empirical study," *Journal of thermal analysis and calorimetry*, vol. 119, no. 2, pp. 1205-1213, 2015.
- [40] S. Whitaker, "Forced convection heat transfer correlations for flow in pipes, past flat plates, single cylinders, single spheres, and for flow in packed beds and tube bundles," *AIChE Journal*, vol. 18, no. 2, pp. 361-371, 1972.
- [41] N. Uddin, G. Liu, Q. Sheng, W. Hou, and M. Han, "Temperature compensation of fiber-optic water flow sensor based on laser-heated silicon Fabry-Perot cavity," in *Optical Fiber Sensors, 2020: Optical Society of America*, p. W3. 3.
- [42] W. Hou and S. o. P.-o. I. Engineers, *Ocean sensing and monitoring: optics and other methods*. SPIE Press, 2013.
- [43] M. Reinke et al., "Development of plasma bolometers using fiber-optic temperature sensors," *Review of Scientific Instruments*, vol. 87, no. 11, p. 11E708, 2016.
- [44] Q. Sheng, G. Liu, M. L. Reinke, and M. Han, "A fiber-optic bolometer based on a high-finesse silicon Fabry-Pérot interferometer," *Review of Scientific Instruments*, vol. 89, no. 6, p. 065002, 2018.
- [45] N. Uddin et al., "Fiber-optic silicon Fabry-Perot interferometric bolometer with improved detection limit for magnetic confinement fusion," *Review of Scientific Instruments*, vol. 92, no. 2, p. 023515, 2021.
- [46] H. Meister et al., "Bolometer developments in diagnostics for magnetic confinement fusion," *Journal of Instrumentation*, vol. 14, no. 10, pp. C10004-C10004, 2019/10/02 2019, doi: 10.1088/1748-0221/14/10/c10004.
- [47] C. Côté and A. DeSilva, "Fast pyroelectric detector for broadband radiated power measurements," *Review of scientific instruments*, vol. 67, no. 12, pp. 4146-4149, 1996.
- [48] E. Müller and F. Mast, "A new metal resistor bolometer for measuring vacuum ultraviolet and soft x radiation," *J Appl Phys*, vol. 55, no. 7, pp. 2635-2641, 1984.
- [49] K. F. Mast, J. Vallet, C. Andelfinger, P. Betzler, H. Kraus, and G. Schramm, "A low noise highly integrated bolometer array for absolute measurement of VUV and soft x radiation," *Review of scientific instruments*, vol. 62, no. 3, pp. 744-750, 1991.

- [50] H. Hsuan, K. Bol, and R. Ellis, "Measurement of the energy balance in ATC tokamak," *Nuclear Fusion*, vol. 15, no. 4, p. 657, 1975.
- [51] M. di Maio, *Design of a Ferroelectric Bolometer*. Shaker, 2000.
- [52] B. Peterson, "Infrared imaging video bolometer," *Review of Scientific Instruments*, vol. 71, no. 10, pp. 3696-3701, 2000.
- [53] J. Schivell, G. Renda, J. Lowrance, and H. Hsuan, "Bolometer for measurements on high-temperature plasmas," *Review of Scientific Instruments*, vol. 53, no. 10, pp. 1527-1534, 1982.
- [54] S. Paul, R. Fonck, and G. Schmidt, "Operation of a multichannel tangential bolometer on PBX," *American Institute of Physics*, 1986.
- [55] B. L. Henke, E. M. Gullikson, and J. C. Davis, "X-ray interactions: photoabsorption, scattering, transmission and reflection  $E= 50\text{-}30,000$  eV,  $Z= 1\text{-}92$ ," *Atomic data and nuclear data tables*, vol. 54, no. 2, 1993.
- [56] M. D. Kriese, N. R. Moody, and W. W. Gerberich, "Effects of annealing and interlayers on the adhesion energy of copper thin films to SiO<sub>2</sub>/Si substrates," *Acta Materialia*, vol. 46, no. 18, pp. 6623-6630, 1998/11/01/ 1998, doi: [https://doi.org/10.1016/S1359-6454\(98\)00277-8](https://doi.org/10.1016/S1359-6454(98)00277-8).
- [57] H. Nagata, T. Shinriki, K. Shima, M. Tamai, and E. Min Haga, "Improvement of bonding strength between Au/Ti and SiO<sub>2</sub> films by Si layer insertion," *Journal of Vacuum Science & Technology A: Vacuum, Surfaces, and Films*, vol. 17, no. 3, pp. 1018-1023, 1999.
- [58] N. Uddin et al., "Multichannel Fiber-Optic Silicon Fabry–Pérot Interferometric Bolometer System for Plasma Radiation Measurements," in *Photonics*, 2021, vol. 8, no. 9: Multidisciplinary Digital Publishing Institute, p. 344.
- [59] H. Meister et al., "The ITER bolometer diagnostic: Status and plans," *Review of Scientific Instruments*, vol. 79, no. 10, p. 10F511, 2008.
- [60] Y. Duan, L. Hu, S. Mao, K. Chen, S. Lin, and E. D. Team, "The resistive bolometer for radiated power measurement on EAST," *Review of Scientific Instruments*, vol. 83, no. 9, p. 093501, 2012.
- [61] D. R. Ferreira, P. J. Carvalho, I. S. Carvalho, C. Stuart, P. J. Lomas, and J. Contributors, "Monitoring the plasma radiation profile with real-time bolometer tomography at JET," *Fusion Engineering and Design*, vol. 164, p. 112179, 2021.
- [62] M. U. Lee et al., "Radiation measurement in plasma disruption by thin-foil infrared bolometer," *Review of Scientific Instruments*, vol. 92, no. 5, p. 053536, 2021.

- [63] H. Meister et al., "Bolometer developments in diagnostics for magnetic confinement fusion," *Journal of Instrumentation*, vol. 14, no. 10, p. C10004, 2019.
- [64] Y. Zhang et al., "Fringe visibility enhanced extrinsic Fabry–Perot interferometer using a graded index fiber collimator," *IEEE Photonics Journal*, vol. 2, no. 3, pp. 469-481, 2010.
- [65] W. Emkey and C. Jack, "Analysis and evaluation of graded-index fiber lenses," *Journal of Lightwave Technology*, vol. 5, no. 9, pp. 1156-1164, 1987.
- [66] T. Carlstrom, D. Ahlgren, and J. Crosbie, "Real-time, vibration-compensated CO<sub>2</sub> interferometer operation on the DIII-D tokamak," *Review of scientific instruments*, vol. 59, no. 7, pp. 1063-1066, 1988.
- [67] W. Bergerson, P. Xu, J. Irby, D. Brower, W. Ding, and E. Marmor, "Far-infrared polarimetry diagnostic for measurement of internal magnetic field dynamics and fluctuations in the C-MOD Tokamak," *Review of Scientific Instruments*, vol. 83, no. 10, p. 10E316, 2012.
- [68] S. Lederhandler, "Infrared studies of birefringence in silicon," *Journal of applied physics*, vol. 30, no. 11, pp. 1631-1638, 1959.
- [69] Q. Sheng, G. Liu, N. Uddin, M. L. Reinke, and M. Han, "Fiber-Optic Silicon Fabry-Perot Interferometric Bolometer: The Influence of Mechanical Vibration and Magnetic Field," *Journal of Lightwave Technology*, vol. 38, no. 8, pp. 2547-2554, 2020.